

Polarized Neutron studies  
of Spin Dynamics  
of Functional Materials

**Giovanni Battista Pasquino**

ROYAL HOLLOWAY COLLEGE  
UNIVERSITY OF LONDON

A DISSERTATION SUBMITTED TO THE UNIVERSITY OF LONDON  
FOR THE DEGREE OF DOCTOR OF PHILOSOPHY

September 2014



## Declaration of authorship

I, Giovanni Pasquino hereby declare that this thesis and the work presented in it is entirely my own. Where I have consulted the work of others, this is always clearly stated.

Signed: \_\_\_\_\_

Date: \_\_\_\_\_

## Abstract

Three technologically important materials were studied using polarised neutron techniques. The first, INVAR, is widely used in devices that exploit its low thermal expansion. The second, sodium-cobaltate is an example of a new class of correlated thermoelectric materials. The third, manganese vanadate has potential for devices that exploit the couple between its spin and orbital degrees of freedom.

Spin dynamics in INVAR have been studied using the quasi-elastic neutron spin echo technique. Spin dynamics with a characteristic time scale of nanoseconds has been found. Additional muon spin relaxation investigations have confirmed this result and, in addition, revealed the presence of second time scale in the range 0.1 microseconds. The origin of the nanosecond scale may be associated with individual spin excitations, while the slower scale may be associated with the dynamics of magnetic in-homogeneities, in agreement with previous polarised neutron results in the literature. This second component of spin dynamics may be important in understanding the INVAR effect.

The spin-wave dispersion of sodium cobaltate was measured by inelastic neutron scattering using XYZ polarization analysis in order to separate the magnetic signal from the structural scattering. Excellent agreement with the low energy excitations was obtained with calculations using the McPhase program for this itinerant system. In particular, it was possible to explain the energy gap via the anisotropy of the exchange coupling.

McPhase calculations were performed for manganese vanadate, and it was possible to understand the magnetic excitations observed previously from this system. We obtained a new magnetic structure that differs from the existing literature. The calculated magnetic excitations from this ground state are in good agreement with the experimental data. We are able to rule out the previously published model, and our exchange constants are consistent theoretical predictions on the basis of the proposed orbital ordering.

# Contents

|          |   |           |
|----------|---|-----------|
| <b>1</b> | <b>Introduction</b>   | <b>13</b> |
| <b>2</b> | <b>Experimental Techniques</b>  | <b>16</b> |
| 2.1      | Neutron scattering theory . . . . .                                     | 16        |
| 2.1.1    | Coherent and Incoherent nuclear scattering . . . . .                    | 17        |
| 2.1.2    | Magnetic scattering . . . . .   | 18        |
| 2.1.3    | Polarized neutron techniques . . . . .                                  | 19        |
| 2.1.4    | The XYZ-technique . . . . .   | 22        |
| 2.1.5    | Spin-echo . . . . .   | 26        |
| 2.1.6    | Neutron instruments . . . . .   | 32        |
| 2.2      | Muon Spin Relaxation Technique $\mu$ SR . . . . .                       | 34        |
| 2.2.1    | The Muon Spin Relaxation function . . . . .                             | 37        |
| 2.2.2    | Muons Instruments . . . . .   | 40        |
| <b>3</b> | <b>The McPhase Software</b>   | <b>45</b> |
| 3.1      | Introduction . . . . .  | 45        |
| 3.2      | The Solion and Iclion modules . . . . .                                 | 47        |
| 3.2.1    | The module Solion (weak crystal field) . . . . .                        | 48        |
| 3.2.2    | The module iclion (intermediate and strong crystal field) . . . . .     | 51        |
| 3.3      | The core module mcphas (Magnetic Phase Diagram calculations) . . . . .  | 54        |
| 3.3.1    | The Mean-Field Monte Carlo algorithm . . . . .                          | 55        |
| 3.4      | The module mcdisp (calculation of the spin waves dispersions) . . . . . | 58        |

|          |   |            |
|----------|---|------------|
| 3.4.1    | The calculation of the spin wave dispersions . . . . .  | 59         |
| <b>4</b> | <b>Spin Fluctuations in INVAR <math>\text{Fe}_{65}</math></b>   | <b>68</b>  |
| 4.1      | Introduction to the INVAR effect . . . . .  | 68         |
| 4.2      | Experimental Procedure . . . . .  | 77         |
| 4.3      | Results and Discussions . . . . .   | 78         |
| <b>5</b> | <b>Spin-waves in <math>\text{Na}_x\text{CoO}_2</math></b>   | <b>93</b>  |
| 5.1      | Introduction to $\text{Na}_x\text{CoO}_2$ . . . . .   | 93         |
| 5.2      | McPhase Calculation on $\text{Na}_x\text{CoO}_2$ . . . . .  | 104        |
| 5.3      | Results and Discussion . . . . .  | 109        |
| 5.3.1    | Tri-vacancy Phase check . . . . .   | 110        |
| 5.3.2    | Presentation of the Inelastic Data . . . . .  | 111        |
| 5.3.3    | Spin-wave dispersions . . . . .   | 120        |
| <b>6</b> | <b>Spin-waves in <math>\text{MnV}_2\text{O}_4</math></b>  | <b>132</b> |
| 6.1      | 5.1 Introduction to $\text{MnV}_2\text{O}_4$ . . . . .  | 132        |
| 6.2      | Calculation of the $\text{MnV}_2\text{O}_4$ ground state magnetic structure<br>with McPhase . . . . . | 138        |
| 6.3      | Spin-Wave Dispersion and Comparison with the IN20 data . . .  | 146        |
| <b>7</b> | <b>Conclusions and Future Outlook</b>   | <b>157</b> |
| <b>A</b> | <b>McPhase Input Files</b>  | <b>159</b> |

# List of Figures

|     |  |    |
|-----|--|----|
| 2.1 | Experimental setup for unidirectional polarization analysis. . . .   | 21 |
| 2.2 | The geometry of an xyz-polarization analysis experiment. . . . .   | 25 |
| 2.3 | The basic scheme of a NSE spectrometer (top) Spin echo signal<br>(bottom). . . . .   | 27 |
| 2.4 | The scheme of the Ferromagnetic Neutron Spin Echo experi-<br>mental settings. . . . .  | 31 |
| 2.5 | Scheme of the IN20 triple axis spectrometer of I.L.L. . . . .  | 33 |
| 2.6 | The scheme of the IN11 spin echo spectrometer . . . . .  | 34 |
| 2.7 | The experimental arrangement for a muon spin relaxation ex-<br>periment. . . . .   | 35 |
| 2.8 | The HiFi muon spectrometer. . . . .  | 41 |
| 2.9 | The EMU muon spectrometer. . . . .   | 41 |
| 3.1 | Scheme of the McPhase program packages with modules and<br>relative tasks. . . . .   | 46 |
| 3.2 | The iterative mean field procedure scheme . . . . .  | 57 |
| 3.3 | Scheme of the DMD algorithm . . . . .  | 66 |
| 4.1 | Temperature dependence of the magnetizations of the non-INVAr<br>alloy $\text{Fe}_{50}\text{Ni}_{50}$ and the INVAr alloys $\text{Fe}_{65}\text{Ni}_{35}$ and $\text{Fe}_3\text{Pt}$ . . . . | 71 |
| 4.2 | The average spin-flip cross-sections are plotted in absolute units<br>for three data sets: filled circles at 1.4 T, 300 K; open circles at<br>2 T, 300 K; triangles at 2 T, 4.2 K. . . . .   | 72 |

|     |  |     |
|-----|--|-----|
| 4.3 | The angular dependence of the non-spin-flip (NSF) (a) and the spin-flip (SF) scattering (b), (c) and (d) for $\text{Fe}_{1-x}\text{Ni}_x$ alloys. . . . .  | 74  |
| 4.4 | Linear thermal expansion coefficient of fcc ferromagnets calculated by Liot et al. in the DLM approach. Vertical arrows indicate Curie temperatures. . . . .   | 76  |
| 4.5 | FNSE measurements performed on the INVAR sample. . . . .   | 79  |
| 4.6 | Zero field muon relaxation spectra taken at different temperatures. . . . .  | 80  |
| 4.7 | Zero field muon relaxation rate components obtained from the sum of two exponential functions. . . . .   | 83  |
| 4.8 | Zero field initial asymmetries corresponding to the fast component (red circles) and the slow component (yellow circles). . . . .  | 84  |
| 4.9 | Muon depolarization rates under an applied longitudinal field of 0.5 T (blue circles), 1 T (yellow circles) and 2 T (red circles). . . . .   | 85  |
| 5.1 | a) Crystal structure of $\text{Na}_x\text{CoO}_2$ : $\text{CoO}_2$ layer with intercalated Na. b) The hexagonal lattice of Co in the ab plane. c) The phase diagram of $\text{Na}_x\text{CoO}_2$ . . . . .     | 95  |
| 5.2 | a) The two interpenetrating hexagonal lattices of intercalation sites $2b$ and $2d$ of the space group: $\text{P6}_3/\text{mmc}$ occupied by the sodium ions and denoted by Na1 and Na2, respectively. . . . . | 96  |
| 5.3 | a) Spin flip (SF) intensity at $\mathbf{Q}=(1,0,1)$ and $(1,0,0)$ , as a function of temperature (the lines are guides for the eye). . . . .   | 98  |
| 5.4 | Spin wave dispersion along $(h,h,0)$ and $(0,0,l)$ for $x=0.82$ (red) [17] and $x=0.75$ (blue). The solid lines are obtained by fitting the data using the Hamiltonians described in the text. . . . .         | 98  |
| 5.5 | (a)-(j) Energy scans at $\mathbf{Q}=(0,0,1)$ at temperatures between 1.5 K and 24.4 K. . . . .   | 101 |
| 5.6 | Magnon dispersion parallel to $(0,0,1)$ centred at $(0,0,x)=(0,0,3)$ measured at IN20. . . . .   | 102 |



|      |  |     |
|------|--|-----|
| 5.7  | The $\text{CoO}_6$ octahedra of $\text{Na}_x\text{CoO}_2$ . They are elongated along their (0,0,1) direction and trigonally distorted. . . . .   | 106 |
| 5.8  | The $1/13^{\text{th}}$ tri-vacancy phase structure observed by M. Pandiyan.  | 110 |
| 5.9  | Absence of the reflection peaks at (0.667,0.333,0), (0.2,0.2,0) and (0.4,0.4,0). The sample is not in the square phase. . . . .  | 112 |
| 5.10 | Absence of the reflection peak at (0.6,0.4,0). The sample is not in the stripe phase. . . . .  | 113 |
| 5.11 | Intense peak observed in both the <b>h</b> and <b>k</b> directions around (1.077,0.692,0) .A double peak is present at (1.077,0.692,0.25). The sample is in the $1/13^{\text{th}}$ single phase. . . . . | 114 |
| 5.12 | a) Q scan at fixed energy $E=5$ meV along the direction (h,h,3).<br>b) The signal obtained by the linear combination shown in the picture and relative multiple Gaussian fit. . . . .                    | 115 |
| 5.13 | a) Q scan at fixed energy $E=7.5$ meV along the direction (h,h,3).<br>b) The signal obtained by the linear combination shown in the picture and relative multiple Gaussian fit. . . . .                  | 116 |
| 5.14 | a) Q scan at fixed energy $E=4$ meV along the direction (0,0,1).<br>b) Multiple Gaussian fit of the $\text{SF}_x$ component. . . . .   | 117 |
| 5.15 | a) Q scan at fixed energy $E=5$ meV along the direction (0,0,1).<br>b) Multiple Gaussian fit of the $\text{SF}_x$ component. . . . .   | 118 |
| 5.16 | Energy scan at fixed Q (0.5,0.5,3). Only the $\text{SF}_x$ is shown. Maybe there is a very low intensity peak placed around $\sim 31$ meV . . . . .  | 120 |
| 5.17 | a) Energy scan at (0,0,2.5) b) The xyz-polarization analysis result in well resolved peak in zero background easily fitted by a Gaussian function. . . . .   | 121 |
| 5.18 | a) Energy scan at zone centre (0,0,3). b) an additional peak is necessary to have a good fit. . . . .  | 122 |

|      |  |     |
|------|--|-----|
| 5.19 | Calculated dispersion along the direction (0,0,1) (green line) and relative inelastic data (red squares). . . . .  | 124 |
| 5.20 | Calculated dispersion along the direction (h,h,3) (red line) and relative inelastic data (green squares). . . . .  | 125 |
| 5.21 | The theoretical model of Johannes et al. . . . .   | 126 |
| 5.22 | Comparison between the dispersion calculated with different values of the inter-plane neighbours paremeters, $J_c$ and $J'_c$ . . . .  | 128 |
| 6.1  | Orbital order of vanadium ions below the structural phase transition. A view down the [001 . . . . .   | 134 |
| 6.2  | Three-dimensional electron density plot showing the orbital ordering proposed by Sarkar et al. . . . .   | 135 |
| 6.3  | Temperature dependence of x-ray diffraction of the $MnV_2O_4$ single crystal . . . . .   | 136 |
| 6.4  | (a) Projection of the V tetrahedron in the ab plane. (b), (c) Graphical representation of the low-temperature non-collinear ferrimagnetic structure of the $MnV_2O_4$ . (d) Projection of the magnetic structure on the basal plane. . . . . | 137 |
| 6.5  | Plumier magnetic structure. . . . .  | 137 |
| 6.6  | The $VO_6$ octahedra. They are trigonally distorted and compressed along the c direction at base temperaure. . . . .   | 139 |
| 6.7  | The four subsystems given by the vanadium ion and one of the four oxygen surrounding configurations. Chains of V1-V3 along $\vec{a}$ and V2-V4 along $\vec{b}$ . . . . .   | 141 |
| 6.8  | The ground state magnetic structure of $MnO_2V_4$ . V1, V3 ions in black and V2, V4 ions in cyan; Mn ions in red. . . . .  | 145 |
| 6.9  | Spin-wave dispersions measured by A. Magee along the cubic direction $(2+h,h,0)_c$ (top) which correspond to the tetragonal direction $(h,1,0)_t$ (bottom). . . . .  | 149 |

|      |  |     |
|------|--|-----|
| 6.10 | Spin wave dispersion calculated along the tetragonal direction $(2,k,0)_t$ (bottom) in comparison with that measured along the equivalent cubic direction $(h+2,h-2,0)_c$ (top). . . . . | 150 |
| 6.11 | Spin-wave dispersion calculated along the tetragonal directions $(h,2-h,0)_t$ (bottom) and measured along the equivalent cubic direction $(2,k,0)_c$ (top). . . . .                      | 151 |
| 6.12 | Spin wave dispersion measured along the the cubic direction $(h,0,0)_c$ (top) and calculated along the equivalent tetragonal direction $(h,h,0)_t$ (bottom). . . . .                     | 152 |
| 6.13 | Chung et al. spin wave dispersion along the cubic direction $(2,0,l)_c$ . They measured the spin wave dispersion with a multi domain sample with unpolarized neutrons. . . . .           | 153 |
| 6.14 | Spin-wave dispersion along the tetragonal off-symmetry measured by A. Magee along the cubic direction $(2.5+h/4,h,0)_c$ (top) . . . . .  | 154 |
| A.1  | An example of Input file for the program <b>ic1ion</b> of the package McPhase. . . . .   | 161 |
| A.2  | An example of Input file for the core module <b>mcphas</b> of the package McPhase. . . . .   | 162 |
| A.3  | Input file for the module <b>mcdisp</b> of the package McPhase. This file contains the list of scattering vectors for which magnetic excitation energies are calculated. . . . .         | 163 |
| A.4  | Input file containing the mean field at ion sites calulated with the program <b>mcphas</b> for a given Temperature, T, and external magnetic field, H. . . . .                           | 164 |

# List of Tables

|     |   |     |
|-----|---|-----|
| 5.1 | Atomic parameters of $\text{Na}_{0.77}\text{CoO}_2$ . Space group: $P6_3/mmc$ .<br>a=2.84126(6) Å, c=10.8144(3) Å. . . . .  | 95  |
| 5.2 | Values of the coupling constants (see 5.3 b)) obtained in different work. $\text{Na}_{0.82}\text{CoO}_2$ from Bayrakci et al. and $\text{Na}_{0.75}\text{CoO}_2$ of Helme et al. . . . .  | 100 |
| 5.3 | Crystal field parameters in Llm Wybourne notation calculated in point-charge approximation. . . . .   | 107 |
| 5.4 | Fit results after the XYZ-polarization analysis of the fixed energy Q scans. . . . .  | 119 |
| 5.5 | The intra-plane exchange constant , $J_{ab}$ , and the $J^{xx,yy}$ components of the inter-plane nearest and next neighbours exchange constants, $J_c$ and $J'_c$ , obtained by fitting the dispersion along the direction (h,h,3). . . . . | 127 |
| 6.1 | Atomic parameters of $\text{MnV}_2\text{O}_4$ at 2 K [ $I4_1/a$ , a = 6.0250(8) Å, c = 8.5142(8) Å . . . . .  | 140 |
| 6.2 | Point-charge calculated crystal field parameters in Blm Stevens notation. . . . .   | 143 |
| 6.3 | Exchange coupling constants. . . . .  | 148 |

# Chapter 1

## Introduction

This thesis focuses on the study of the spin dynamics of *functional* materials. The consequences of the magnetic excitations on physical properties are varied, and the materials have several practical applications.

$\text{Fe}_{65}\text{Ni}_{35}$  is a compound which exhibits zero thermal expansion over a wide range of temperature and this behaviour is known as the INVAR effect. This property is exploited in many technological applications in particular it is used in instrumentation, for example as a hair spring in mechanical watches and more recently in the shadow masks in colour televisions and computer screens. This behaviour is clearly related to the magnetism of this compound, the conventional thermal expansion is compensated by large magnetovolume effects which are related to the spin dynamics in this system. Therefore the characterization of these spin dynamics may provide useful information in order to understand the origins of this zero thermal expansion behaviour.

Sodium cobaltate  $\text{Na}_x\text{CoO}_2$  shows high thermopower coupled with low resistivity over a wide range of doping  $x$ . This makes it a promising candidate

for technological applications such as thermoelectric cooling. More recently it has been observed that it becomes a superconductor if hydrated. The spin degrees of freedom have important implications in superconductivity, and recent studies have shown that the application of a magnetic field strongly influences the thermopower effects in this compound. Therefore, the study of the magnetic excitations in sodium cobaltate may provide important information to understand the mechanisms related to its thermoelectric power and superconductivity.

$\text{MnV}_2\text{O}_4$  exhibits interesting orbital ordering when a magnetic field is applied and may be used for the realization of magnetic sensors and magnetic memories. Furthermore,  $\text{MnV}_2\text{O}_4$  is particularly interesting because of its complex magnetic behaviour associated with structural transitions. A clear understanding of the relationship between magnetism and orbital ordering is still lacking and the study of the magnetic excitations in this compound may provide valuable information.

In each case polarized neutrons are used as the primary experimental probe. For INVAR  $\text{Fe}_{65}\text{Ni}_{35}$ , muon spin relaxation is also exploited, and for  $\text{Na}_x\text{CoO}_2$  and  $\text{MnV}_2\text{O}_4$  the experiments are complemented by Monte Carlo calculations using the software McPhase.

In chapter 2, we describe the experimental techniques used to investigate the magnetic excitations in these three different materials.

In chapter 3, we describe in detail the software McPhase used to calculate the magnetic structure and magnetic excitations. In chapter 4 we present the results of neutron spin echo and muon spin relaxation measurements performed

on INVAR  $\text{Fe}_{65}\text{Ni}_{35}$ . In chapters 5 and 6 we present the results of spin-wave dispersion measurement performed on  $\text{Na}_x\text{CoO}_2$  and  $\text{MnV}_2\text{O}_4$  with polarized neutron scattering techniques. These results are compared with the spin-wave calculations obtained with the software McPhase.

# Chapter 2

## Experimental Techniques

### 2.1 Neutron scattering technique

Neutrons are important probes for the investigation of many important properties of condensed matter such as nuclear and magnetic structure of chemical compounds and related excitations. They interact with matter in two different ways, either through short range strong nuclear forces or via long range magnetic interactions. Neutrons are uncharged, therefore they can penetrate deep into the matter and come close to the nuclei before being scattered by the nuclear forces. Furthermore neutrons have spin  $1/2$ , so they are sensitive to the magnetic field of the unpaired electrons in the materials.

Neutrons are created in large quantities by spallation or nuclear fission and the energy spectrum of the produced beam, is determined by the moderator. In particular, thermal neutrons result in a de Broglie wavelength of the order of the inter-atomic distances in solids. Thus they are optimal probes to determine the structure of materials through diffraction experiments [1]. Fur-



thermore the energy of thermal neutrons is comparable with that of many excitations in condensed matter. This property may be exploited to study both the nuclear vibrations in a solid or magnetic excitations in a magnetic system.

In this work we performed inelastic neutron scattering measurements to investigate magnetic excitations in three different magnetically ordered materials. In particular, we used the polarized neutron technique to separate the nuclear contribution to the neutron scattering from the magnetic one.

### 2.1.1 Coherent and Incoherent nuclear scattering

The fundamental quantity determined in a nuclear scattering experiment is the double differential cross-section given by:

$$\frac{\partial^2 \sigma}{\partial \Omega \partial E} = \frac{1}{2\pi \hbar} \frac{k_f}{k_i} \sum_{j,j'} b_j b_{j'} \int_{-\infty}^{\infty} \langle \exp\{-iq \cdot R_{j'}(0)\} \exp\{-iq \cdot R_j(t)\} \rangle e^{-i\omega t} dt \quad (2.1)$$

where  $k_i$  and  $k_f$  are the incident and scattered neutron wavevectors, respectively.  $\langle \rangle$  denotes the thermal average and the sum is on all pairs of nuclei.  $b_j$  is the scattering length of the nucleus at the site  $R_j$ . This quantity varies from one nucleus to one another owing to nuclear spin or the presence of isotopes or both. Assuming that there is no correlation between the values of  $b$  for any two nuclei and the system contains a large number of nuclei, the cross section may be written as

$$\frac{\partial^2 \sigma}{\partial \Omega \partial E} = \frac{1}{2\pi \hbar} \frac{k_f}{k_i} \sum_{j,j'} \overline{b_j b_{j'}} \int \langle j', j \rangle e^{-i\omega t} dt \quad (2.2)$$

where the bar on the product  $\overline{b_j b_{j'}}$  indicates the average over the entire system.

The term in the integral of equation 2.1 has been written in a more compact form. Under the assumption of no correlation we have

$$\begin{aligned}\overline{b_j b_{j'}} &= (\bar{b})^2 & j' \neq j \\ \overline{b_j b_{j'}} &= \bar{b}^2 & j' = j\end{aligned}$$

then equation 2.2 assumes the following expression

$$\frac{\partial^2 \sigma}{\partial \Omega \partial E} = \frac{1}{8\pi^2 \hbar} \frac{k_f}{k_i} \left[ \sigma_{coh} \sum_{j,j'} \int \langle j', j \rangle e^{-i\omega t} dt + \sigma_{inc} \sum_j \int \langle j, j \rangle e^{-i\omega t} dt \right] \quad (2.3)$$

The first term in equation 2.3 represents the coherent scattering cross section  $\sigma_{coh} = 4\pi(\bar{b})^2$  while the second term the incoherent one  $\sigma_{inc} = 4\pi[(\bar{b}^2 - \bar{b})^2]$ .

The coherent scattering gives the intensity which would be produced if all scattering lengths were equal to  $\bar{b}$ . The incoherent scattering arises from the random distribution of the deviations of the scattering lengths from their mean value. This term must be added to obtain the observed total cross section.

### 2.1.2 Magnetic scattering

The neutron is an optimal probe to investigate the magnetic properties of condensed matter. Having non-zero magnetic moment  $\mu_N$  the neutron interacts with any unpaired electrons in a magnetic atom. Elastic scattering of this kind allows us to deduce the magnetic structure of the system, while inelastic

scattering provides information on the magnetic excitations. Unlike the case of X-rays, neutrons have equal sensitivity to nuclear and magnetic structure, in fact the cross sections of these two processes are roughly the same. The magnetic neutron cross section for a spin lattice is given by:

$$\frac{\partial^2 \sigma}{\partial \Omega \partial E} = \frac{(\gamma r_0)^2 k_f}{2\pi \hbar k_i} N [\frac{1}{2} g F(q)]^2 e^{-2W} \sum_{\alpha\beta} (\delta_{\alpha\beta} - \hat{k}_\alpha \hat{k}_\beta) \sum_l \exp(iq \cdot l) \\ \times \int_{-\infty}^{\infty} \langle S_0^\alpha(0) S_l^\beta(t) \rangle e^{-i\omega t} dt$$

where  $\gamma$  is the gyromagnetic factor of the neutron and  $r_0$  is the electron classical radius.  $F(q)$  is known as the magnetic form factor. The factor  $\sum_{\alpha\beta} (\delta_{\alpha\beta} - \hat{k}_\alpha \hat{k}_\beta)$  indicates that the cross section is non-zero only when the scattering wavevector  $\mathbf{q}$  is perpendicular to the spin direction. This means that neutrons are sensitive not only to the spatial distribution of spins but also to their directions [1].

### 2.1.3 Polarized neutron techniques

In order to achieve separation of magnetic scattering cross section from the total cross section in a neutron scattering experiment, analysis of the spin of the scattered neutron is required. To do that, it is necessary to produce a polarized neutron beam in a definite spin state  $|S\rangle$  and analyse the spin-state distribution of the neutrons after scattering. The polarization of a neutron beam is defined as the expectation value of the neutron spin normalized by its modulus. Hence we have:

$$\mathbf{P} = 2 \langle \mathbf{S} \rangle / \langle \sigma \rangle \quad (2.4)$$

where  $\sigma$  is the Pauli operator. If during our scattering experiment a magnetic field is applied along a certain direction, the neutron can be considered as being spin up  $|\uparrow\rangle$  or spin down  $|\downarrow\rangle$  relative to the magnetic field direction. Therefore, the polarization can then be expressed as a scalar as :

$$P = \frac{N_{\uparrow} - N_{\downarrow}}{N_{\uparrow} + N_{\downarrow}} = \frac{F - 1}{F + 1} \quad (2.5)$$

where  $N_{\uparrow}$  and  $N_{\downarrow}$  are the numbers of neutrons with spin up and spin down, respectively.  $F = \frac{N_{\uparrow}}{N_{\downarrow}}$  is called flipping ratio. A completely polarized beam has  $P=1$  (all  $\uparrow$ ) or  $P=-1$  (all  $\downarrow$ ) and an unpolarized beam has  $P=0$ . For  $0 < |P| < 1$  the beam is partially polarized. All polarization analysis experiments performed under these conditions are termed longitudinal polarization analysis (LPA) experiments. Only the scalar component of the polarization along the field direction is measurable. All transverse polarization components will rapidly precess around the field direction and will be not measured in the experiment.

In order to obtain a spin-polarised incident neutron beam, filters, mirrors and supermirrors or magnetic crystals can be used. They polarize the incident neutron beam via preferential absorption, reflection and Bragg reflection, respectively [1, 2]. A similar crystal is used to determine the energy and spin state of the scattered neutron (Analyser). A guide magnetic field of a few millitesla is applied along the neutron path to preserve the polarization throughout the instrument. Spin-flipper devices, which may be 'On or 'Off', are used to change the spin state from  $\uparrow$  to  $\downarrow$  or vice versa. Here,  $\uparrow$  and  $\downarrow$  refer to the neutron

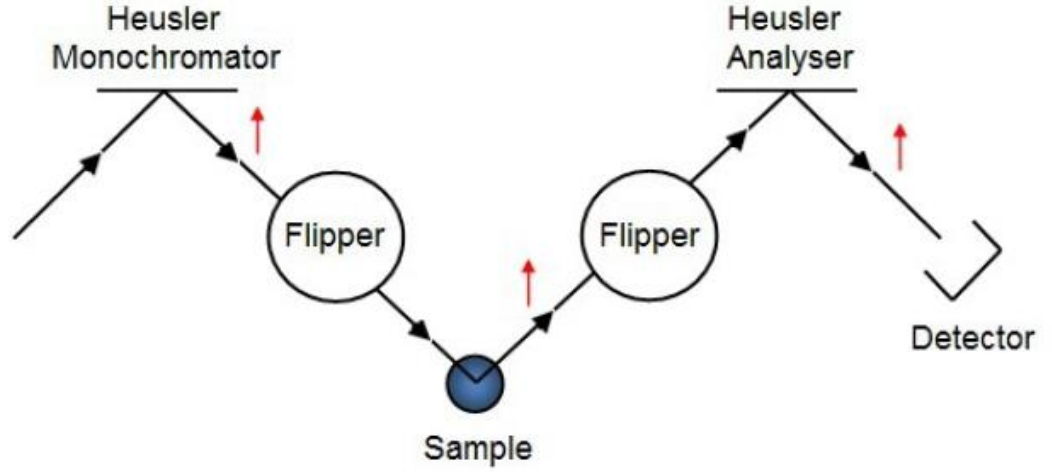


Figure 2.1: *Experimental setup for unidirectional polarization analysis.* [15]

moment parallel or antiparallel, respectively to the guide field. To do that they produce a radio-frequency field perpendicular to the guide field. Changing the magnetic guide field and using spin flippers, the polarization may be rotated or flipped. Polarized neutrons have magnetic cross section which generally have spin flip (SF) and non spin flip (NSF) components in all the x, y and z axes. In figure 2.1 the experimental setup for unidirectional polarization analysis is shown. The polarization is directed along the vertical axis z. Four different neutron spin dependent cross sections are measured depending on the status of the spin flippers. Non spin flip (NSF) cross sections are measured when both the flippers are set On or Off. Spin flip (SF) cross sections are measured when only one of the flippers is set On and the other Off. The four different spin

dependent cross section are given by the Moon-Riste-Koehler equations [1, 3]:

$$\begin{aligned}
U^{\uparrow\uparrow} &= b_{coh} - pM_{\perp z} + b_{ii} + \frac{1}{3}b_{si} \\
U^{\downarrow\downarrow} &= b_{coh} + pM_{\perp z} + b_{ii} + \frac{1}{3}b_{si} \\
U^{\downarrow\uparrow} &= -p(M_{\perp x} + iM_{\perp y}) + \frac{2}{3}b_{si} \\
U^{\uparrow\downarrow} &= -p(M_{\perp x} - iM_{\perp y}) + \frac{2}{3}b_{si}
\end{aligned}$$

where  $M_{\perp i}$  indicate the component of the magnetization perpendicular to the  $i$ -axis. The subscripts  $ii$  and  $si$  denote the isotope incoherent and the spin incoherent scattering, respectively.

Magnetic scattering is seen in both the NSF and in the SF channels. The component of the magnetic scattering parallel to  $z$  is NSF while the magnetic scattering perpendicular to  $z$  is SF. Spin incoherent scattering is present in both the channels.

The unidirectional polarization analysis has been used by Andrea Magee to separate the magnon contribution to the cross section from that of phonons in  $\text{MnV}_2\text{O}_4$  [15] (see chapter 6). To do similar investigations on  $\text{Na}_x\text{CoO}_2$  (chapter 5), we used the *XYZ-polarization analysis* technique which is described in more detail in the next paragraph.

#### 2.1.4 The XYZ-technique

The *XYZ* technique or three-directional polarization analysis allows the simultaneous and unambiguous determination of the nuclear, magnetic and nuclear spin-incoherent scattering cross section as a function of both momen-

tum and energy transfer. A typical geometry of the XYZ-technique neutron spectrometer is shown in figure 2.2. A planar multi-detector is placed in the xy plane. The unit scattering vector is given by:

$$Q = [\cos(\alpha), \sin(\alpha), 0] \quad (2.6)$$

where  $\alpha$  is called the Scharf angle, and is the angle between the scattering vector and an arbitrarily chosen x axis [5]. In accordance with the Moon-Riste-Koehler equations [1, 3], the NSF and SF magnetic cross sections for a paramagnet are given by:

$$\begin{aligned} \left( \frac{\partial^2 \sigma}{\partial \Omega \partial E} \right)_{nsf} &= \frac{1}{2} \left( \frac{\partial^2 \sigma}{\partial \Omega \partial E} \right)_{mag} [1 - (\hat{P} \cdot \hat{Q})^2] \\ \left( \frac{\partial^2 \sigma}{\partial \Omega \partial E} \right)_{sf} &= \frac{1}{2} \left( \frac{\partial^2 \sigma}{\partial \Omega \partial E} \right)_{mag} [1 + (\hat{P} \cdot \hat{Q})^2] \end{aligned}$$

where  $\hat{P}$  is the polarization vector. Including the nuclear coherent and isotope incoherent and spin incoherent terms and aligning the polarization of the incident beam alternately along the **x**, **y** and **z** directions, we obtain the expression for the spin dependent cross section for an XYZ polarization analysis measurement:

$$\begin{aligned}
\left(\frac{\partial^2 \sigma}{\partial \Omega \partial E}\right)_{nsf}^x &= \frac{1}{2} \sin^2 \alpha \left(\frac{\partial^2 \sigma}{\partial \Omega \partial E}\right)_{mag} + \frac{1}{3} \left(\frac{\partial^2 \sigma}{\partial \Omega \partial E}\right)_{si} + \left(\frac{\partial^2 \sigma}{\partial \Omega \partial E}\right)_{nuc} \\
\left(\frac{\partial^2 \sigma}{\partial \Omega \partial E}\right)_{sf}^x &= \frac{1}{2} (1 + \cos^2 \alpha) \left(\frac{\partial^2 \sigma}{\partial \Omega \partial E}\right)_{mag} + \frac{2}{3} \left(\frac{\partial^2 \sigma}{\partial \Omega \partial E}\right)_{si} \\
\left(\frac{\partial^2 \sigma}{\partial \Omega \partial E}\right)_{nsf}^y &= \frac{1}{2} \cos^2 \alpha \left(\frac{\partial^2 \sigma}{\partial \Omega \partial E}\right)_{mag} + \frac{1}{3} \left(\frac{\partial^2 \sigma}{\partial \Omega \partial E}\right)_{si} + \left(\frac{\partial^2 \sigma}{\partial \Omega \partial E}\right)_{nuc} \\
\left(\frac{\partial^2 \sigma}{\partial \Omega \partial E}\right)_{sf}^y &= \frac{1}{2} (1 + \sin^2 \alpha) \left(\frac{\partial^2 \sigma}{\partial \Omega \partial E}\right)_{mag} + \frac{2}{3} \left(\frac{\partial^2 \sigma}{\partial \Omega \partial E}\right)_{si} \\
\left(\frac{\partial^2 \sigma}{\partial \Omega \partial E}\right)_{nsf}^z &= \frac{1}{2} \left(\frac{\partial^2 \sigma}{\partial \Omega \partial E}\right)_{mag} + \frac{1}{3} \left(\frac{\partial^2 \sigma}{\partial \Omega \partial E}\right)_{si} + \left(\frac{\partial^2 \sigma}{\partial \Omega \partial E}\right)_{nuc} \\
\left(\frac{\partial^2 \sigma}{\partial \Omega \partial E}\right)_{sf}^z &= \frac{1}{2} \left(\frac{\partial^2 \sigma}{\partial \Omega \partial E}\right)_{mag} + \frac{2}{3} \left(\frac{\partial^2 \sigma}{\partial \Omega \partial E}\right)_{si}
\end{aligned}$$

where the subscripts x, y, and z refer to the directions of the incident polarization and the subscripts *nuc* and *si* refer to nuclear and spin incoherent scattering respectively. The separation of nuclear, spin incoherent and magnetic scattering is obtained through opportune linear combination of the XYZ equations. In particular the magnetic scattering cross section in which we are most interested is given by:

$$\begin{aligned}
\left(\frac{\partial^2 \sigma}{\partial \Omega \partial E}\right)_{mag} &= 2 \left(\frac{\partial^2 \sigma}{\partial \Omega \partial E}\right)_{sf}^x + 2 \left(\frac{\partial^2 \sigma}{\partial \Omega \partial E}\right)_{sf}^y - 4 \left(\frac{\partial^2 \sigma}{\partial \Omega \partial E}\right)_{sf}^z \\
\left(\frac{\partial^2 \sigma}{\partial \Omega \partial E}\right)_{mag} &= 4 \left(\frac{\partial^2 \sigma}{\partial \Omega \partial E}\right)_{nsf}^z - 2 \left(\frac{\partial^2 \sigma}{\partial \Omega \partial E}\right)_{nsf}^x - 2 \left(\frac{\partial^2 \sigma}{\partial \Omega \partial E}\right)_{nsf}^y
\end{aligned}$$

The XYZ equations apply to magnetic systems with both collinear and non-collinear magnetization and randomly oriented moment directions, such as paramagnets, disordered systems and anti-ferromagnets in the polycrystalline



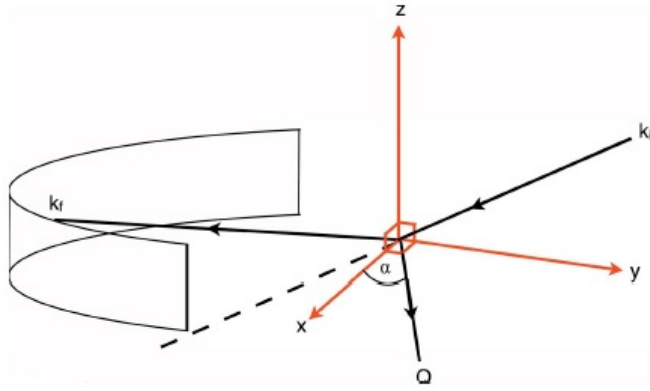


Figure 2.2: *The geometry of an xyz-polarization analysis experiment. The incident polarization is aligned alternately along the directions  $\mathbf{x}$ ,  $\mathbf{y}$  and  $\mathbf{z}$ . The Schärpf angle,  $\alpha$ , is the angle between the wave vector transfer  $\mathbf{Q}$  and the arbitrarily positioned  $x$  axis.*

form in zero external field.

In antiferromagnetically ordered single crystals there is in general a strong correlation between  $x$  and  $y$  components of the sample magnetization which lie in the scattering plane. To achieve separation of the magnetic and nuclear scattering in this case, either the angle between the magnetization and the scattering vector or the magnetic form factor of the sample have to be known in advance [3, 5]. This is the particular case of the  $\text{Na}_x\text{CoO}_2$  which presents an A-type antiferromagnetic structure characterized by the stacking of ferromagnetic layer with spins pointing alternatively parallel or anti-parallel to the  $z$ -direction (see chapter chapter 5).

The XYZ polarization analysis is an extension of uniaxial polarization, so that only the longitudinal component of neutron polarization along the guide field is measured and not the entire polarization tensor as in polarimetry measurements [6]. Therefore, any non-zero magnetization over a long length scale will

result in a reduction of this longitudinal component because of the Larmor precession of the neutrons spin around the sample magnetization. Thus the XYZ-polarization analysis cannot be used to study ferromagnetic systems or a ferrimagnetic system as the  $\text{MnV}_2\text{O}_4$  presented in chapter 6. In this kind of system, in fact, ferromagnetic domains and demagnetization fields depolarize the scattered neutrons. However, uniaxial polarization analysis of single domain ferromagnets (in a saturating field) can be performed in the direction of the sample magnetization [3].

### 2.1.5 Spin-echo

The Neutron Spin Echo (NSE) technique was invented by F. Mezei in 1972 [8]. This technique is able to measure extremely low energy transfers in the range of  $\mu\text{eV}$  to  $\text{neV}$  (time scales of  $10^{-11}$  to  $10^{-7}$  s), which are generally originated by processes such as tunnelling, diffusion, relaxation and random fluctuations. This is achieved without loss of intensity which is the general issue encountered using the conventional inelastic neutron scattering techniques [8]. In contrast to conventional inelastic neutron scattering techniques, in NSE technique the velocity change (the energy transfer) of neutrons after scattering by a sample is measured by comparing the Larmor precession in known magnetic fields before and after the scattering. As the comparison is made for each neutron individually the resolution for measuring the velocity change can be much better than that corresponding to the width of the incident beam. Hence, in a NSE experiment, the width of the incoming beam can be significantly larger than the energy transfer due to the scattering process [8].

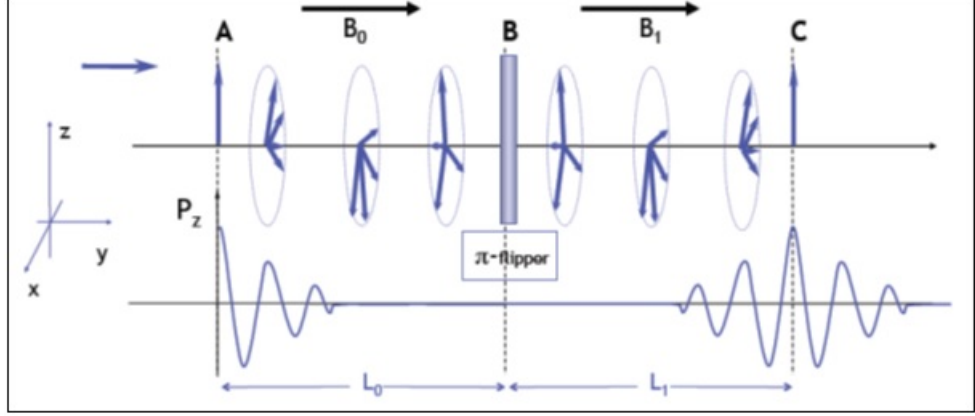


Figure 2.3: *The basic scheme of a NSE spectrometer (top) Spin echo signal (bottom).*

In figure 2.3 the basic scheme of a NSE spectrometer is shown. A broadly monochromatic beam of neutrons is initially polarized along the y-direction. At **A** their spins are flipped through  $\pi/2$  to the z-direction then at this point the beam will be completely polarized along the z-direction. In the space between **A** and **B** the spins precess under the effect of a uniform field  $B_0$  pointing in the y direction. After going through a distance  $L_0$ , each neutron precesses by an amount  $\varphi = \frac{\gamma B_0 L_0}{v}$  where  $v$  is the velocity of the neutron. The polarization of the beam along the z-axis is given by  $P_z = \langle \cos \varphi \rangle$  where the average is performed along the beam velocity distribution. As  $L_0$  increases, the differences between  $\varphi$ 's for different  $v$ 's become bigger and bigger and the Larmor precessions for different neutrons become more and more out of phase. Consequently, for  $L_0$  large enough, the average  $\langle \cos \varphi \rangle$  will tend to zero and the beam will be completely depolarized.

The period of the damped oscillations of  $P_z$  is obviously related to the average beam velocity. At **B** the neutron spins are flipped by  $\pi$  and start to precess in the field  $B_1$ .

At the point **C** the phase will be  $\varphi = \varphi_{AB} - \varphi_{BC} = \gamma \frac{(B_0 L_0 - B_1 L_1)}{v}$  so that for a symmetric configuration with  $B_0 L_0 = B_1 L_1$ ,  $\varphi$  will be zero for all velocities and therefore  $P_z = \langle \cos \varphi \rangle = 1$ .

$P_z$  will show the same damped oscillation behaviour on both side of **C** as that described for the point **A** since differences in  $\varphi$  build up in exactly the same way of moving away from **C**, see figure 2.3. This behaviour of the polarization  $P_z$  is called *spin echo group* while the amplitude of the  $P_z$  oscillation at the symmetry point **C** is called *spin echo signal*,  $P_{NSE}$ . The way  $P_z$  can be measured at **C** consists of flipping the neutron spins by  $\pi/2$  along the y-axis. The NSE group is the cosine Fourier Transform (FT) of the  $\frac{1}{v}$  distribution function which is equivalent to the FT of the wavelength spread of the beam. The narrower is the distribution the more oscillations are contained in the group.

So far we have assumed that the neutrons enter and leave the spectrometer with the same distribution of velocities. This is true only if the scattering by the sample is pure elastic. The presence of inelastic processes changes the energy and thus the velocity of the neutrons. Therefore, the accumulated precession angle is now  $\varphi = \gamma \left[ \left( \frac{B_0 L_0}{v_0} \right) - \left( \frac{B_1 L_1}{v_1} \right) \right]$ . The accumulated precession angle  $\varphi$  can be used as a measure of the energy transfer associated with the scattering process. Since the energy transfer in the scattering process is  $E_1 - E_0 = \hbar\omega = \frac{1}{2}m(v_1^2 - v_0^2)$ , for small energy transfer such as in the quasi-elastic limit, the energy transfer is  $\delta E = \hbar\omega = mv\delta v$  and the velocity of the scattered neutron  $v_1 = v_0 + \delta v_0 = v_0 + \frac{\hbar\omega}{mv_0}$ . This is translated in terms of accumulated precession angle as  $\varphi \cong \gamma \frac{(B_0 L_0 - B_1 L_1)}{v} + \gamma \frac{L_1 B_1 \hbar}{mv^3} \omega$ . Then, for an optimized

spin-echo instrument, the first term vanishes and we have:

$$\varphi = \gamma \frac{L_1 B_1 \hbar}{mv^3} \omega = t_F \omega \quad (2.7)$$

where  $t_F$  is a constant of proportionality which has units of time and it is so called Fourier Time. The essential result of equation 2.7 is that  $\varphi$  depends only on the energy transfer  $\omega$ , which is the relevant parameter for the sample scattering, and it does not explicitly depend on  $v_1$  and  $v_0$  separately. The sample scattering is characterized by the scattering function  $S(\mathbf{k}, \omega)$  which will be assumed to depend only on  $\omega$ , since we are looking at energy the transfer only. The NSE method in its general form can be applied to  $\mathbf{k}$  dependent processes too, like elementary excitations with a general dispersion relation [8]. Anyway this is beyond the scope of this work and we will restrict to the case of  $S$  weakly depending on  $\mathbf{k}$ . The function  $S(\mathbf{k}, \omega)$  describes the probability that the neutrons are scattered with the energy change  $\omega$ , consequently the NSE signal will be given as:

$$P_z = P_S \langle \cos(\omega t_F) \rangle = P_S \frac{\int S(\mathbf{k}, \omega) \cos(\omega t_F) d\omega}{\int S(\mathbf{k}, \omega) d\omega} \quad (2.8)$$

where  $P_S$  takes into account the eventual change in the neutron polarization by the scattering action itself. If there is no spin scattering and no high magnetic fields are involved,  $P_S=1$ . We have to consider that equation 2.8 holds only to first order around  $v_0$  so in a restricted range of  $\delta v_0$ , thus the integration in 2.8 have to be restricted to this range. This means that in practice the

incoming beam has to be roughly monochromatic and eventually an analyser has to be used for the outgoing beam. Thus equation 2.8 shows that the  $P_{NSE}$  correspond to the Fourier Transform (F.T.) of the convolution of  $S(\mathbf{k},\omega)$  with the transmission function of the background spectrometer. The F.T. of a convolution gives a simple multiplication. Therefore, the NSE signal  $P_{NSE}^{eff}(t)$  directly observed from the sample is given by  $P_{NSE}^{eff}(t) = P_{NSE}(t)P_{NSE}^0$  where  $P_{NSE}(t)$  is actually the  $\omega$  cosine F.T. of the scattering function  $S(\mathbf{k},\omega)$  which is called the intermediate scattering  $S(\mathbf{k},t)$ .  $P_{NSE}^0$  is the transmission function of the background spectrometer. In contrast to usual methods, the instrumental resolution effects are taken into account by simple division instead of a tedious de-convolution.

### **Ferromagnetic Neutron Spin Echo (FNSE)**

As already pointed out in the paragraph on polarization analysis, to study a ferromagnetic sample it is necessary to apply a magnetic field to saturate it, to avoid the well known complete depolarization effects [3, 8]. On the other hand, NSE is very sensitive to the presence of a magnetic field in the region outside the precessing coils because it can de-phase the Larmor precession destroying the echo, and it introduces in-homogeneities in the magnetic fields inside the coils [8, 9].

In order to circumvent this problem, we can exploit the non-precessing component of the polarization parallel to the saturating field at the sample  $B_s$ . To do that, the Ferromagnetic Neutron Spin Echo (FNSE) configuration, shown in figure 2.4, is adopted.

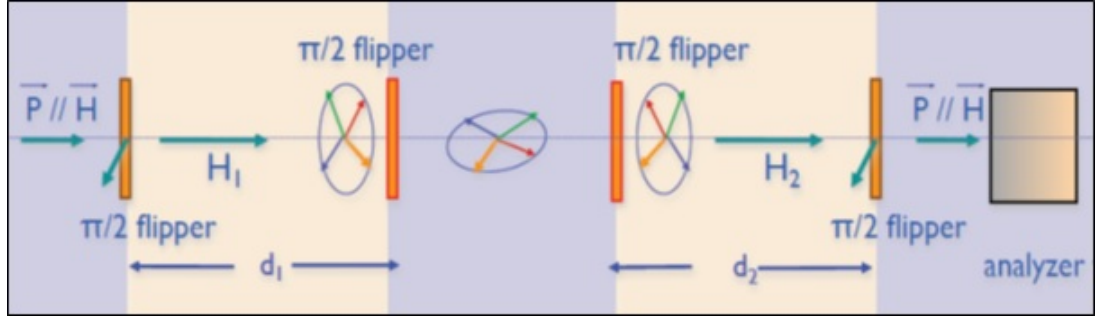


Figure 2.4: *The scheme of the Ferromagnetic Neutron Spin Echo experimental settings.*

Applying a  $\pi/2$  turn to the neutron spins after the region of  $B_0$ , one component of the  $(x, z)$  precessing polarization is turned. Let us assume that the x-component is turned into the z direction. After the scattering this component is turned back by another  $\pi/2$  coil before entering the  $B_1$  region. The other two components are assumed to be completely de-phased in the sample region, hence the spin history between  $B_0$  and  $B_1$  region is:

$$(P_x, P_y, P_z) \xrightarrow{\pi/2} (-P_z, P_y, P_x) \xrightarrow{B_s} (0, 0, P_x) \xrightarrow{\pi/2} (P_x, 0, 0) \quad (2.9)$$

The final polarization  $\mathbf{P}' = (P_x, 0, 0)$  can be considered as the sum of two terms

$$(P_x, 0, 0) = \left(\frac{1}{2}P_x, \frac{1}{2}P_y, 0\right) + \left(\frac{1}{2}P_x, -\frac{1}{2}P_y, 0\right) \quad (2.10)$$

where the first term corresponds to a phase  $\varphi$  equal to that one before the scattering and the second term with a phase opposite in sign which give rise to the echo signal with an amplitude reduce by factor 2 ( $P_s=1/2$ ). We used this method to study the spin dynamics in INVAR  $\text{Fe}_{65}\text{Ni}_{35}$ . This results are presented in chapter 4.

### **2.1.6 Neutron instruments**

#### **The IN20 triple axis spectrometer**

IN20 is a thermal beam triple axis spectrometer at ILL (Grenoble) for inelastic scattering experiments in various sample environments with a maximum applied magnetic field  $B = 15$  T. The scheme of the IN20 spectrometer is shown in figure 2.5. Heavy input slits of adjustable size provide a large solid angle for the monochromatic beam, which together with a sapphire filter window, reduces the fast neutron background. Both the primary and the secondary spectrometer employ a monochromatic horizontal geometry. XYZ polarization analysis is performed using the Heusler 111 crystal as monochromator to select the neutron energy, then a second Heusler 111 analyser is used to determine the properties of the scattered beam. This spectrometer has a  $^3\text{He}$  single detector and parallel-perpendicular polarization analysis can also be used. For this, Helmholtz coils are placed around the sample and a field of about 15 Gauss can be applied in any direction [7]. Full polarization analysis may be employed using CRYOPAD. The IN20 spectrometer is suitable also for high resolution linewidth studies of dispersionless excitation using TASSE, the spin echo technique [7].

#### **The IN11 neutron spin echo spectrometer**

The IN11 is a spin echo instrument at ILL (Grenoble). It is primarily used to study slow relaxation phenomena in polymers, glasses or magnetic materials. Other applications are elastic paramagnetic scattering and the determination



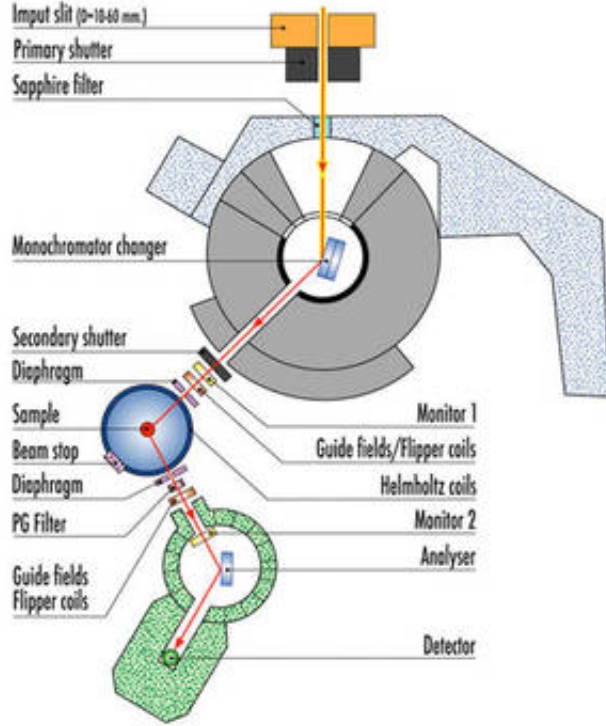


Figure 2.5: *Scheme of the IN20 triple axis spectrometer of ILL [7].*

of phonon linewidths. In figure 2.6 the scheme of the IN11 instrument is shown. Two detector options are available for high Q/energy resolution and high signal, respectively [10]. Option IN11A is a 2-dimensional multi-detector with a pixel size of  $5 \times 5 \text{ mm}^2$  and a detector solid angle of  $0.9^\circ \times 0.9^\circ$ . Also a triple-axis spectrometer may be employed in this option. The option IN11C uses 41 detectors distributed over an angle of  $30^\circ$  and offers a count rate superior by a factor of 20 with the trade off of a lower energy resolution. For a wavelengths of  $4 \text{ \AA}$ , Fourier times in the range of  $0.002 \dots 3 \text{ ns}$  and of  $0.002 \dots 0.5 \text{ ns}$  may be measured using the options IN11A and IN11C, respectively. For our measurements on  $\text{Fe}_{65}\text{Ni}_{35}$  we used the detector option IN11A.

A polarization of 99% is created by supermirrors (FeAg and CoTi super-mirror). The polarization direction is turned perpendicular to the precession

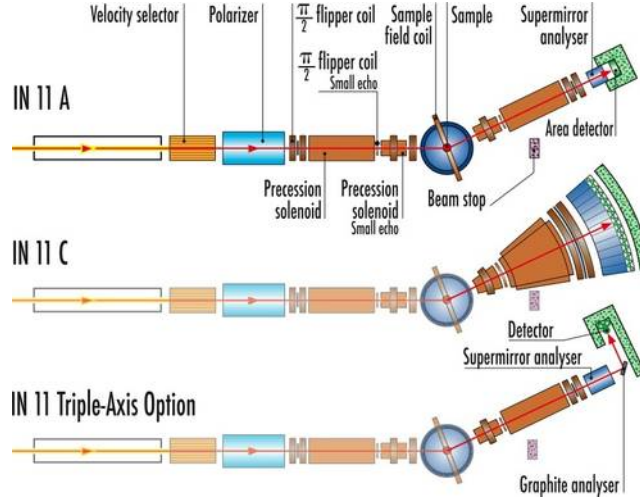


Figure 2.6: *The scheme of the IN11 spin echo spectrometer [10]. The option IN11 A (top) uses a 2-dimensional multi-detector with a pixel size of  $5 \times 5 \text{ mm}^2$  and a detector solid angle of  $0.9^\circ \times 0.9^\circ$ . In this option Also a triple-axis spectrometer may be employed (bottom). The option IN11 A has been used for our measurements on  $\text{Fe}_{65}\text{Ni}_{35}$  (see chapter 4). The option IN11C (middle) instead, uses 41 detectors distributed over an angle of  $30^\circ$  (solid angle detector  $30^\circ \times 1.5^\circ$ ) and offers a count rate superior by a factor of 20 with the trade off of a lower energy resolution.*

fields  $H_0$  and  $H_1$  in the solenoids by two  $\pi/2$ -flipper coils. An additional  $\pi$ -flipper coil allows to keep the fields  $H_0$  and  $H_1$  parallel resulting in higher polarization at small scattering angles [10].

## 2.2 Muon Spin Relaxation Technique $\mu\text{SR}$

Positive muons are unstable leptons with a characteristic lifetime,  $\tau_\mu = 2.2\mu\text{s}$ . They decay via the parity-violating weak interaction in the process:

$$\mu^+ \rightarrow e^+ + \bar{\nu}_\mu + \nu_e \quad (2.11)$$

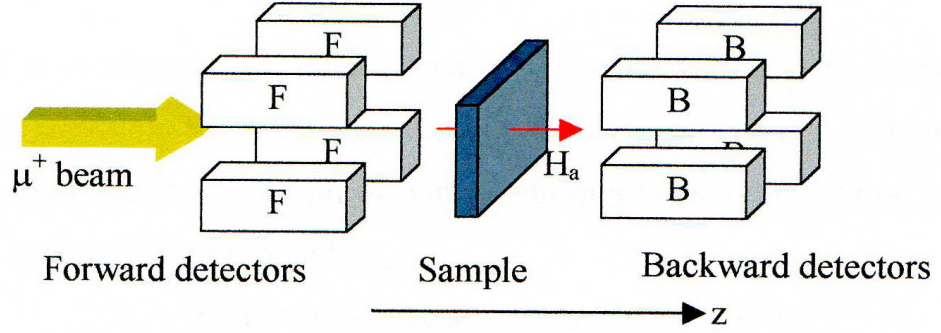


Figure 2.7: *The experimental arrangement for a muon spin relaxation experiment. The  $z$ -direction is defined as the direction of muon motion and initial polarization.  $H_a$  is the direction of the longitudinal field which is turned off during a zero-field measurement [13].*

with the positron emitted preferentially along the muon spin direction at the instant of decay. This particular property is exploited in the muon relaxation ( $\mu$ SR) experiments to study the magnetic properties of condensed matter. In a  $\mu$ SR experiment, muons polarised along their direction of motion, are implanted into the sample under investigation. Because of its positive charge, the muon then localizes at an interstitial site in a time interval much shorter than  $\tau_\mu$  ( $\sim 10^{-10}$ - $10^{-9}$  s) [11]. In this short time interval, the muon maintains its initial polarization. Then the muon spin depolarize under the action of the local magnetic fields until it decays. By collecting several billions of emitted positrons, it is possible to reconstruct the time dependence of the muon relaxation function which is directly related to spatial and temporal distribution of the magnetic field at the muon site. In figure 2.7 the schematic arrangement for a  $\mu$ SR experiment is shown. The positrons emitted after the muon decay, are detected in parallel and antiparallel direction with the respect to the initial

muon polarization. Then we will refer to the forward and backward detectors, respectively. These measurements may be performed either in zero-field (ZF) or with a magnetic field longitudinal to the initial muon polarization. This way of measuring the emitted positrons is called *longitudinal geometry* [12].

The positron counting rates in the two detector banks are given by:

$$N_{F,B}(t) = N_{F,B}(0) \exp\left(-\frac{t}{\tau_\mu}\right) [1 \pm P_z(t)] \quad (2.12)$$

where  $P_z(t)$  is called the *longitudinal muon relaxation function* or *depolarization function*.  $P_z(t)$  is extracted from the measured count rates by calculating the ratio:

$$A_z(t) = a_0 P_z(t) = \frac{N_F(t) - \alpha N_B(t)}{N_F(t) + \alpha N_B(t)} \quad (2.13)$$

where  $\alpha$  is a normalization factor which accounts for the relative efficiencies of the forward and backward detectors and the anisotropic absorption of positrons by the sample and its environments.  $A_z(t)$  is also called asymmetry. The value of  $\alpha$  is determined by performing a *spin-rotation* measurement which consists of applying a magnetic field of a few millitesla perpendicular to the initial muon polarization. Therefore, the muon polarization precesses at the Larmor frequency,  $\omega = \gamma_\mu B$ , consequently the emitted positrons are detected periodically by the forward and backward detector banks. The resulting asymmetry will be an oscillating function modulated by a depolarization envelope,  $G_x(t)$ . The value of  $\alpha$  is found iteratively until the measured asymmetry oscillates around zero [13].

### 2.2.1 Muon Spin Relaxation Function

If the muons are introduced into the sample at  $t=0$  with their spins aligned along the z-axis, then the time evolution of the z-component of the single muon spin is given by the Larmor equation:

$$S_{\mu}^z = \cos^2\theta + \sin^2\theta \cos(\gamma_{\mu} B_{loc} t) \quad (2.14)$$

where  $B_{loc}$  is the magnitude of the local magnetic field experienced by the muon and  $\theta$  is the angle between  $B_{loc}$  and the z-axis. On this equation is based the entire  $\mu$ SR technique. The measured muon depolarization function is given by an ensemble average of  $S_{\mu}^z$  which depends on the particular local magnetic field distribution. For a concentrated disordered arrangement of magnetic moments which are static in the time scale of muon lifetime, the magnetic field distribution is well represented by a Gaussian function. If the random fields are also isotropic, the distribution takes the form:

$$P(B_i) = \frac{\gamma_{\mu}}{(2\pi)^{1/2}\Delta} \exp\left(-\frac{\gamma_{\mu}^2 B_i^2}{2\Delta^2}\right) \quad (2.15)$$

where  $i=x, y, z$  and  $\frac{\Delta^2}{\gamma_{\mu}^2}$  represents the second moment of the distribution.  $\Delta$  can be expressed in terms of interactions between the muon spin and the spins of the compound [12]. The relaxation function in this case assumes this form:

$$P_z(t) = \frac{1}{3} + \frac{2}{3}(1 - \sigma^2 t^2) \exp\left(-\frac{1}{2}\sigma^2 t^2\right) \quad (2.16)$$

The expression is also called the *zero field static Gaussian Kubo-Toyabe function* [14].

Generally the field experienced by the muon is not static and fluctuates in time. The fluctuations of the magnetic field occur as the results of spin dynamics into the sample or the motion of the muon from site to site. In general, one has to consider the simultaneous effect of these two factors. If these fluctuations are fast, the muon will experience many local fields, weighted by their probability distribution. As an effect, the muon will see an average of the total field distribution, thereby reducing the total width of the distribution. This effect is known as *motional narrowing* and it has been observed also in NMR.

The muon diffusion in the sample is normally well described by the *strong collision* model suggested by Kubo et al. In this model the muon jumps from site to site with a mean hopping frequency  $\nu$ , experiencing a sudden change in the local field and there is no correlation between the fields experienced by the muon before and after jumping [14, 15]. Analytical expressions for the muon relaxation function are given in the limit of fast diffusion and very slow diffusion [12]. In particular, in the fast limit with  $\nu/\Delta > 1$  the muon relaxation function is given by

$$P_z(t) = \exp\left(-\frac{2\sigma^2}{\nu^2}[e^{-\nu t} - 1 + \nu t]\right) \quad (2.17)$$

Equation (2.17) in the motional narrowing limit with  $\nu \ll 1/t$  the muon

relaxation function assumes an exponential form

$$P_z(t) = \exp(-\lambda t) \quad (2.18)$$

with  $\lambda = \frac{2\sigma^2}{\nu}$ .

On the contrary, in dynamic spin systems the field modulation can not be assumed as sudden and uncorrelated. In these systems the field modulation is better described by the autocorrelation function. In particular, Kubo and Toyabe in their paper assumed that modulation of the field follow a Gaussian-Markovian process. In other words, the autocorrelation of the fluctuating field is given by a simple exponential form

$$\langle B(t + \tau)B(\tau) \rangle = \frac{\Delta^2}{\gamma^2} \exp(-\frac{t}{\tau}) \quad (2.19)$$

with  $\tau$  the correlation time of the field fluctuation [12, 14, 15]. Under this assumption in the motional narrowing limit, the muon relaxation function is again well described by a simple exponential function

$$P_z(t) = \exp(-\lambda t) \quad (2.20)$$

with  $\lambda$  given by

$$\lambda = \gamma_\mu^2 \Delta^2 \tau \quad (2.21)$$

where  $\tau$  is the fluctuations characteristic time.

We used the muon spin relaxation technique to investigate the spin dy-

namics of  $\text{Fe}_{65}\text{Ni}_{35}$ . These measurements are complementary to the FNSE measurements performed on it.

## 2.2.2 Muons Instruments

### The HIFI muon spectrometer

Figure 2.8 shows the *HIFI* muon spectrometer installed at the ISIS muon facility. The name HIFI is an acronym for high field, in fact this spectrometer is able to perform  $\mu\text{SR}$  measurement in a longitudinal applied field up to 5 T. The magnet which provides this field is a superconducting split-pair, with high field homogeneity over the sample volume and an actively compensated stray field. This spectrometer works mainly in the longitudinal geometry with a field applied parallel to the muon initial polarization. The positrons emitted are detected by two banks of 32 scintillators.

The range of frequency measurable is 0.1-10 MHz and it is limited by the muon pulse width. The HIFI spectrometer allows  $\mu\text{SR}$  measurements at very low temperature (30 mK-6 K) thanks to a dilution refrigerator installed on it. A close circuit refrigerator (CCR) allows measurements in the temperature range from 10 K to 600 K. For high temperature measurements (300-1500 K), a furnace is installed on the HIFI spectrometer [34].

### The EMU muon spectrometer

Figure 2.9 show the *EMU* muon spectrometer installed at the ISIS muon facility. This spectrometer is optimized to perform  $\mu\text{SR}$  measurement in zero



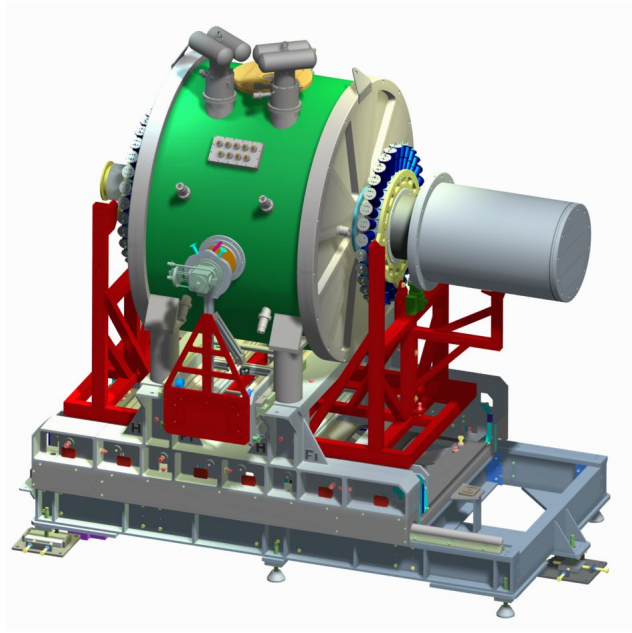


Figure 2.8: *The HiFi muon spectrometer.*



Figure 2.9: *The EMU muon spectrometer.*

field or longitudinal low field around 0.45-0.5 T .The positrons emitted are detected by two banks of 32 scintillators. The range of frequency measurable is 0.1-10 MHz and it is limited by the the muon pulse width. The EMU spectrometer may work both at very low temperature and at high temperature thanks to cryostats, CCR refrigerators and a furnace installed on it [33].

# Bibliography

- [1] G.L. Squires *Introduction to the theory of Thermal Neutron Scattering* (1978) ed. Dover, New York
- [2] G. Ehlers, J.R. Stewart, A.R. Wildes, P.P. Deen and K.H. Andersen *Rev.Sci.Instr.* 84,093901 (2013)
- [3] J.R. Stewart, P.P. Deen, K.H. Andersen, H. Schober, J.F. Barthelemy, J.M. Hillier, A.P. Murani, T. Hayes and B. Lindenau *J. Appl. Cryst.* 42,69 (2009)
- [4] A. Magee Phd Thesis at Royal Holloway University of London *Spin Correlations in Frustrated Magnets with Orbital Ordering* (2011)
- [5] O.Schärpf and Capellmann *Phys. Stat. Sol.* 135,359 (1993)
- [6] M. Blume *Phys. Rev.* 130,1670 (1963)
- [7] <http://www.ill.eu/instruments-support/instruments-groups/instruments/in20/description/layout-of-the-instrument/>
- [8] F. Mezei *The Principles of Neutron spin echo* Proceedings of a Laue-Langevin Institut Workshop Grenoble, October 15-16, 1979 (1980)

- [9] J.B. Hayter *Z.Physik B* 31,117 (1978)
- [10] <http://www.ill.eu/instruments-support/instruments-groups/instruments/in11/>
- [11] T. McMullen and E. Zaremba *Phys. Rev. B* 18,3026 (1978)
- [12] P.D. Reotier and A. Yaouanc *J. Phys. Condens. Matter* 9,9113 (1997)
- [13] J.R. Stewart Ph.D. Thesis *Moment Localization in  $\beta\text{Mn}_{1-x}\text{Al}_x$  St. Andrew university* (1998)
- [14] R.S. Hayano, Y.J. Uemura, J. Imazato, N. Nishida, T. Yamazaki and R. Kubo *Phys. Rev. B* 20,850 (1979)
- [15] R. Kubo and T. Toyabe *Magnetic Resonance and Relaxation ed. by R. Blinc North-Holland Amsterdam* (1967)
- [16] <http://www.isis.stfc.ac.uk/instruments/hifi/hifi2976.html>
- [17] <http://www.isis.stfc.ac.uk/instruments/emu/emu2924.html>

# Chapter 3

## The McPhase software

### 3.1 Introduction

The software McPhase is the program we have used in my thesis to calculate the magnetic structures and excitations in  $\text{Na}_x\text{CoO}_2$  and  $\text{MnV}_2\text{O}_4$ . This program is designed to calculate these properties in magnetic systems with localized magnetic moments given the single magnetic ions configuration and the exchange interaction constants. Figure 3.1 shows an overview of the different modules and related tasks of the package McPhase.

- **solion**, **cfield**, **ic1ion** are modules used to diagonalize the single ion Hamiltonian in different crystal field regimes. The modules **solion** and **cfield** are used in the *weak crystal field* limit, whilst **ic1ion** is used for the *intermediate* and *strong crystal field* limits. These modules can be used even to calculate the thermodynamic properties of a magnetic system in which the multiple ion interactions are negligible.

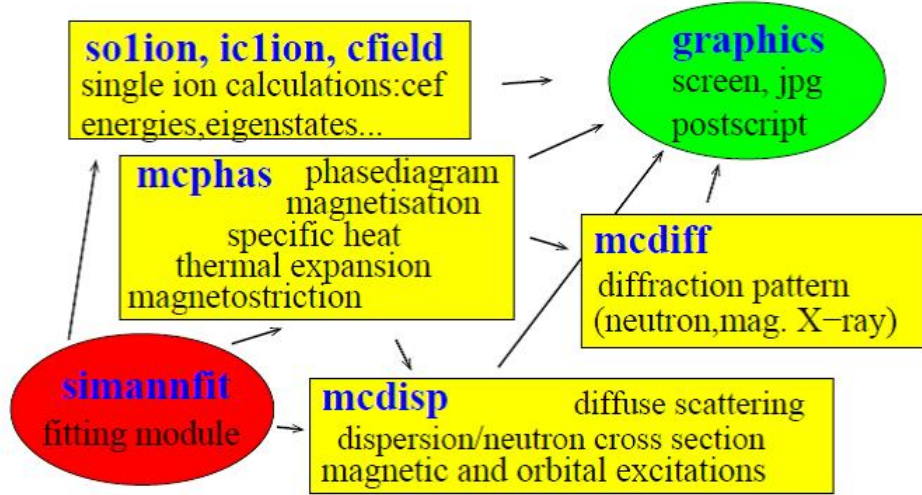


Figure 3.1: *Scheme of the McPhase program packages with modules and relative tasks [2].*

- **mcphas** calculates the thermodynamic properties of magnetic systems involving the single ion modules we mentioned above, considering also the multiple ion interactions, in particular the ion-pair interactions. To do that a combined mean-field/Monte Carlo algorithm is used and this is why this module and the whole software is called McPhase.
- **mcdiff** can be used to calculate the magnetic neutron or resonant X-ray diffraction intensities. Neutron intensities can be calculated going beyond the dipole approximation treatment of the problem. This module has not been used for our calculations and the description of it is beyond the scope of this thesis. For more information see [2].
- The module **mcdisp** can be used to calculate the dispersion and intensity of magnetic excitations and diffuse scattering cross-section. It is based on a mean field-random phase approximation treatment of the problem. I used this program to calculate the spin wave dispersions in  $\text{Na}_x\text{CoO}_2$

and  $\text{MnV}_2\text{O}_4$ .

- **simannfit** is used to determine the parameters of the magnetic Hamiltonian from experimental data, in particular to fit experimental magnetic structure and excitation data. It is based on a simulated annealing algorithm [2].
- **graphics** includes several graphics program to visualize the calculated data.

In the following sections I will give a brief description of the McPhase modules I have used for this thesis work. In particular I will describe the modules **solion**, **ic1ion** and **mcphas** which I used to obtain the ground state magnetic structure of  $\text{Na}_x\text{CoO}_2$  and  $\text{MnV}_2\text{O}_4$ , and the module **mcdisp** that I used to calculate the spin wave dispersions in these two compounds. These dispersions have been directly compared with inelastic neutron scattering data obtained from them. Finally I have used the module **simannfit** to optimize the agreement between experiment and theory.

## 3.2 The Solion and Ic1ion modules

The program modules **solion** and **ic1ion** are used to diagonalize the Hamiltonian of subsystems such as single ions or cluster of ions. The subsystem Hamiltonian,  $\hat{\mathcal{H}}(n)$ , is that of the electrons of the unfilled shell of these ions. These electrons are subjected to four major single-ion interactions: the electron-electron (Coulomb) interaction,  $\hat{\mathcal{H}}_{e-e}$ , the spin-orbit interaction,  $\hat{\mathcal{H}}_{so}$ ,

the crystal field (CF) interaction,  $\hat{\mathcal{H}}_{CF}$ , and eventually the Zeeman interaction,  $\hat{\mathcal{H}}_Z$ , when an external magnetic field is applied. The crystal field interaction is due to the electric field deriving from the neighbouring atoms in the crystal.

Depending on the CF strength relative the electron-electron and spin-orbit interactions, the former or the latter program module is used. The module **solion** is used in the *weak field limit* where the electron-electron and spin-orbit interactions are much stronger than the crystal fields interactions,  $\hat{\mathcal{H}}_{e-e} \gg \hat{\mathcal{H}}_{SO} \gg \hat{\mathcal{H}}_{CF}$ , while the module **ic1ion** is used in the *intermediate* and *strong crystal field* limits where the conditions  $\hat{\mathcal{H}}_{e-e} \gg \hat{\mathcal{H}}_{CF} \gg \hat{\mathcal{H}}_{so}$  and  $\hat{\mathcal{H}}_{CF} \gg \hat{\mathcal{H}}_{e-e} \gg \hat{\mathcal{H}}_{so}$  are respectively, verified.

Both the modules takes as input a file containing the characteristics of the free ion, in particular the number of electrons in the outer shell (valence), the electronic configuration  $nl^\nu$ , the Slater Integrals,  $F_l$  with  $l = 0, 2, 4$ , which give the strength of the electron-electron Coulomb interaction and the spin orbit parameter,  $\lambda$ , (see figure A.1 appendix A ). This file contains the calculated crystal field parameters which can be listed in Stevens or Wybourne notations and the external magnetic field for the Zeeman interaction [2].

### 3.2.1 The module Solion (weak crystal field)

The *weak field limit*,  $\hat{\mathcal{H}}_{e-e} \gg \hat{\mathcal{H}}_{SO} \gg \hat{\mathcal{H}}_{CF}$ , is usually verified in the rare-earth and some localized actinide systems. The single energy levels are calculated in the Russels-Saunders  $LS$  coupling scheme and the CF and the eventual Zeeman interactions are treated as perturbations. The  $\hat{\mathcal{H}}_{e-e}$  splits the energy level of the electrons in the unfilled shell into terms with the same orbital,



$L$ , and spin,  $S$ , quantum numbers, whilst the spin-orbit coupling subsequently splits these terms into multiplets of the same total angular momentum,  $J$ . The multiplets  $|L, S, J, J_z\rangle$  are assumed to be well separated in energy so that there is no mixing between them, and the low temperature properties of the ion may be described by considering just the ground state multiplet. Hence we need only to calculate the splitting of this multiplet due to CF and Zeeman interactions, and that is what the module **solion** does.

The Hamiltonian of the single ion,  $n$ , in this limit consists of two parts:

$$\hat{H}(n) = \sum_{kq} B_k^q(n) \hat{O}_q^k(\hat{J}^n) + g_J^n \mu_B \hat{J}^n \cdot \mathbf{H} \quad (3.1)$$

The first term in the single-ion Hamiltonian equation describes the crystal field (CF). The  $B_k^q(n)$  denote the crystal field parameters which describe the strength of the crystal field whilst the  $\hat{O}_q^k$  with  $k = 2, 4, 6$  and  $q = -k, -k+1, -k+2, \dots, +k$  denote the Stevens operators which are functions of the total angular momentum,  $J$ , that in this limit is a good quantum number [1]. The second term is the Zeeman interaction and describes the action of an external magnetic field  $\mathbf{H}$ .

The crystal field is the electrostatic field which is produced by the charges of the crystal environments of a rare earth ion. It acts on the  $4f$  electrons and causes magnetic anisotropy. The strength of the crystal field is given by the parameters,  $B_k^q$ , which can be calculated using different methods depending on the electronic properties of the magnetic system. In the case of insulating materials these parameters may often be obtained by the *point charge approxi-*

*mation* in which only the electrostatic interactions between the central ion and its surroundings are considered [1]. Bonding and other charge transfer effects, however, mean the actual charges of surrounding ions do not yield accurate crystal field parameters. In these cases the values of the point charges are treated as free parameters and used to fit experimental data. This procedure is quite useful for metals, in which the conduction electrons screen the point charges [1, 3]. The point charge model will reflect the actual symmetry of the crystal field acting on an ion. In Hutchings et al. it is possible to find detailed calculations for particular symmetries (cubic coordination) [1].

A simpler way of dealing with crystal field anisotropy is to write instead of the first term in equation 3.1

$$\sum_s D_x (J_x^s)^2 + D_y (J_y^s)^2 + D_z (J_z^s)^2 \quad (3.2)$$

where the coefficients  $D_i$  are called anisotropy terms. They, in fact, determine the direction of the magnetic moments in a magnetic system with respect to the coordinates axes. This second simpler form of the Hamiltonian is very useful in describing magnetic systems in which the determination of the crystal field parameters is not straightforward and the physics can be described in a simpler way. Some systems in particular have their axis of magnetization aligned along one of the coordinate axes and can be thought a pure spin systems. Many times, in fact, the orbital moment  $L$  is quenched ( $L=0$ ) so that the magnetic properties are determined just by the total spin  $S$  of the magnetic ions. Also in this case the module **solion** can be used and as input it takes a

file which contain just the spin of the modelled magnetic ion and the values of the anisotropies  $D_i$  which can be treated as variable parameters. In chapter 5 I will find that this second approach is very useful in describing the magnetic excitations of sodium cobaltate,  $\text{Na}_x\text{CoO}_2$ . In this conductive material is very difficult to determine the crystal field parameters and the point charge approximation is not enough accurate. Nevertheless the magnetic structure and excitations in sodium cobaltate are well reproduced if it is modelled by a simple spin 1/2 system.

### 3.2.2 The module ic1ion (intermediate and strong crystal field)

The  $LS$  coupling approximation breaks down for transition metal and actinide ions where  $\mathcal{H}_{e-e}$  is weaker because the  $d$  and  $5f$  electron wavefunctions extend further out from the nucleus. This causes some mixing of multiplets of different  $J$  but the same  $L$  and  $S$ . For actinides one can use the j-j coupling approximation, where the relative interaction strengths are assumed to be  $\mathcal{H}_{so} \gg \mathcal{H}_{e-e} \gg \mathcal{H}_{CF} \sim \mathcal{H}_Z$ . In this case  $\mathcal{H}_{so}$  splits the single-electron energy levels into two states with  $j = l \pm s$ . These states are then coupled by the Coulomb interaction and split by the crystal field and Zeeman interactions.

However this approximation cannot account for the magnetic properties of a transition metal ion because for these the crystal field interaction is much stronger than the spin-orbit coupling. Two additional limiting cases of crystal field have to be considered. The *intermediate field* is the case where  $\mathcal{H}_{e-e} \gg$

$\mathcal{H}_{CF} \gg \mathcal{H}_{so}$  and this case may be calculated by the subroutine **icflion** of the module **ic1ion**. In this limit only the lowest energy term of constant  $L$  and  $S$  is considered. The low temperature magnetic properties may be accounted for by the spin-orbit, the crystal field and the Zeeman interactions. The basis states are now  $|L, S, m_l, m_s\rangle$ , and the Hamiltonian in equation 3.1 becomes:

$$\hat{H}(n) = \lambda_n L^n \cdot S^n + \sum_{kq} B_k^q(n) \hat{O}_k^q(\hat{L}^n) + \mu_B (\hat{L}^n + 2\hat{S}^n) \cdot H \quad (3.3)$$

where the Stevens operators for angular momenta  $\hat{O}_k^q(\hat{L}^n)$  must be used in place of those for total angular momentum  $\hat{O}_k^q(\hat{J}^n)$  because we now treat the spin and orbital components separately. We are still considering a manifold of constant  $L$  thus the only difference between  $L$ -Stevens operator  $\hat{O}_k^q(\hat{L}^n)$  and the more usual  $\hat{O}_k^q(\hat{J}^n)$  is in the operator equivalent factors,  $\theta_k^L \neq \theta_k^J$  (see [2, 3] for more details).

Finally, one may consider the full ground state configuration of a particular ion, and thus all allowed,  $L$ ,  $S$  values, by including in addition the Coulomb electron-electron interaction. The single ion Hamiltonian then becomes:

$$\hat{H}(n) = \sum_{k=0}^{2l} F^k(n) \hat{f}_k + \zeta_n \sum_{i=1}^{\nu_n} \hat{l}_i^n \hat{s}_i^n + \sum_{kq} L^q(n)_k \hat{T}_{kq}^n + \mu_B (2\hat{S}^n + \hat{L}^n) \quad (3.4)$$

where the  $\hat{f}_k$  are the Slater operators for the electron-electron Coulomb interaction. The strength of the Coulomb interaction is given by *Slater integrals*,  $F^k$ , which embodies the radial dependence of the electron wavefunction. The angular part is given by the Slater operators  $\hat{f}_k$ . The spin-orbit interaction

is written as a sum of contributions of each electron in the  $l''$  configuration, where  $l = 0, 1, 2, 3 \dots = s, p, d, f \dots$ . The crystal field term is written in term of Wybourne parameters,  $L_k^q$ , and operators,  $\hat{T}_{kq}^n$ . The use of the Wybourne notation in the Hamiltonian 3.4 instead of the Stevens one is due to fact that we are not restricted to a single manifold on constant  $L$ . Crystal field parameters in Wybourne notation can be converted in CF parameters in Stevens notation through the multiplication by opportune factors, see [3] for further details.

In this way is possible to treat the *strong field* limit where the crystal field interaction,  $\mathcal{H}_{CF}$ , dominates over the electron-electron Coulomb interactions,  $\mathcal{H}_{e-e}$ . In this case the crystal field is considered to act first on single-electron states, splitting the degenerate orbital levels  $m_l = -l, \dots, l$ , as dictated by the point symmetry of the ion. For example, in the case of a transition ion in a cubic symmetry the 3d orbitals are usually spilt into a doublet  $|m_l = 0, 2\rangle$ , labelled by the group theoretical irreducible representation of the cubic group  $E_g$ ; and into a triplet  $|m_l = -2, -1, 1\rangle$  labelled  $T_{2g}$ . Electrons may then fill these single electron crystal states, and their degeneracy may be lifted by the Coulomb and the spin-orbit interactions [2].

The module **ic1ion** is used to evaluate the single ion energy levels in this specific case. **ic1ion**, however uses the total orbital and spin angular momenta as labels for the states, rather than single-electron angular momenta or irreducible representations, so it is difficult to interpret **ic1ion** output in this limit.

Furthermore **ic1ion** may be used in the general case, where all three main single ion interactions are considered with variable strengths  $\mathcal{H}_{e-e} \sim \mathcal{H}_{so} \sim$

$\mathcal{H}_{CF}$ , but may also specifically refer to situations in which the strength of the Coulomb and spin-orbit interaction is fixed by parameters determined either from experimental, optical spectra or ab-initio calculations. If the CF interaction is relatively weak, there will be a multiplet structure but the eigenstates of the system are a mixture of the  $LS$ -basis states, with only  $J$  being a good quantum number which can be used to distinguish the states. In case of large CF interaction, however, *J-mixing* can occur, which results in the loss of a distinct multiplet structure.

### 3.3 The core module **mcphas** (Magnetic Phase Diagram calculations)

The module **mcphas** is the core module of the software McPhase and it is used to calculate the phase diagram H-T of a magnetic system. In particular this module includes also the multiple-ion interactions together with the single ion interactions which are treated by the modules described in the first section. If the multiple ion interactions are negligible, it is possible, in first approximation, to calculate the thermodynamic properties of a weakly interacting system using the single ion modules **solion** and **ic1ion**. For a given Temperature, T, and external magnetic field, H, the single ion modules are able to calculate the sum of canonical partition after diagonalizing the Hamiltonian. Then thermodynamic properties such as magnetic susceptibility and specific heat can be easily evaluated.

In the opposite limit when the multiple ion interaction are important, the

program **mcphas** may be used to calculate the ground state magnetic structure and thermodynamic properties. To do that a combined mean-field/Monte Carlo simulation is performed. For a given temperature  $T$  and magnetic field  $H$ , several possible magnetic structures are stabilized by a mean field algorithm and the free energy is calculated. The initial values for this mean-field procedure are modified by a Monte Carlo process.

As input this program takes some files defining the single magnetic ions involved and a file containing the informations on the lattice and exchange parameters (see figure A.2 in the appendix A). The files which define the single magnetic ions are identical to those used by the single ion modules described in the previous paragraph. The single ion modules **solion** or **iclion** are used by the algorithm to calculate the energy levels of the single ions in each step of the Monte Carlo simulation.

### 3.3.1 The Mean-Field Monte Carlo algorithm

We assume a quantum mechanical system that can be described by the Hamiltonian

$$\hat{\mathcal{H}} = \sum_{n=1}^N \hat{\mathcal{H}}(n) - \frac{1}{2} \sum_{n,n',\alpha,\beta} J_{\alpha\beta}(R_{n'} - R_n) \hat{I}_{\alpha}^n \hat{I}_{\beta}^{n'} \quad (3.5)$$

The first term  $\hat{\mathcal{H}}(n)$  denotes the Hamiltonian of a single ion (or a cluster of ions) as those described in the first section. The second term describes a bilinear interaction between different subsystems through the operators  $\hat{I}_{\alpha}^n$ , with  $\alpha = 1, 2, \dots, m$ . The operators indexed by  $n$  act in the subspace  $n$  of

the Hilbert space, thus the commutators between operators with  $n \neq n'$  are all zero. For example, in the case of a Heisenberg exchange between magnetic ions we could identify the set of operators with  $\alpha = 1-3$  with the three components of the spin. The beauty of the analysis which follows is that it can be applied to almost any Hamiltonian of the form 3.5. The analysis of complex magnetic systems can thus be attempted by starting from a simple form such as the Heisenberg model and by introducing, step by step, more complexity into the model. For example, the anisotropy and interactions with an extended range can be introduced by modifying the  $J_{\alpha\beta}(R_{n'} - R_n)$  coefficients.

The main limitation of the approach is that it neglects fluctuations associated with phase transitions and quantum disorder. We are primarily concerned, therefore, with excitations associated with a well-ordered ground state.

In the case of a Bravais lattice the position of the ion,  $n$ , (the subsystem in consideration) can be specified by a lattice vector  $\ell$  and a basis vector  $\mathbf{b}_s$ . The latter is the position of  $n$  relative to  $\ell$ . The calculation of the excited states of the system starts from a mean-field model for the ground state order. We define a mean field acting on each ion by:

$$H_{\alpha}^s = \sum_{\ell' s' \beta} J_{\alpha\beta}(\ell' + \mathbf{b}_{s'} - \ell - \mathbf{b}_s) \langle \hat{I}_{\beta}^{s'} \rangle \quad (3.6)$$

where  $\langle \hat{I}_{\beta}^{s'} \rangle$  represents the thermal expectation value at a temperature  $T$  in the mean field acting on the ion  $s'$ . Note that the mean field is periodic in the lattice, so does not depend on  $\ell$ . The mean field Hamiltonian for the ion  $s$  is



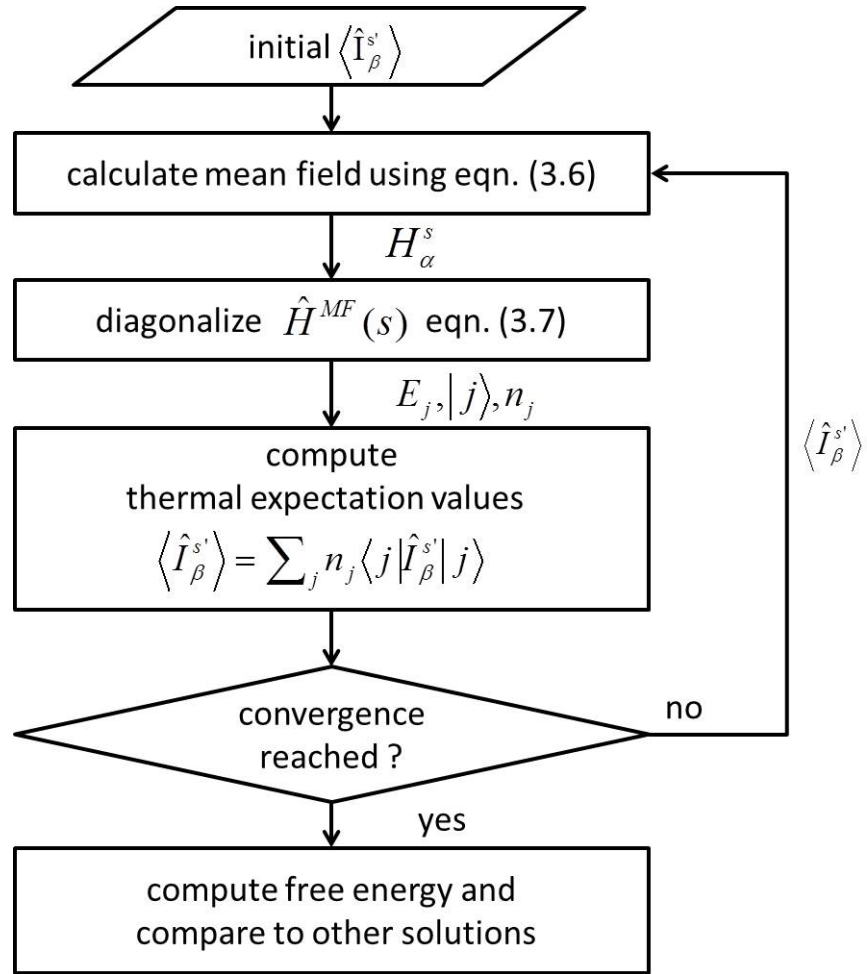


Figure 3.2: *The iterative mean field procedure scheme [3].*

then given by

$$\hat{\mathcal{H}}^{MF}(s) = \hat{\mathcal{H}}(s) - \sum_{\alpha=1}^m H_{\alpha}^s \hat{I}_{\alpha}^s \quad (3.7)$$

The mean-field ground state is obtained from self-consistent solution of 3.6 and 3.7. The iterative procedure is shown in figure 3.2. The mean-field Hamiltonian 3.7 for the ion  $s$  is used to calculate thermal expectation values  $\langle \hat{I}_{\beta}^{s'} \rangle$  for the initial mean field acting on all ion  $s = 1, 2, \dots, m$ . A new set of mean fields is calculated by using 3.6. These are again used in 3.7, and the procedure is repeated until convergence is reached to within some specified precision. The free energy of the mean-field ground state is evaluated and compared to that of other solutions obtained at the same temperature (computed from other initial states). The solution with the lowest free energy corresponds to the stable ground state [3].

### 3.4 The module **mcdisp** (calculation of the spin waves dispersions)

Once a stable ground state magnetic structure is obtained for our system using the program **mcphas**, it is possible to calculate the excited states of the system, in particular with the module **mcdisp** it is possible to calculate the spin wave excitations for a set of given scattering vectors,  $\mathbf{Q}_s$ . To do that the program uses a dynamical matrix diagonalization algorithm which will be described in the next section. The program **mcdisp**, in addition to the energy dispersions, also calculates the relative neutron scattering intensities.

In order to perform this calculation it is necessary to select a specific point in the phase diagram H-T calculated by **mcphas**. This corresponds to the creation of an input file for the program **mcdisp** (see figure A.4 in appendix A) which contains the mean fields at ion sites in the unit cell for the given point on the phase diagram. The program also needs the same input files used by **mcphas**: a file containing the informations on the lattice and exchange parameters and a file defining each single magnetic ion involved. These files are the same files used by the single ion programs described in the first section. These single ion files also contain the neutron magnetic form factor coefficients which are required by the program **mcdisp** to calculate the neutron scattering intensities.

Finally **mcdisp** takes a file with a list of scattering vectors  $\mathbf{Q}$  for which it calculates the excitations, see figure A.3 in appendix A. Furthermore, if in this last file experimentally measured energies are also included with their own error, the program is able calculate the value of the  $\chi^2$  factor. This is very useful if one requires not only qualitative but also quantitative agreement between theory and experiment [2].

### 3.4.1 The calculation of the spin wave dispersions

From linear response theory it can be shown that the excited states are poles of the dynamical susceptibility [4], which is defined by

$$\chi_{BA}(\omega) = \lim_{\varepsilon \rightarrow 0^+} \left[ \sum_{aa'}^{E_a \neq E_{a'}} \frac{\langle a | \hat{B} | a' \rangle \langle a' | \hat{A} | a \rangle}{E_{a'} - E_a - \hbar(\omega + i\varepsilon)} (n_a - n_{a'}) + \frac{i\varepsilon}{\omega + i\varepsilon} \chi'_{BA}(el) \right] \quad (3.8)$$

where

$$\chi'_{BA}(el) = \frac{1}{k_B T} \sum_{aa'}^{E_a=E_{a'}} \langle a | \hat{B} - \langle \hat{B} \rangle | a' \rangle \langle a' | \hat{A} - \langle \hat{A} \rangle | a \rangle n_a \quad (3.9)$$

and

$$n_a = \frac{\exp(-E_a/k_B T)}{\sum_{a'} \exp(-E_{a'}/k_B T)}; \quad \langle \hat{A} \rangle = \sum_a \langle a | \hat{A} | a \rangle n_a \quad (3.10)$$

Here the energy levels and eigenstates of the Hamiltonian are denoted by  $E_a$  and  $|a\rangle$ , respectively.  $n_a$  is the corresponding Boltzmann occupation probability.  $\hat{A}$  and  $\hat{B}$  are quantum mechanical operators describing the perturbation to the Hamiltonian and the response of the system according to the general concepts of linear response theory [4]. The expression 3.8 is based on a system with well defined energy levels implying that the poles of  $\chi_{AB}$  are all lying on the real axis, or that the absorptive part of the response function

$$\chi''_{AB} \equiv \lim_{\varepsilon \rightarrow 0^+} \frac{1}{2i} [\chi_{AB}(z) - \chi_{AB}(-z^*)] \quad (3.11)$$

is a sum of  $\delta$ -functions centred at  $(\hbar\omega = E_{a'} - E_a)$ . In any realistic, interacting system the energy levels are no longer discrete states and fluctuations will cause spontaneous transitions between different levels. Non-zero probabilities for such transition may be accounted for in a phenomenological way by replacing  $E_{a'} - E_a$  in equation 3.8 by  $E_{a'} - E_a - i\gamma_{a',a}$  with  $\gamma_{a',a}$  non-negative. The same result is achieved if  $\varepsilon$  is substituted by a non-negative quantity instead of taking the limit  $\varepsilon \rightarrow 0^+$ . In this approximation the response becomes a sum of Lorentzians.

Because of the periodicity of our system it is convenient to rewrite the

generalized susceptibilities  $\chi_{\alpha\beta}^{ss'} \equiv \chi_{AB}$  in terms of Fourier transform operators defined as:

$$\hat{A} = \frac{1}{\sqrt{N}} \exp(i\mathbf{Q} \cdot \mathbf{b}_{s'}) \sum_{\ell'} \exp(i\mathbf{Q} \cdot \ell') \hat{I}_{\beta}^{(\ell's')} \quad (3.12)$$

$$\hat{B} = \frac{1}{\sqrt{N}} \exp(i\mathbf{Q} \cdot \mathbf{b}_s) \sum_{\ell} \exp(i\mathbf{Q} \cdot \ell) \hat{I}_{\alpha}^{(\ell s)} \quad (3.13)$$

where  $N$  is the number of unit cells. For the same reason we also introduce the Fourier transform of the two-body interaction

$$J_{\alpha\beta}^{ss'}(\mathbf{Q}) = \sum_{\ell'} J_{\alpha\beta}(\ell' + \mathbf{b}_{s'} - \mathbf{b}_s) \exp\{i\mathbf{Q} \cdot (\ell' + \mathbf{b}_{s'} - \mathbf{b}_s)\} \quad (3.14)$$

We have arbitrarily chosen  $\ell = 0$  since  $J(\mathbf{Q})$  is the same for all  $\ell$  due to the translational symmetry.

The calculation of the dynamical susceptibility  $\chi_{\alpha\beta}(\mathbf{Q}, \omega)$  from the Hamiltonian 3.5 is carried out within the mean field-random phase approximation (MF-RPA) [4, 5]. This approximation neglects correlations in the difference  $\hat{I}^n(t) - \langle \hat{I}^n(t) \rangle$  of different subsystems  $n$  (in our case ions). In this approach the dynamical susceptibility for a primitive lattice ( $s=s'=0$ ) can be calculated from the solution of the following equation:

$$1 = [\bar{\chi}^0(\omega)^{-1} - \bar{J}(\mathbf{Q})] \bar{\chi}(\mathbf{Q}, \omega) \quad (3.15)$$

where  $\bar{\chi}^0(\omega)$  is the usual single-ion magnetic susceptibility tensor. This equation can be rewritten in index notation for several subsystems  $s = 1, 2, \dots, N_b$

(in our case the different ions in the primitive cell) as:

$$\delta_{\alpha\beta}\delta_{ss'} = \sum_{s''=1}^{N_b} \sum_{\delta=1}^m \left[ \delta_{ss''} [\chi^s(\omega)]_{\alpha\delta}^{-1} - J_{\alpha\delta}^{ss''}(\mathbf{Q}) \right] \chi_{\delta\beta}^{s''s'}(\mathbf{Q}, \omega) \quad (3.16)$$

where  $\chi_{\alpha\beta}^s$  is the subsystem susceptibility given by:

$$\chi_{\alpha\beta}^s(\omega) = \sum_{jj'} \frac{\langle j | \hat{I}_\alpha - \langle \hat{I}_\alpha \rangle | j' \rangle \langle j' | \hat{I}_\beta - \langle \hat{I}_\beta \rangle | j \rangle}{\epsilon_{j'} - \epsilon_j - \hbar\omega} (n_j - n_{j'}) \quad (3.17)$$

where for more readability the index  $s$  has been omitted on the right-hand side.  $\epsilon_j$  and  $\epsilon_{j'}$  are energy levels of the subsystem  $s$  as calculated self-consistently within the mean-field theory using the Hamiltonian 3.7,  $|j\rangle$  and  $|j'\rangle$  denote the corresponding eigenstates and  $n_j$  the corresponding populations. This expression of the generalized susceptibility is identical to the expression 3.8 if  $\epsilon_{j'}$  is replaced by  $\epsilon_{j'} + d$  in all terms where  $\epsilon_{j'} = \epsilon_j$  with  $|d| \ll k_B T$  after taking the limit  $\varepsilon \rightarrow 0^+$ .

The main problem in applying the MF-RPA is the calculation of the dynamical susceptibility  $\chi_{\alpha\beta}^{s''s'}(\mathbf{Q}, \omega)$  from equation 3.16. The direct method is to substitute the expression 3.17 in equation 3.16, which is then solved for each desired value of  $\omega$  and  $\mathbf{Q}$  by inverting this matrix. To avoid numerical divergences, it is necessary to add to  $\hbar\omega$  a small imaginary part  $\hbar\omega + i\gamma$ . This method is inefficient and time consuming, in fact it requires the inversion of a  $3N_B \times 3N_B$  matrix for each  $(\mathbf{Q}, \omega)$  in the calculation.

In order to minimize the computational effort, **mcdisp** uses an algorithm which requires only the solution of a single generalized eigenvalue problem at

each scattering vector  $\mathbf{Q}$ . This algorithm is called *dynamical matrix diagonalization* (DMD) and it was in the first instance developed to solve dynamical equations describing the oscillation of modes on a crystal lattice (phonons) [6].

In the following we describe the DMD for a single excitation  $\epsilon_- \longrightarrow \epsilon_+$  of each subsystem  $s$ , i.e. we assume that each subsystem is a two-level system with a single transition only. Other transitions (terms in 3.17) can be considered in the DMD formalism by assigning to each of these transitions an additional value of the index  $s$  and increasing the total number of subsystems ( $N_b$ ) correspondingly.

For readability it is convenient to adopt the following matrix notation: an  $m \times m$  matrix is indicated by a bar on top of the symbol, so that  $\overline{\chi}^s$  refers to a matrix  $\chi_{\alpha\beta}^s$  with  $\alpha, \beta = 1, \dots, m$ . An  $N_b \times N_b$  matrix is denoted by a bar below the symbol. Making use of these two conventions the dynamical susceptibility  $\chi_{\alpha\beta}^{ss'}(\mathbf{Q}, \omega)$  can be written as  $\underline{\overline{\chi}}(\mathbf{Q}, \omega)$ . Moreover, omitting the bar refers to the '11'-component of the matrix, e.g.  $\chi^{ss'} \equiv \chi_{11}^{ss'}(\mathbf{Q}, \omega)$ .

If we consider only a single excitation  $\epsilon_- \longrightarrow \epsilon_+$  in the subsystem susceptibility, equation 3.17 is simply:

$$\overline{\chi}^s(\omega) = \frac{\overline{M}^s}{\Delta^s - \hbar\omega} \quad (3.18)$$

with  $\Delta^s = \epsilon_+^s - \epsilon_-^s$  and the transition matrix element

$$M_{\alpha\beta}^s = \langle -|\hat{I}_\alpha^s - \langle \hat{I}_\alpha^s \rangle|+ \rangle \langle +|\hat{I}_\beta^s - \langle \hat{I}_\beta^s \rangle|- \rangle (n_- - n_+) \quad (3.19)$$

The  $m \times m$  matrices  $\overline{M}^s$  may be diagonalized giving eigenvalues which are all zero except for one real eigenvalue  $\gamma^s$  (which have the same sign of  $\Delta^s$ ):

$$\gamma^s = \text{Tr}\{\overline{M}^s\} \quad (3.20)$$

Now, for the MF-RPA problem equation 3.16 may be simplified by using the unitary transformation  $\overline{U}^s$  ( $\overline{U}^{s\dagger}\overline{U}^s = \mathbb{1}$ ), which diagonalizes  $\overline{M}^s$ . Note that the first column of this matrix  $\overline{U}^s$  (the eigenvector with the eigenvalue  $\gamma^s$ ) is simply

$$\mathcal{U}_{\alpha 1}^s = \sqrt{(n_- - n_+)/\gamma^s} \langle -|\hat{I}_\alpha^s - \langle \hat{I}_\alpha^s \rangle_{\mathbf{H},T}|+ \rangle \quad (3.21)$$

This property is very useful as most of the equations below require only knowledge of this first column. With a similar procedure one may transform the subsystem interaction  $J_{\alpha\beta}^{ss'}(\mathbf{Q})$

$$\overline{\mathcal{L}}^{ss'}(\mathbf{Q}) \equiv \overline{U}^{s\dagger} \overline{J}^{ss'}(\mathbf{Q}) \overline{U}^{s'} \quad (3.22)$$

Now the  $N_b \times N_b$  Hermitian dynamical matrix may be defined as

$$A^{ss'}(\mathbf{Q}) \equiv \Lambda^{ss'} \Delta^s - \sqrt{\gamma^s} \overline{\mathcal{L}}^{ss'}(\mathbf{Q}) (\sqrt{\gamma^s})^* \quad (3.23)$$

The energies of the system may be calculated by solving the following generalized eigenvalue problem:

$$\underline{A}(\mathbf{Q}) \underline{\mathbf{t}} = \hbar\omega \underline{\Lambda} \underline{\mathbf{t}} \quad (3.24)$$



where the matrix  $\underline{\Lambda}$  is defined as

$$\Lambda^{ss'} \equiv \delta_{ss'} \text{sgn}(\Delta^s). \quad (3.25)$$

The solution of the generalized eigenvalue problem 3.24 yields the eigenvectors  $\underline{\tau} = (\mathbf{t}^1, \mathbf{t}^2, \dots, \mathbf{t}^r..)$  and eigenvalues  $\hbar\omega^r$  which correspond to the excitation energies of the system at the wavevector  $\mathbf{Q}$  for which  $\underline{A}(\mathbf{Q})$  was calculated. The solution of the eigenvalue problem 3.24 corresponds to the diagonalization of the dynamical matrix in the case of phonons, and therefore this method for calculating magntic excitations is called dynamical matrix diagonalization.

The eigenvector matrix  $\underline{\tau}$  provides a unitary transformation, which may be used to obtain the dynamical susceptibility, see[14]. If eigenvectors are normalized as  $\underline{\tau}^\dagger \underline{A} \underline{\tau} = 1$ , then equation 3.16 can be transformed using  $\bar{\mathcal{U}}^s$  and  $\underline{\tau}$ :

$$\chi_{\alpha\beta}^{ss'}(\mathbf{Q}, \omega) = (\sqrt{\gamma^s})^* \sum_r \mathcal{U}_{\alpha 1}^s \tau^{sr}(\mathbf{Q}) \frac{\hbar\omega^r(\mathbf{Q})}{\hbar\omega^r(\mathbf{Q}) - \hbar\omega} \tau^{sr'\dagger}(\mathbf{Q}) \mathcal{U}_{1\beta}^{s'\dagger} \sqrt{\gamma^{s'}}. \quad (3.26)$$

By its definition, the generalized susceptibility gives information about the correlated movement of the operators  $\langle \hat{I}_\alpha^s \rangle$  for a specific excitation and contains the relative phases and amplitudes of the different operators. The procedure for the calculation of the excitation energies  $\hbar\omega^r$  and physical observables (such as correlation function and spectra) outlined above is very fast, because it involves only a single diagonalization for every scattering vector of interest.

Figure 3.3 shows the DMD algorithm of which we have described only

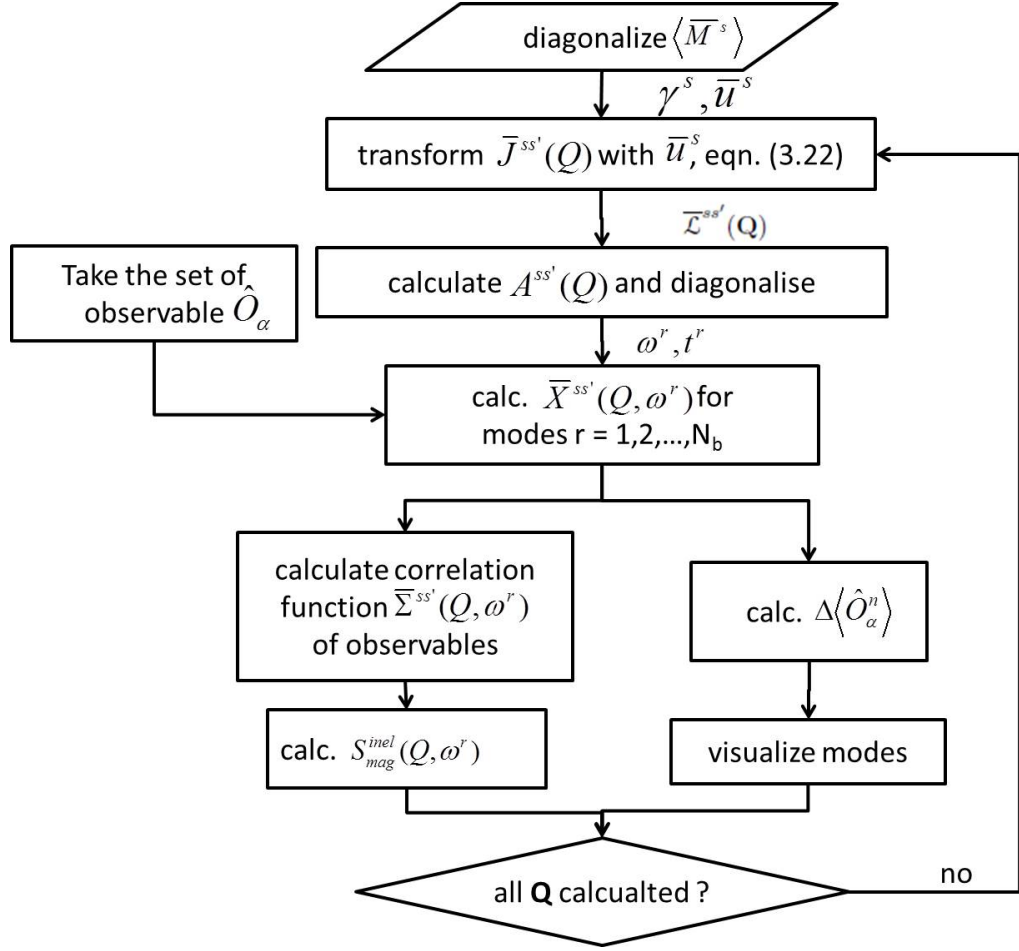


Figure 3.3: Scheme of the DMD algorithm [3].

the first three parts necessary to obtain the eigenvectors  $\mathbf{t}^r$  and eigenvalues  $\hbar\omega^r$ . The other parts are described in [14]. The same procedure can be used to calculate a general susceptibility  $\bar{X}(\mathbf{Q}, \omega)$  corresponding to an arbitrary observable, from which physical properties may be calculated.

# Bibliography

- [1] M.T. Hutchings et al *Solid State Phys.* 16,227 (1964)
- [2] [http://www.cpfs.mpg.de/~rotter/homepagemcphase/manual/  
manual.html](http://www.cpfs.mpg.de/~rotter/homepagemcphase/manual/manual.html)
- [3] M. Rotter et al. *J. Phys. Condens. Matter* 24,213201 (2004)
- [4] J. Jensen and A. R. Mackintosh *Rare Earth Magnetism* Oxford Clarendon  
(1991)
- [5] S.V. Tjablikov *Methods in the Quantum Theory of Magnetism* New York  
Plenum (1967)
- [6] M. Rotter *Comput. Mater. Sci.* 38, 400-4 (2006)

# Chapter 4

## Spin Fluctuations in INVAR

### $\text{Fe}_{65}\text{Ni}_{35}$

#### 4.1 Introduction to the INVAR effect

In 1987 C.E. Guillaume established that face-centred-cubic (fcc) alloys of iron and nickel with  $\sim 35\%$  of nickel exhibit an anomalously small thermal expansion over a wide range of temperature [1]. He considered the expansion of these alloys to be 'invariable' hence this kind of behaviour has since become known as the INVAR effect. The same effect has since been observed also in various ordered and random alloys and even in amorphous materials [2]. There is a wide range of applications in which INVAR alloys are used because of this useful property; for example in the realization of measuring tapes, in the springs of mechanical watches. Nevertheless a clear understanding of the mechanism behind this effect is still lacking. The INVAR effect is clearly related to ferromagnetism [2, 3] in these alloys. Below the Curie temperature,

their coefficients of linear expansion are typically around  $\alpha \sim 2.1 \times 10^{-6} \text{ K}^{-1}$ , while in the paramagnetic phase, they are one order of magnitude greater than this value.

The first model to describe the INVAR effect, was suggested by Weiss and is called the  $2\gamma$ -state model [3]. It is based on the coexistence two nearly degenerate magnetic states in f.c.c. iron ( $\gamma$ -Fe): a high spin, high volume state and a low spin, low volume state. The thermal excitations between these two states are supposed to compensate for lattice expansion coming from the anharmonic components of the lattice vibrations.

Modern electronic band theory calculations confirm the main idea of the  $2\gamma$ -state model. First-principle calculations of  $\gamma$ -Fe, random ordered  $\gamma$ -Fe-Ni and ordered  $\text{Fe}_3\text{Ni}$  alloys clearly show the existence of two stable magnetic states, a low-spin low-volume (LS) and a high-spin high-volume (HS) state [4, 5]. In particular Ental et al. predicted a change in the relative occupancy between the anti-bonding  $t_{2g}$  majority spin states and the non-bonding  $e_g$  minority spin states in favour of the latter as the temperature increases [4]. This results in the contraction of bonds, thereby counteracting the thermal expansion. This provides a useful explanation of the magneto-volume effect responsible for the near zero thermal expansion in INVAR system.

However, the existence of these spin states has not been observed at ambient pressure in any INVAR material. Only recent X-ray magnetic circular dichroism (XMCD) measurements on  $\text{Fe}_{72}\text{Pt}_{28}$  under high pressure, revealed that the system undergoes a magnetic transition at an applied pressure of 4 GPa (40 kbar), commensurate with that expected to occur during a high spin

(HS) to low spin (LS) transition [6, 7]. Other X-ray diffraction measurements have shown that the non-INVAr system Pd<sub>3</sub>Fe exhibits INVAr properties at high pressure [8]. On the other hand, spin polarized neutron diffraction measurements performed at atmospheric pressure on Fe-Ni Invar alloys [9, 10] have shown that the fraction of unpaired electrons with  $e_g$  symmetry remains constant in a range of temperature from 100-600 K, contradicting the theoretical results of Ental et al. [4].

Both theoretical works such as the unified theory of spin fluctuation by Moriya et al. [11, 12] and magnetostriction measurements [13, 14, 16] established that the INVAr effect is a result of a large magneto-volume effect associated with the variation in amplitude of the local magnetic moment  $\langle M_{loc}^2(T) \rangle$ , which compensates for the normal thermal expansion.

Motivated by the research of the excitations responsible of the INVAr effect, Ishikawa et al. performed inelastic neutron scattering measurements on the INVAr alloys Fe<sub>65</sub>Ni<sub>35</sub> and Fe<sub>3</sub>Pt and on the non-INVAr Fe<sub>50</sub>Ni<sub>50</sub>. They observed that in INVAr Fe<sub>65</sub>Ni<sub>35</sub> and Fe<sub>3</sub>Pt spin wave excitations explain only about a half of the temperature decrease of the magnetization while this discrepancy is absent in non-INVAr Fe<sub>50</sub>Ni<sub>50</sub> (see figure 4.1)[17, 18].

On the basis of their results they suggested that the variation in amplitude of the local magnetic moment and then the INVAr effect may be due to the presence in these alloys of some *hidden (undetected) excitation*. Nevertheless no other kind of magnetic excitations which may originate the INVAr effect have been observed. Stoner excitations appear at too high an energy ( 100 meV) to be responsible for the INVAr effect [15, 18, 19, 20]. Longitudinal

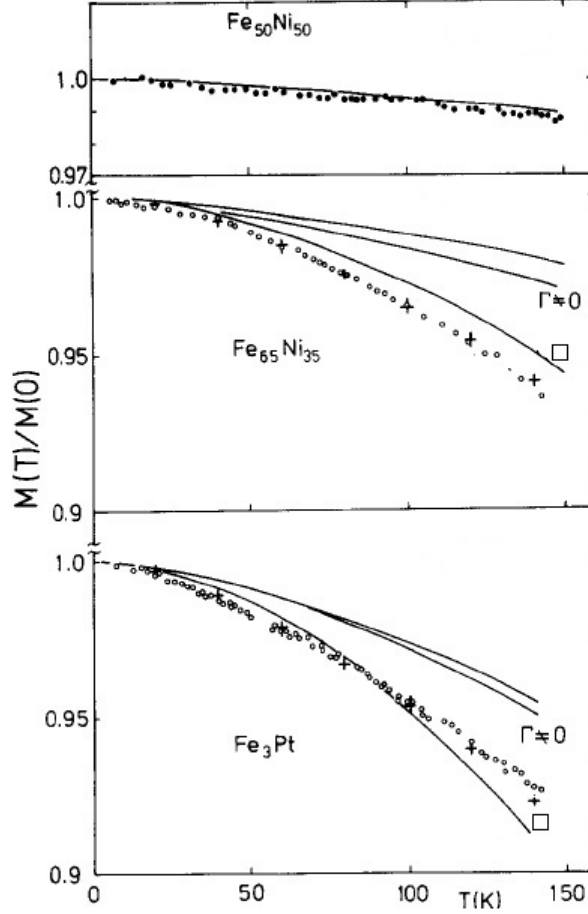


Figure 4.1: Temperature dependence of the magnetizations of the non-INVAR alloy  $\text{Fe}_{50}\text{Ni}_{50}$  and the INVAR alloys  $\text{Fe}_{65}\text{Ni}_{35}$  and  $\text{Fe}_3\text{Pt}$  calculated by spin wave theory using the magnon dispersion  $\hbar\omega_q = D(T)q^2$  experimentally obtained (solid lines and (+) ) and magnetizations measured on the same samples (open and closed circles). Satisfactory agreement is achieved only for the  $\text{Fe}_{50}\text{Ni}_{50}$ . In the case of the INVAR alloys  $\text{Fe}_{65}\text{Ni}_{35}$  and  $\text{Fe}_3\text{Pt}$  the agreement remains poor even if the line broadening of the magnon dispersion (line marked with  $\Gamma \neq 0$ ) and the presence of an optical mode close to the acoustic one is considered (line marked with  $\square$ ). Satisfactory agreement also for the INVAR  $\text{Fe}_{65}\text{Ni}_{35}$  and  $\text{Fe}_3\text{Pt}$  is achieved only if additional 'hidden' excitations with the same dispersion relation of magnons are included (+). [17].

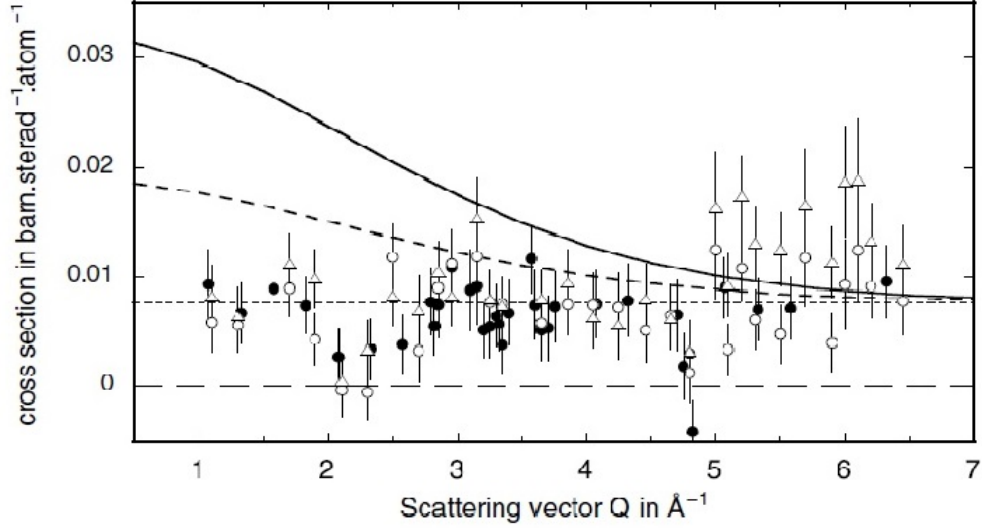


Figure 4.2: *The average spin-flip cross-sections are plotted in absolute units for three data sets: filled circles at 1.4 T, 300 K; open circles at 2 T, 300 K; triangles at 2 T, 4.2 K. The horizontal dotted line is the effective nuclear spin incoherent scattering cross-section. The dashed and the solid curve are the predicted magnetic contributions to the cross-section for two different non-collinear models consistent with the calculations of Schilfgaard et. [30].*

spin fluctuations have also been ruled out because they were observed only in INVAR  $\text{Fe}_{65}\text{Ni}_{35}$  and not in INVAR  $\text{Fe}_3\text{Pt}$  in which the INVAR effect is even stronger [21].

More recent theoretical studies suggest, instead, that the INVAR effect is related to thermal magnetic disorder. Two main models of magnetic disorder have been proposed in literature: the disordered local moment (DLM) and the canted spins model. Disordered local moments are defined as random arrangements of two distinct magnetic states of the same atomic species in a metallic system, one with the spin pointing parallel and the other antiparallel to the magnetization direction [22, 23, 24, 26, 27]. The other model is based on presence of non-collinearity in the magnetic structure, i.e. spins may be canted with respect to the average magnetization direction [30].



Schilfgaarde et al., for example, using an ab-initio electronic structure approach, find in INVAR concentrations of Fe-Ni alloys a magnetic structure characterized, even at zero temperature, by a continuous transition from a ferromagnetic state at high volumes to a disordered non-collinear configuration at low volumes [30]. The non-collinearity gives rise to anomalies in the binding energy volume dependence curve which is directly related to the thermal expansion coefficient through the bulk modulus and Grüneisen constant. This anomalous behaviour of the binding energy results in a magneto-volume effect able to explain the INVAR effect.

Nonetheless the presence of non-collinearity has been confirmed experimentally only at low  $Q$  [31]. In fact, polarized neutron diffraction measurements have shown that in the range of  $Q$  ( $1 < Q < 6.5 \text{ \AA}^{-1}$ ) INVAR  $\text{Fe}_{65}\text{Ni}_{35}$  looks like a simple collinear ferromagnet [28]. This is clearly shown in figure 4.2. The spin flip (SF) neutron cross section which accounts only for the spin components perpendicular to the magnetization, is close to zero and independent of  $Q$  at different temperatures and applied magnetic fields (see [28]).

On the other hand, Menshikov et al. observed a high intensity spin flip (SF) signal at low  $Q$  for a sample of INVAR  $\text{Fe}_{65}\text{Ni}_{35}$ . Moreover they observed an increase of the signal intensity as a function of temperature, see figure 4.3 [31, 32]. In non-INVAR  $\text{Fe}_{50}\text{Ni}_{50}$  this feature was absent. On the basis of this observation Menshikov et al. concluded that in the INVAR  $\text{Fe}_{65}\text{Ni}_{35}$  magnetic structure non-collinear in-homogeneities are present and have a size of  $10\text{-}15\text{ \AA}$ . They suggested a model magnetic structure characterized by the occurrence of static spin fluctuations embedded in a ferromagnetic matrix. The

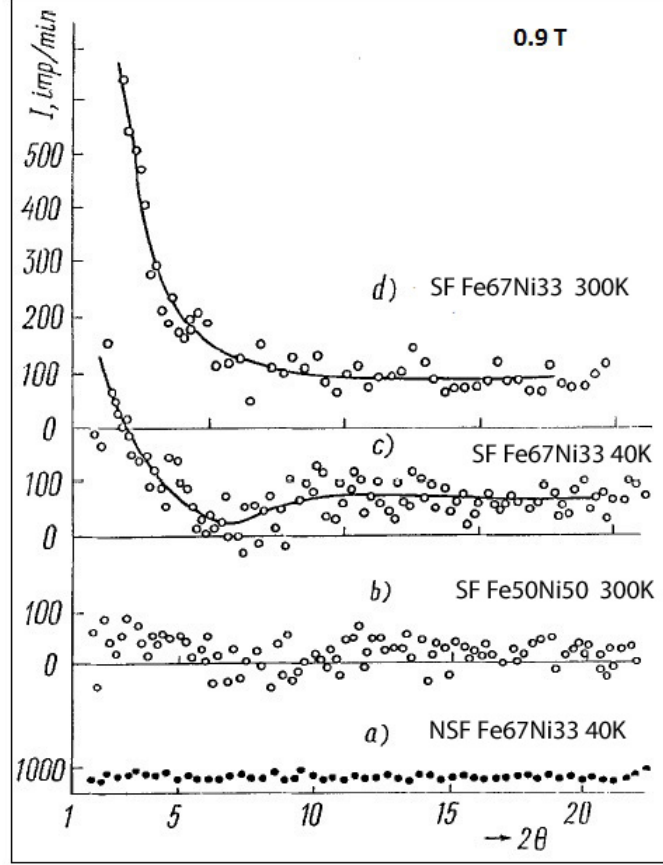


Figure 4.3: The angular dependence of the non-spin-flip (NSF) (a) and the spin-flip (SF) scattering (b), (c) and (d) for  $\text{Fe}_{1-x}\text{Ni}_x$  alloys. (a)  $\text{Fe}_{67}\text{Ni}_{33}$  (40 K); (b)  $\text{Fe}_{50}\text{Ni}_{50}$  (300 K); (c)  $\text{Fe}_{67}\text{Ni}_{33}$  (40 K); (d)  $\text{Fe}_{67}\text{Ni}_{33}$  (300 K). The neutron polarization and the magnetization of the sample were set parallel to the scattering vector [32]. SF signal is sensitive to the spin components which are perpendicular to the magnetization, while NSF scattering is sensitive to the nuclear scattering. The presence of high intensity SF signal for INVAR  $\text{Fe}_{67}\text{Ni}_{33}$  at two different temperatures, (c) and (d)), is evidence of magnetic non-collinearity in this sample. This is not observed in non-INVAR  $\text{Fe}_{50}\text{Ni}_{50}$  (b) [32].

centres of such fluctuations are iron atoms surrounded only by atoms of the same species in the nearest coordination sphere. These fluctuations are due to antiferromagnetic iron-pair interactions in accordance with previous spin wave measurements [29].

Finally recent ab initio electronic structure calculations based on the disordered local moment (DLM) approach, gives a good description of the INVAR effect in Fe-Pt [26] and RCo<sub>2</sub> with R= Dy, Ho alloys [23]. In particular in the work of Mohn et al. on Fe-Pt alloy, the presence of two distinct magnetic states of the iron is allowed. The INVAR effect in Fe-Pt seems to be entirely related to the thermal magnetic disorder modelled as DLM. The anomaly in the temperature dependence of the magnetization, in this framework, is well explained by a spontaneous reduction of local magnetic moment rather than by the suggestion of *hidden excitations* (see figure 4.1) [26]. This approach looks promising also in describing the INVAR effect in the Fe-Ni alloys. Probably the presence of in-homogeneities seems to complicate the solution of this problem.

Further improvements in the description of INVAR effect on Fe-Ni, Fe-Pt and Fe-Pd alloys using the DLM approach, have been achieved by Liot et al. [27]. In particular they have used the density functional theory (DFT) to evaluate the free energy of alloys in DLM states as a function of lattice constant for different temperature. Moreover they considered also the effects of lattice vibrations and estimated them within the Debye-Grüneisen model. The calculated thermal expansion coefficients for these INVAR alloy results in qualitative agreement with those obtained experimentally as shown in figure

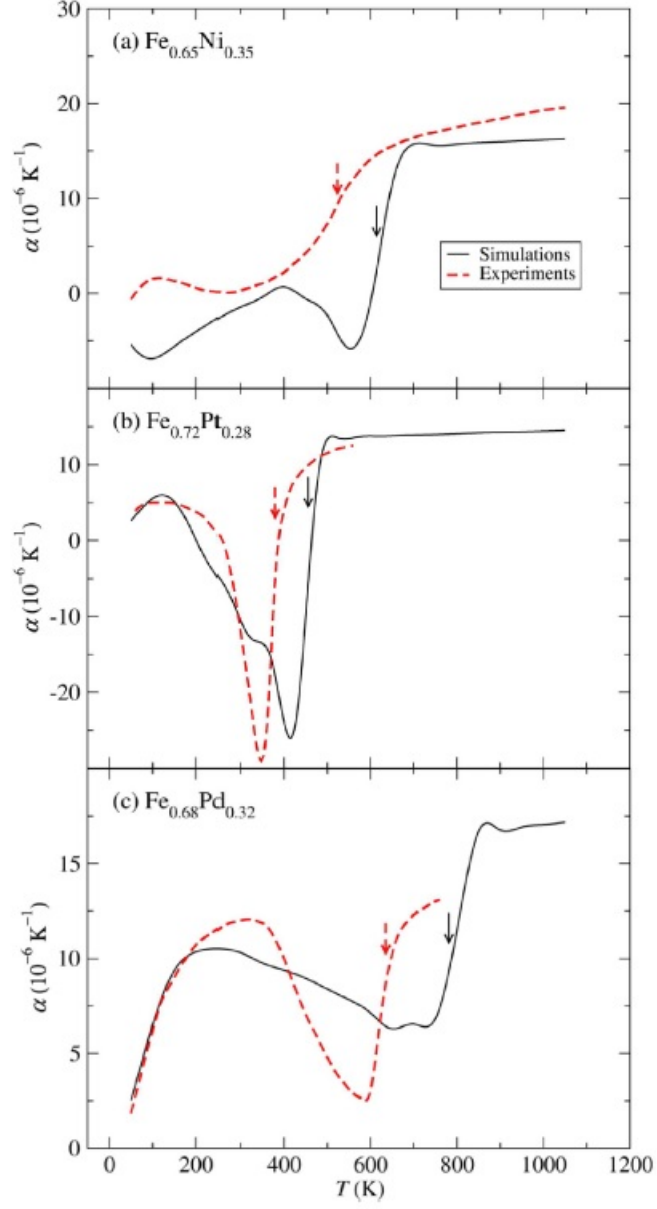


Figure 4.4: *Linear thermal expansion coefficient of fcc ferromagnets calculated by Liot et al. in the DLM approach. Vertical arrows indicate Curie temperatures.* [27]

#### 4.4.

Nevertheless there are also cases in which the DLM approach does not result in good agreement with the experimental results [25]. More importantly there is still a lack of experimental evidence that may or may not give credence to the role of disordered local moments in the INVAR phenomena.

In order to shed more light on the importance of spin dynamics in INVAR and on the role played by the magnetic disorder and the eventual presence of non-collinearity in INVAR  $\text{Fe}_{65}\text{Ni}_{35}$ , we performed muon spin relaxation ( $\mu\text{SR}$ ) and ferromagnetic neutron spin echo (FNSE) measurements on this system. As shown on chapter 2, if the implanted muon diffuses through the sample at high temperature (300) K it could become sensitive to the domain structure. Moreover, if a longitudinal magnetic field is applied it could reveal the presence of non-collinearity. On the other hand a static muon is sensitive to the magnetic field correlation at the muon site (see chapter 2) and this provides useful information on the local spin fluctuations. FNSE measurements instead provide valuable information on the microscopic origin of spin fluctuations; which may range from local spin dynamics, to large scale cluster dynamics. In particular the FNSE should reveal the characteristic time and distance scales of fluctuations.

## 4.2 Experimental procedure

The samples were prepared by melting appropriate quantities of starting materials with purity of 99.99 in an argon-arc furnace. The as-melted in-

gots were then annealed at 800 C for 72 hours followed by a slow cool. The stoichiometry of the samples was verified by performing energy dispersive fluorescence analysis using a commercial scanning electron microscope. For the FNSE experiment a  $\text{Fe}_{65}\text{Ni}_{35}$  sample with a mass of about 100 gr, was mounted in the Spin-Echo spectrometer IN11 of I.L.L. (Grenoble) described in detail in chapter 2. A vertical saturating vertical field of 1 T was applied to preserve the neutron polarization. The dependence on temperature of the intermediate scattering function  $S(Q,t)/S(Q,0)$  was measured using a monochromatic source with  $\lambda=5.5 \text{ \AA}$  at a scattering angle  $2\Theta=4^\circ$ .

The zero field (ZF)  $\mu\text{SR}$  measurements on INVAR  $\text{Fe}_{65}\text{Ni}_{35}$  were performed at the EMU ISIS facility, while the longitudinal field (LF)  $\mu\text{SR}$  measurements were done at the HIFI ISIS facility. The  $\text{Fe}_{65}\text{Ni}_{35}$  sample was mounted on a silver plate whose depolarization function is taken as time independent because silver has no electronic moment and a very small nuclear moment. In order to measure the temperature dependence of the muon depolarization rate we used a closed cycle refrigerator (CCR) able to cool the samples to 10 K or heat them to 600 K. For the longitudinal field measurements we used a 5 T cryogen-free superconducting magnet installed on the HIFI spectrometer.

### 4.3 Results and Discussions

In figure 4.5 are displayed the results of the FNSE measurements performed on the INVAR  $\text{Fe}_{65}\text{Ni}_{35}$  sample under an applied field of 1 T in order to create a single domain magnetic structure hence preserve the neutron polarization. The

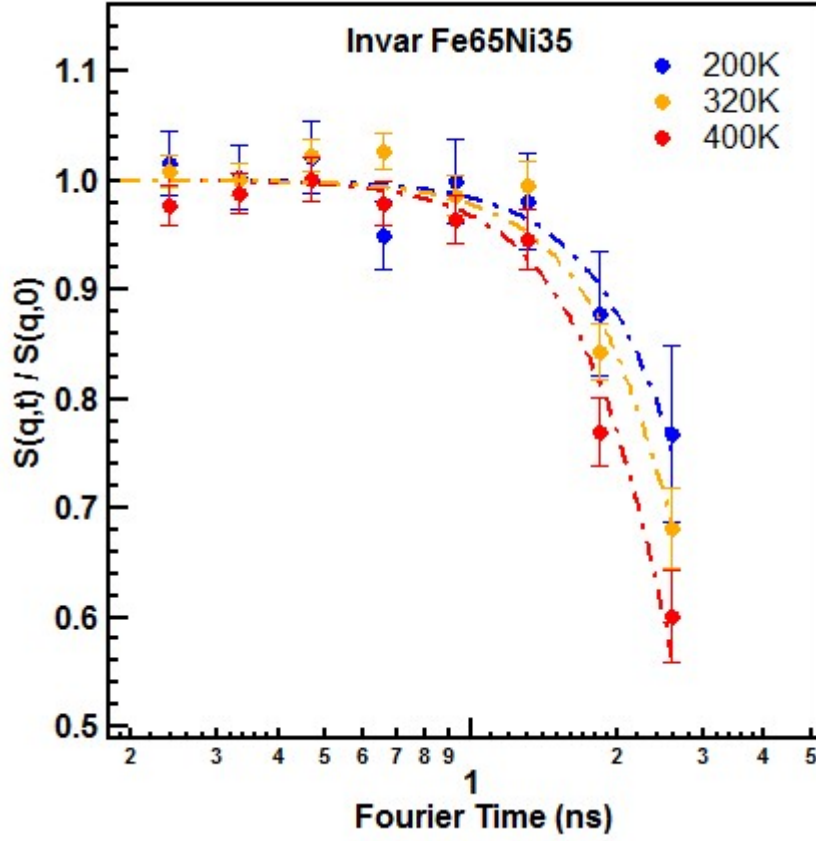


Figure 4.5: *FNSE* measurements performed on the *INVAR* sample. The normalized intermediate scattering function  $S(q,t)/S(q,0)$  starts to decrease rapidly after a time of  $\simeq 0.7$  ns (the dashed lines are guides for the eyes). This means in *INVAR*  $\text{Fe}_{65}\text{Ni}_{35}$  there are spin dynamics with a characteristic time of the order of nanoseconds. This characteristic time decreases as a function of temperature.

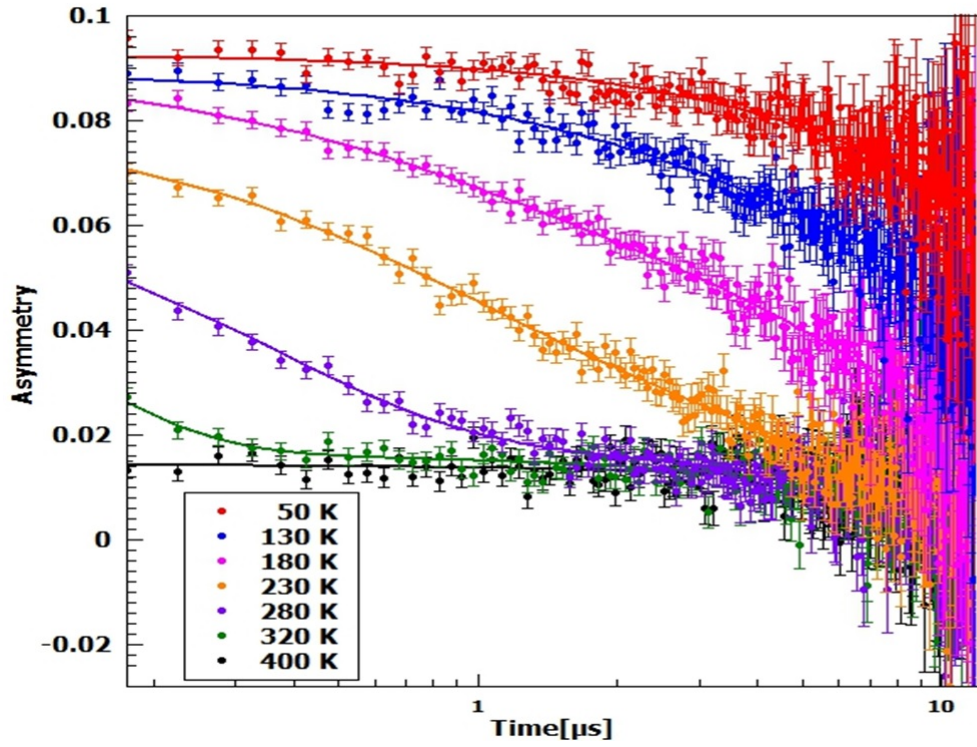


Figure 4.6: Zero field muon relaxation spectra taken at different temperatures. They are fitted to the sum of two exponential functions  $a_i \exp(-\lambda_i t)$  where  $\lambda_i$  and  $a_i$  are muon relaxation rates and initial asymmetries respectively.



normalized intermediate scattering function looks flat up to 0.7 ns then it starts to decrease steeply. This decrease is enhanced on increasing the temperature as clearly shown in figure 1 by the guide lines. This suggests the presence of low-frequency spin dynamics in INVAR  $\text{Fe}_{65}\text{Ni}_{35}$  with a characteristic time scale of the order of nanoseconds (energy 1-10  $\mu\text{eV}$ ). The characteristic time of these spin dynamics is lowered when the temperature increases. This characteristic time is obtained by fitting the data with an exponential relaxation function. From the FNSE measurements we can only conclude that at low  $Q$  ( $\sim 0.08 \text{ \AA}^{-1}$ ) INVAR  $\text{Fe}_{65}\text{Ni}_{35}$  in the ordered magnetic state exhibits spin dynamics with characteristic time of the order of nanoseconds.

In figure 4.6 are shown some examples of ZF  $\mu\text{SR}$  spectra. The ZF spectra are well fitted by the sum of two exponential relaxing functions  $a_i \exp(-\lambda_i t)$ . Muon relaxation rates  $\lambda_i$  and initial asymmetries  $a_i$  are plotted as function of the temperature in figure 4.7 and 4.8 respectively.

The presence of two muon relaxation rate suggests the presence of two time scales. The time scale of one of the exponential functions is in the range 1-10 MHz and we identify it as *fast* (red circles) while the other is in the range of 0.03-0.1 MHz and consequently we identify it as *slow* (yellow circles). Below 100 K the spectrum is well fitted by a single relaxation component and it is not possible to deduce which of the two components persists in this temperature range. For simplicity we kept only the *slow* relaxation component. The *fast* component relaxes at a value of approximately 1 MHz up to 230 K at which point it starts to increase. At roughly the same temperature the *slow* component reaches a peak maybe due to a dynamical transition such as a spin

freezing. Above 230 K the *fast* component further increases reaching 10 MHz at 330 K then above this temperature the spectrum is again well fitted by the single *slow* component. This is because the *fast* component dynamics at a certain temperature moves beyond the upper limit of measurable frequencies at EMU ( $\simeq 10$  MHz) [33]. In figure 4.8 the corresponding initial asymmetries of the two relaxation functions are shown. The asymmetry corresponding to the fast component increases as a function of temperature up to  $\simeq 230$  K where it saturates at a constant value of  $\simeq 0.054$ . The asymmetry corresponding to the slow component is higher at low temperature with a value of  $\simeq 0.09$ , then decreases above  $\simeq 100$  K reaching the minimum constant value of  $\simeq 0.014$  beyond  $\simeq 250$  K.

In figure 4.9 are shown the fits results of the  $\mu$ SR spectra measured in an applied longitudinal magnetic field (LF) at HIFI. In this regime the spectra are well fitted by a single exponential function and the dynamics is no longer characterized by two well separated time scales as in the ZF case. In fact for each applied field the muon depolarization rate is characterized by a single component that monotonically increases from an order of magnitude of 0.01-0.1 MHz at low temperature and overcomes the upper limit of measurable frequencies ( $\simeq 10$  MHz) at highest temperatures [34]. In the case of an applied field of 2.0 T this process start from 0.01 MHz around 150 K reaching the upper limit at 375 K while for the applied fields of 0.5 T and 1.0 T it starts from 0.1 MHz around 150 K and overcomes the upper limit at  $\simeq 300$  K. The application of longitudinal magnetic field seems to remove the *slow* component

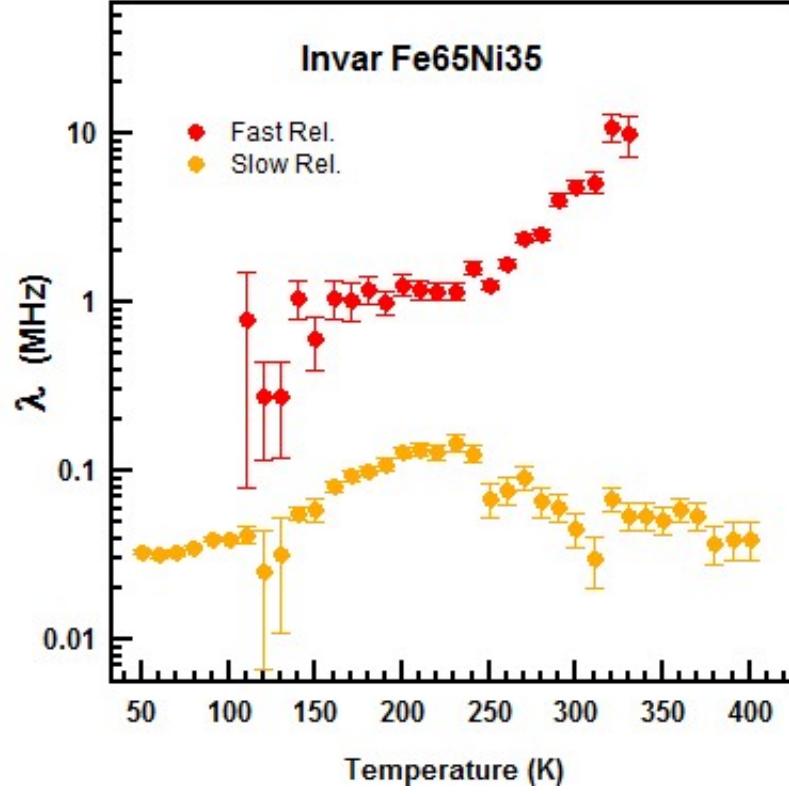


Figure 4.7: Zero field muon relaxation rate components obtained from the sum of two exponential functions, for each fit we have chi square per degree of freedom,  $\chi^2_{red} \cong 1$ . The fast component (red circles) at  $\simeq 230$  K starts to increase overcoming the upper limit of measurable frequencies at EMU ( $\simeq 10$  MHz) at  $\simeq 330$  K. The slow component (yellow circles) instead displays a broad peak in temperature ( $\simeq 230$  K) suggesting the presence of a spin dynamics transition in INVAR  $Fe_{65}Ni_{35}$  such spin-freezing.

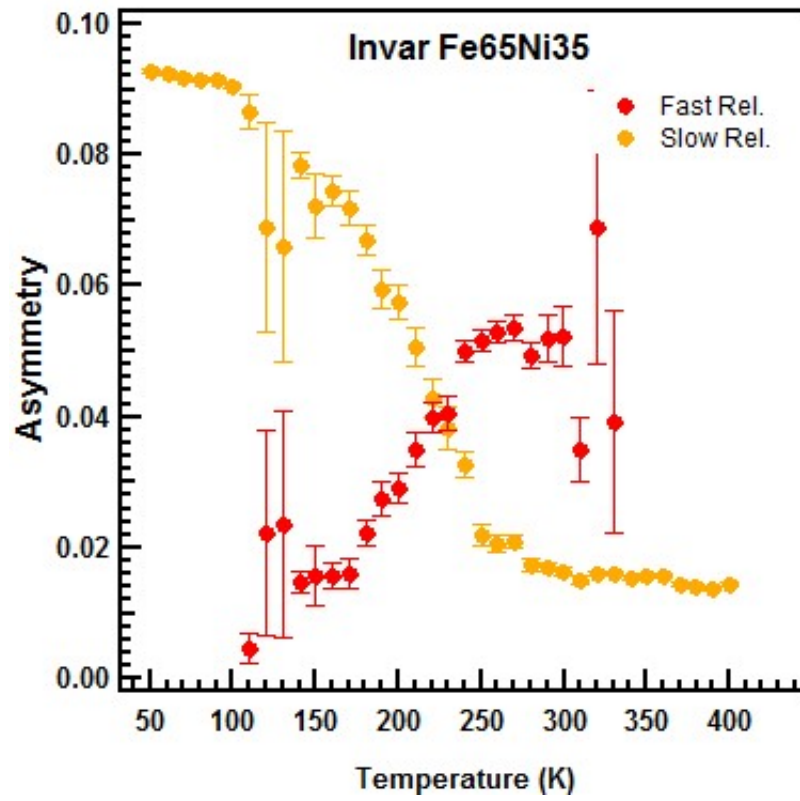


Figure 4.8: Zero field initial asymmetries corresponding to the fast component (red circles) and the slow component (yellow circles).

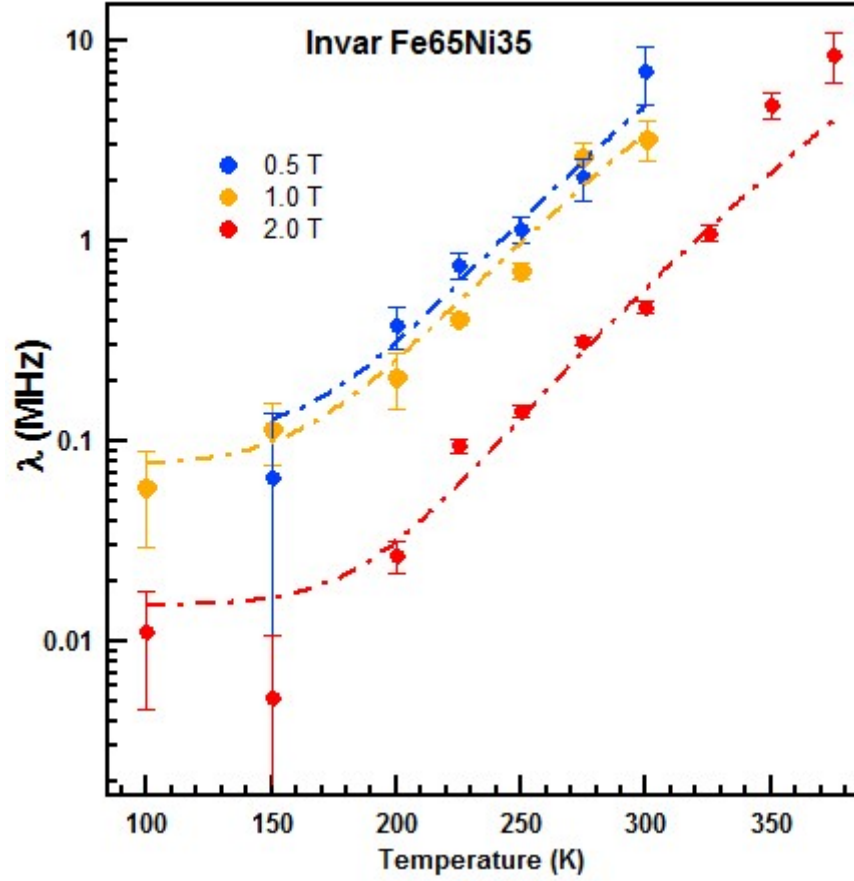


Figure 4.9: Muon depolarization rates under an applied longitudinal field of 0.5 T (blue circles), 1 T (yellow circles) and 2 T (red circles). In the longitudinal field regime, spectra are well fitted by a single component,  $\chi_{red}^2 \cong 1.08$ .

of the spin dynamics. In fact, the single muon relaxation rate observed in LF exhibits a behaviour very similar to that of *fast* component in ZF. Further investigations are necessary to verify this hypothesis.

The  $\mu$ SR measurements both in ZF and in LF confirm the presence of low-frequency spin-dynamics in INVAR Fe<sub>65</sub>Ni<sub>35</sub> in agreement with the previous FNSE measurements. Furthermore ZF  $\mu$ SR measurements suggest the coexistence of two well separated times scales of spin-dynamics. The dependence on temperature of the corresponding initial asymmetries shows that, below 100 K, the spin dynamics are dominated by the slower process then increasing the temperature this contribution is lowered in favour of the fast spin dynamical process. At 230 K the contribution of these two time scales of spin-dynamics is the same, then the fast one becomes dominant reaching a stable maximum asymmetry at 250 K. The slow one at roughly the same temperature reaches a stable minimum value.

The *fast* component of the spin dynamics may be associated with individual spin excitations. In conventional ferromagnets, a peak at  $T_c$ , in the T dependence of muon depolarization rate is expected to occur because of critical spin fluctuations around the phase transitions. The increase of the *fast* component around 250 K may be the onset of this peak ( $T_c \simeq 490$  K for the INVAR Fe<sub>65</sub>Ni<sub>35</sub>). In order to check this, further  $\mu$ SR measurements could be performed in a temperature range which includes  $T_c$  and using an instrument sensitive to higher frequencies than the maxima measurable at the pulsed muon beam EMU and HIFI ISIS facilities (10 MHz). The ALC facility at PSI continuous muon source may be a candidate for that.

The *slow* component instead may be associated with the dynamics of non-collinear magnetic inhomogeneities observed in INVAR  $\text{Fe}_{65}\text{Ni}_{35}$  by Menshikov et al. using the polarized neutron diffraction technique [32]. On the basis of their results, Menshikov et al. proposed a magnetic structure characterized by spin fluctuations similar to a spin glass, embedded in a ferromagnetic matrix. Centres of such fluctuations are iron atoms surrounded by the same sort of atoms in the nearest coordination sphere [31]. These fluctuations are due to the presence of anti-ferromagnetic iron-pair interactions,  $J_{\text{Fe}-\text{Fe}} < 0$ , together with  $J_{\text{Ni}-\text{Ni}} > 0$ ,  $J_{\text{Ni}-\text{Fe}} > 0$  as shown by previous spin waves studies [29]. So that, in this framework, the *fast* muon relaxation component may be associated with the ferromagnetic matrix dynamics (spin waves) while the *slow* one, with the magnetic inhomogeneities observed in Invar  $\text{Fe}_{65}\text{Ni}_{35}$ .

These inhomogeneities seem related to the INVAR effect, in fact the related compound  $\text{Fe}_{50}\text{Ni}_{50}$  is an homogeneous ferromagnet as shown by polarised neutron measurements. Thus the slow spin dynamics observed may be the origin of the INVAR effect. However in order to confirm this, it is necessary to perform similar spin dynamics investigations on the related compound  $\text{Fe}_{50}\text{Ni}_{50}$ .

Other models which have explained in a satisfactory way the INVAR effect in Fe-Pt alloys and in  $\text{RCO}_2$  with  $\text{R} = \text{Dy}, \text{Ho}$ , are based on the disordered local moments (DLM) approach [22, 26, 27]. DLM are defined as a random arrangement of two distinct magnetic states of the same atomic species in a metallic system. The *slow* component of the muon relaxation rate may be related to the the dynamics of the disordered local moments and may be, thus, associated to the INVAR effect. Nevertheless similar spin dynamics investigation such as

$\mu$ SR measurements on the related compound  $\text{Fe}_{50}\text{Ni}_{50}$ , are necessary in order to check the suggested explanation. Another aspect that needs to be clarified, is the effect of an applied magnetic field on the spin dynamics and eventually on the INVAR effect. In the LF regime the *slow* component is suppressed, indicating that the spin dynamics related to the inhomogeneities or to the DLM is suppressed. Possibly the application of a longitudinal field removes the magnetic inhomogeneities and therefore the associated spin dynamics. This may be checked by performing dilatation measurements of  $\text{Fe}_{65}\text{Ni}_{35}$  as a function of applied field. These studies may be also complementary to the  $\mu$ SR measurements suggested above.

Finally the spin dynamics observed by the FNSE measurements under an applied field of 1 T, should correspond to the *fast* component observed in the  $\mu$ SR experiment. The *slow* component has a characteristic time too long to be revealed by NSE [35]. However, further zero field NSE measurements may provide additional information on the *fast* component time scale spin dynamics.

In conclusion we performed FNSE measurements on INVAR  $\text{Fe}_{65}\text{Ni}_{35}$  revealing the presence in this system of low frequency spin dynamics with a characteristic time of the order of nanoseconds.  $\mu$ SR measurements confirm the presence of spin dynamics both in ZF and in LF. Furthermore ZF  $\mu$ SR measurements suggest the presence of a second well separated time scale of spin-dynamics: a *fast* one in the range of 1-10 MHz and a *slow* component in the range of 0.1 MHz. The first one may be associated to individual spin fluctuations and corresponds to that one measured by NSE. The second one



instead may be related to magnetic structure, non-collinear inhomogeneities or the presence of disordered local moments (DLM). Under an applied longitudinal magnetic field the *slow* component is suppressed.

# Bibliography

- [1] C.E. Guillaume *CR acad.Sci.* **125**,235 (1897)
- [2] E.F. Wasserman *Ferromagnetic Materials* **5**,237 (1990)
- [3] R.J. Weiss *Proc.R.Soc.Lond.* **A 82**,281 (1963)
- [4] P. Entel, E. Hoffmann, P. Mohn, K. Schwarz and V.L. Moruzzi *Phys.Rev.B* **47**,8706 (1993)
- [5] J.Kasper and Salahub, *Phys.Rev.Lett.* **47**,54 (1981)
- [6] S. Odin, F. Baudalet, Ch. Giorgetti, E. Dartyge, J.P. Itie, A. Polian, C.J. Chervin, S. Pizzini, A. Fontaine and J.P. Kappler *Euro.Phys.Lett.* **47**,378 (1999)
- [7] S. Odin et al. *Phil.Mag.* **B 80**,155 (2000)
- [8] M.L. Winterose et al. *Phys.Rev.Lett.* **102**,237202 (2009)
- [9] P.J. Brown. K.R.A. Ziebeck and K.U. Neumann *J.Phys.Cond.Mat.* **13**,1563 (2001)
- [10] Y.Ito, J.Akimitsu, M.Matsui and S.Chikazumi *JMMM* **10**,194 (1979)

- [11] T. Moryia and K. Usami *Solid State Comm.* **34**,95 (1980)
- [12] A.R. Williams, V.L. Moruzzi, C.D. Gelatt, J. Kubler and Jr. Kubler  
*JMMM* **31**,88 (1983)
- [13] F. Ono *J.Phys.Soc.Jpn.* **50**,7 (1981)
- [14] O. Yamada *Physica B* **11**,90 (1983)
- [15] K. Tajima, P. Boni, G. Shirane, Y. Ishikawa and M. Khogi *Phys.Rev.B*  
**35**,1 (1987)
- [16] M. Matsunaga, Y. Ishikawa and T. Nakajima *J.Phys.Soc.Jpn.* **51**,1152  
(1982)
- [17] Y. Ishikawa, S. Onodera and K. Tajima *JMMM* **10**,183 (1979)
- [18] S. Onodera, Y. Ishikawa and K. Tajima *J.Phys.Soc.Jpn.* **50**,1513 (1981)
- [19] Y. Ishikawa, Y. Noda, K.R.A. Ziebeck and D. Givord *Solid State Comm.*  
**57**,531 (1986)
- [20] Y. Ishikawa, S. Onodera, B.H. Grier and G. Shirane *Solid State Comm.*  
**57**,535 (1986)
- [21] Y. Ishikawa, S. Onodera and K. Tajima *Solid State Comm.* **38**,561 (1981)
- [22] H.Akai and P.H. Dederichs *Phys.Rev.B* **47**,8739 (1993)
- [23] S. Khemelevskiy and P. Mohn *Phys.Rev.B* **66**,220404(R) (2002)
- [24] V. Crisan, P. Entel, H. Ebert, H. Akai, D.D. Johnson and J.B. Staunton  
*Phys.Rev.B* **66**,014416 (2002)

- [25] J.W. Taylor et al. *Phys.Rev.B* **65**,224408 (2002)
- [26] S.Khmelevskiy, I.Turek and P.Mohn *Phys.Rev.Lett.* **91**,037201-1 (2003)
- [27] F.Liot and C.A. Hooley *Cond-Mat.mtrl-sci arXiv*:**1208**,2850v
- [28] N Cowlam and A. Wildes *J.Condens.Matter* **15**,521 (2003)
- [29] M. Hatherly et al. *Proc.Phys.Soc.* **84**,55 (1964)
- [30] M.V. Schilfgaarde, I. Abrikosov and Johansson *Nature* **400**,46 (1999)
- [31] A.Z. Menschikov *JMMM* **10**,205 (1979)
- [32] A.Z. Menschikov and J.Schweiezer *Solid State Comm.* **100**,251 (1996)
- [33] [http://www.isis.stfc.ac.uk/instruments/emu/technical/  
emu-technical4935.html](http://www.isis.stfc.ac.uk/instruments/emu/technical/emu-technical4935.html)
- [34] [http://www.isis.stfc.ac.uk/instruments/hifi/technical/  
hifi-technical-information2994.html](http://www.isis.stfc.ac.uk/instruments/hifi/technical/hifi-technical-information2994.html)
- [35] [http://www.ill.eu/instruments-support/instruments-groups/  
instruments/in11/characteristics/](http://www.ill.eu/instruments-support/instruments-groups/instruments/in11/characteristics/)

# Chapter 5

## Spin-waves in $\text{Na}_x\text{CoO}_2$

### 5.1 Introduction to $\text{Na}_x\text{CoO}_2$

$\text{Na}_x\text{CoO}_2$  is a layered transition metal oxide which is composed of layers of  $\text{CoO}_2$  spaced with layers of sodium as shown in figure 5.1. It presents a hexagonal structure of space group  $P6_3/mmc$  where the cobalt occupies the Wyckoff position  $2a$  and the oxygen the position  $4f$  (see table 5.1). The cobalt ions form a two-dimensional triangular lattice within the  $ab$  plane and are surrounded by octahedra of oxygen ions [1]

The system is metallic over the entire range of sodium concentration and this behaviour is achieved by doping the Mott-insulating  $\text{CoO}_2$  layers with electron donated by the sodium atoms. The exception is at  $x=0.5$  where the system is a charge ordered insulator [2, 3].

Each cobalt has average charge  $\text{Co}^{4-x}$ , and in the ionic picture this corresponds to  $x$  non-magnetic  $\text{Co}^{3+}$  ions (with  $S=0$ ) in a background of  $\text{Co}^{4+}$  ions carrying spin  $S=1/2$ . The sodium ions may occupy two different sites

in the space between the  $\text{CoO}_2$  layers, the  $2b$  and  $2d$  sites. They form two inter-penetrating triangular lattices as shown figure 5.2 a) and are denoted by Na1 and Na2 respectively. The occupation of the Na1 site results in extra energy cost because of the short-range repulsion of the cobalt ion which lies above and below it. The spontaneous formation of multi-vacancy clusters drives the organization of  $\text{Na}^+$  ions as shown in figure 5.2 b). When the distance between two vacancies is reduced enough on the scale of the hexagonal lattice parameter,  $a$ , the promotion of a Na2 sodium to the central Na1 site is energetically favoured. In figure 5.2 c) we show the formation of tri-vacancy clusters and in figure 5.2 d) the ordered superstructure phases: the stripe and square phases observed by Morris et al. for a range of doping  $x > 0.75$  [7, 8]. This range of doping is particularly interesting because the  $\text{Na}_x\text{CoO}_2$  becomes magnetically ordered (see figure 5.1 c) ) and it will be discussed in more detail in the following paragraphs.

The study of the magnetic interactions, in fact, may provide useful information to explain the properties of  $\text{Na}_x\text{CoO}_2$ . In the range of doping  $0.5 < x < 0.9$  this exhibits large thermopower coupled with low resistivity which make it a promising candidate for technological applications [6].

In particular Wang et al. [9] have observed that a magnetic field strongly influences the thermopower and proposed that large spin entropy, associated with the conduction electrons, causes cooling when an electric current flows under an applied voltage. Furthermore recent investigations have shown that  $\text{Na}_x\text{CoO}_2$  becomes a superconductor at 5 K if hydrated ( $\text{Na}_x\text{CoO}_2 \cdot y\text{H}_2\text{O}$  with  $x \approx 0.3$  and  $y \approx 1.3$ ) [4]. The layered structure and the existence of superconduc-

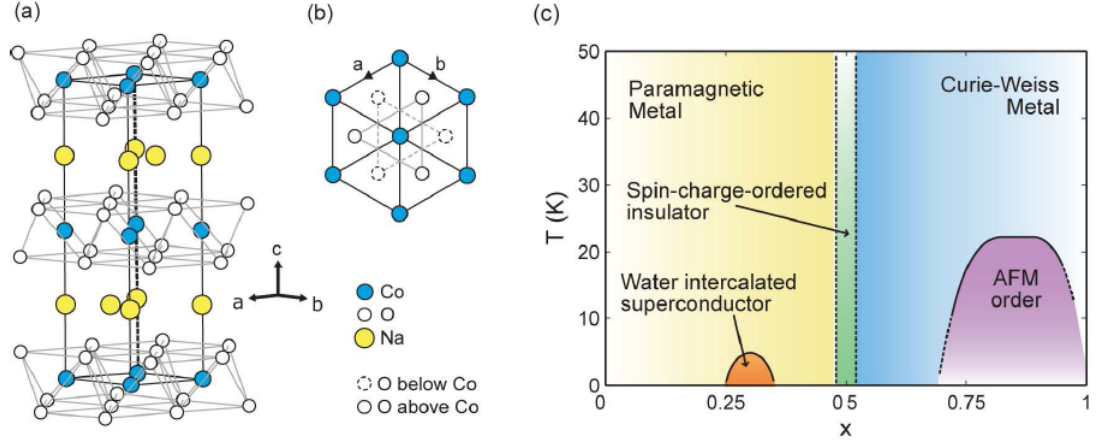


Figure 5.1: a) Crystal structure of  $\text{Na}_x\text{CoO}_2$ :  $\text{CoO}_2$  layer with intercalated Na. b) The hexagonal lattice of Co in the  $ab$  plane. c) The phase diagram of  $\text{Na}_x\text{CoO}_2$  [2, 5]

| Atom | Site | x             | y             | z             |
|------|------|---------------|---------------|---------------|
| Co   | 2a   | 0             | 0             | 0             |
| O    | 4f   | $\frac{1}{3}$ | $\frac{2}{3}$ | 0.0909(1)     |
| Na   | 2b   | 0             | 0             | $\frac{1}{4}$ |
| Na   | 2d   | $\frac{1}{3}$ | $\frac{2}{3}$ | $\frac{1}{4}$ |

Table 5.1: Atomic parameters of  $\text{Na}_{0.77}\text{CoO}_2$ . Space group:  $P6_3/mmc$ .  $a=2.84126(6)$  Å,  $c=10.8144(3)$  Å. [1]

tivity over a narrow range of doping near a Mott-insulator invite comparisons with the copper-oxide superconductors. Nonetheless there is experimental evidence which suggests that the superconductivity originates from an unconventional mechanism with respect to the cuprates [10, 11]. The importance of the spin degrees of freedom, both to explain the large thermoelectric effect and to clarify the origin of the superconductivity, provides a strong incentive to characterize the magnetic order and excitations of  $\text{Na}_x\text{CoO}_2$ . In this chapter we treat the case  $x=0.77$  which is in the interval of doping where the sodium cobaltate exhibits magnetic order. It is interesting to note that, even if the system becomes a superconductor for a quite different level of doping  $x\sim 0.3$ ,

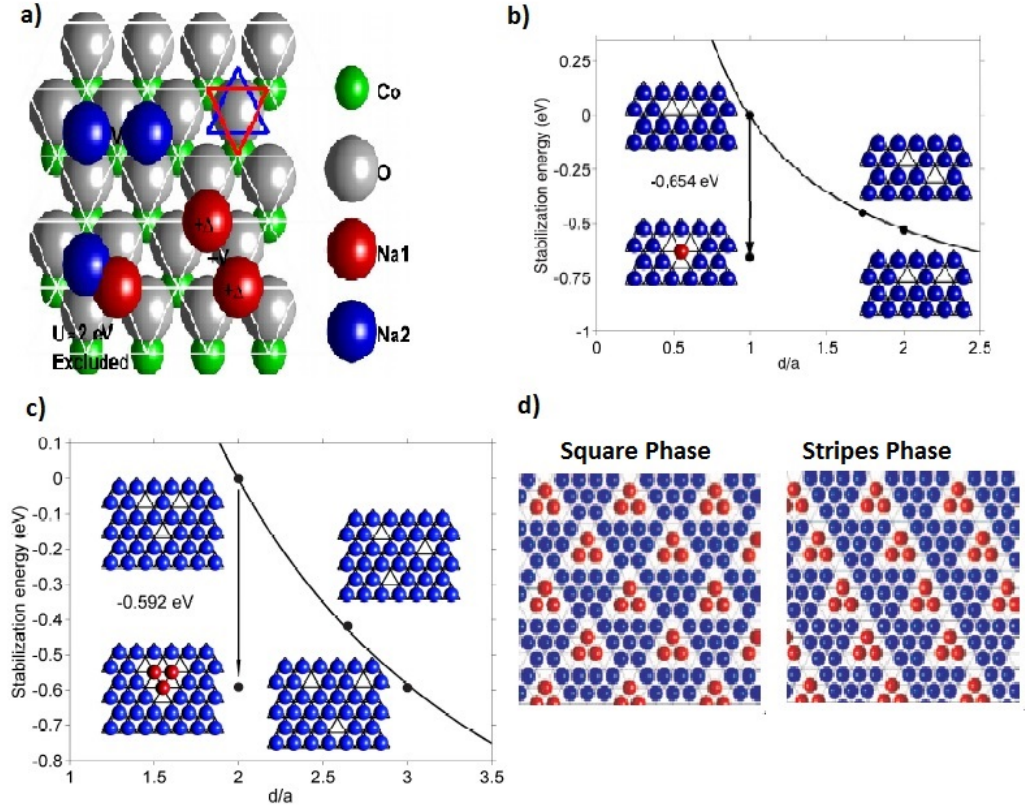


Figure 5.2: a) The two interpenetrating hexagonal lattices of intercalation sites  $2b$  and  $2d$  of the space group:  $P6_3/mmc$  occupied by the sodium ions and denoted by Na1 and Na2, respectively. The energy of 2 eV can be considered infinite at room temperature and, therefore, the occupation of neighbouring Na1 and Na2 sites is excluded. b) Energy for two vacancies decreases with increasing distance  $d$ , in the units of hexagonal lattice parameter  $a$ , as expected for Coulomb repulsion. Neighbouring vacancies can reduce their energy by promotion of a Na2 sodium to the central Na1 site. c) The tri-vacancy cluster which becomes favoured energetically when the distance between the vacancies is reduced d) ordered tri-vacancy phases: the square and the stripe phase observed for  $x > 0.75$ . [7, 8]



there is experimental evidence to suggest that the Co valence in the hydrated superconductor corresponds to  $x=0.6-0.75$  due to the presence of  $\text{H}_3\text{O}^+$  ions [12]. Therefore the magnetic phase studied here may represent a parent of the superconducting phase. This provides an additional incentive in studying the magnetic interaction in this phase because they may play a central role in the formation of the superconducting state.

Susceptibility measurements in the range of  $x\sim 0.7-0.95$  shows the presence of a magnetic transition at  $T_m \simeq 22$  K [13, 14]. This is confirmed by muon spin rotation ( $\mu\text{SR}$ ) measurement which suggested the existence of static magnetic order and places an upper limit of  $0.2\mu_B$  on the size of the ordered moment [15]. For  $T > T_m$  susceptibility is well fitted by a Curie-Weiss law plus a constant term indicating a degree of local character to the magnetism [14]. These fits give a negative Weiss temperature which implies that antiferromagnetic correlations are dominant. Further ( $\mu\text{SR}$ ) measurements indicated that in the magnetically ordered phase, moments are aligned along the c-axis [16].

However the ground state magnetic structure of sodium cobaltate has been unambiguously determined by polarized neutron scattering measurements performed by Bayrakci et al. [17] on a sample of  $\text{Na}_{0.82}\text{CoO}_2$ . They observed magnetic Bragg reflections at a few  $(h,k,l)$  with  $h$  or  $k \neq 0$  and  $l$  odd, and an absence of magnetic reflections with  $l$  even. Figure 5.3 a) shows the temperature dependence of the  $(1,0,1)$  and  $(1,0,0)$  peaks. These results are consistent with A-type antiferromagnetic order with the magnetic moments pointing along the c-axis (see figure 5.3 b)). Such a magnetic arrangement is characterized by ferromagnetic (FM) spin coupling within the ab plane and antiferromagnetic

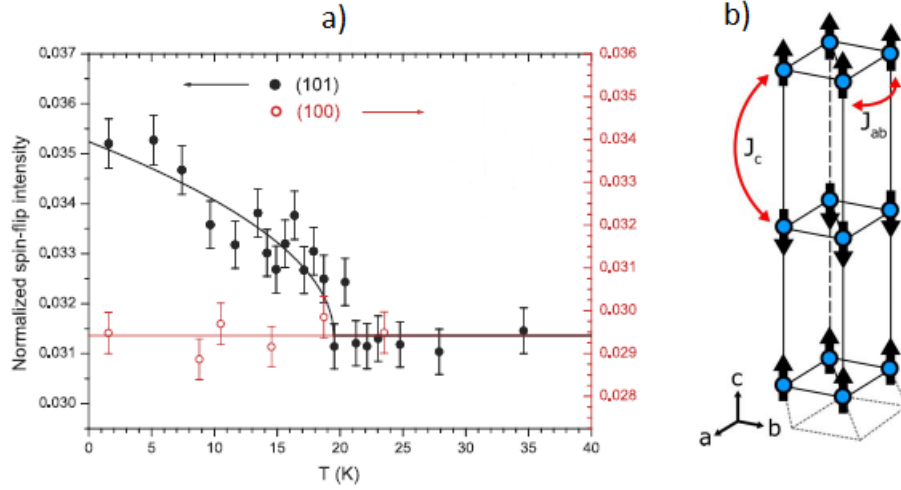


Figure 5.3: a) *Spin flip (SF) intensity at  $\mathbf{Q}=(1,0,1)$  and  $(1,0,0)$ , as a function of temperature (the lines are guides for the eye). The absence of the Bragg magnetic reflection  $(1,0,0)$  together with the presence of the magnetic reflection  $(1,0,1)$  indicates that the magnetic propagation vector is  $(0,0,1)$  consistent with the A-type antiferromagnetic (AF) structure (shown in b)) with Co spins parallel to the  $c$ -axis[17]. b) The magnetic unit cell, showing the exchange interactions used to model the dispersion in figure 5.4*

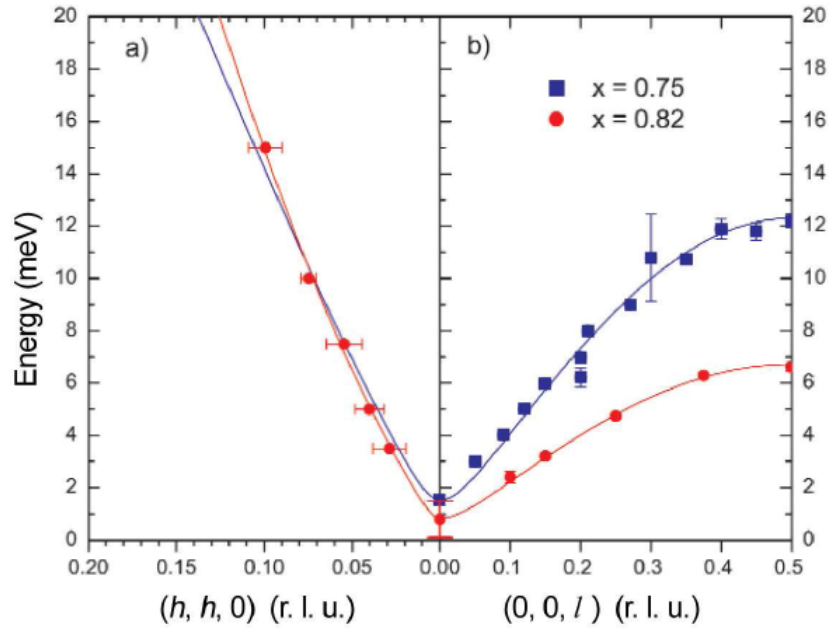


Figure 5.4: *Spin wave dispersion along  $(h,h,0)$  and  $(0,0,l)$  for  $x=0.82$  (red) [17] and  $x=0.75$  (blue) [19]. The solid lines are obtained by fitting the data using the Hamiltonians described in the text.*

(AF) spin coupling along the c-axis.

The same group also performed inelastic unpolarized neutron scattering measurements in order to describe the spin wave excitations in  $\text{Na}_{0.82}\text{CoO}_2$  and to determine the in-plane and out of plane magnetic interactions. They characterized the spin wave dispersion along high symmetry directions, in particular the in-plane  $(h,h,0)$  direction and the out-plane direction  $(00l)$ . These dispersions are illustrated in figure 5.4, the solid line results from fits to the data points assuming a simple Heisenberg spin Hamiltonian given by:

$$\hat{\mathcal{H}} = J_{ab} \sum_{i,i'} \hat{S}_i \cdot \hat{S}_{i'} + J_c \sum_{i,j} \hat{S}_i \cdot \hat{S}_j - D \sum_i (\hat{S}_i^z)^2 \quad (5.1)$$

where  $J_{ab}$  and  $J_c$  are the coupling constants characterizing the exchange interactions within the ab plane and between adjacent planes, respectively, see 5.3 b). Only nearest-neighbour interactions are considered, and  $i,i'$  and  $i,j$  denotes spin pairs within the same layer and on adjacent layers respectively.  $D$  is the single-ion anisotropy; it quantifies the tendency of the spins to align along the c-axis and it generates the gap observed in the spin wave dispersions (see figure 5.4). The values for the coupling constants  $J_{ab}$  and  $J_c$  and the anisotropy obtained from the fits of Bayrakci et al. are listed in table 5.1.  $J_{ab}$  and  $J_c$  values are comparable and this reveals that the magnetic correlations in  $\text{Na}_{0.82}\text{CoO}_2$  are of a three-dimensional nature, which is surprising in the light of the two dimensionality of the system.

Similar conclusions have been reached by Helme et al. [18] for a sample of  $\text{Na}_{0.75}\text{CoO}_2$ . They observed spin wave dispersions along the same directions

|                                | $J_{ab}$ (meV) | $J_c$ (meV) | D (meV) | E (meV) |
|--------------------------------|----------------|-------------|---------|---------|
| $\text{Na}_{0.82}\text{CoO}_2$ | -9.0           | 6.6         | 0.05    | —       |
| $\text{Na}_{0.75}\text{CoO}_2$ | -6.0           | 12.2        | 0.096   | 0.059   |

Table 5.2: *Values of the coupling constants (see 5.3 b)) obtained in different work.  $\text{Na}_{0.82}\text{CoO}_2$  from Bayrakci et al. [17] and  $\text{Na}_{0.75}\text{CoO}_2$  of Helme et al. [18, 19]*

similar to those of Bayrakci et al. Nevertheless the values of the coupling constants resulted from analogous fits, are different with the respect to those of Bayrakci et al. especially  $J_c$  (see table 5.1). This means that the sodium doping has an important influence on the magnetic interactions. Also Helme et al. observed the same gap.

In order to investigate the nature of the gap they performed further inelastic neutron scattering measurements on  $\text{Na}_{0.75}\text{CoO}_2$  using cold neutrons [19]. At fixed  $\mathbf{Q}=(001)$  scans of energy transfer were better fitted by two Gaussian peaks instead of one. Thus Helme et al. concluded that this gap is double rather than single [19]. This double gap disappears as temperature reaches  $T_m$ . Figure 5.5 shows the peak fitting while figure 5.6 displays the resulting dispersion. In order to fit the dispersion they suggested a model Hamiltonian in which there is also an in-plane anisotropy E:

$$\hat{\mathcal{H}} = \hat{\mathcal{H}}_B - E \sum_i [(\hat{S}_i^x)^2 - (\hat{S}_j^y)^2] \quad (5.2)$$

$\mathcal{H}_B$  is the Heisenberg Hamiltonian in equation 5.1 suggested by Bayrakci et al. [17], and the second term is an in-plane anisotropy consistent with the  $\text{Na}_{0.75}\text{CoO}_2$  symmetry. The results of the fit are listed in table 5.1. The same

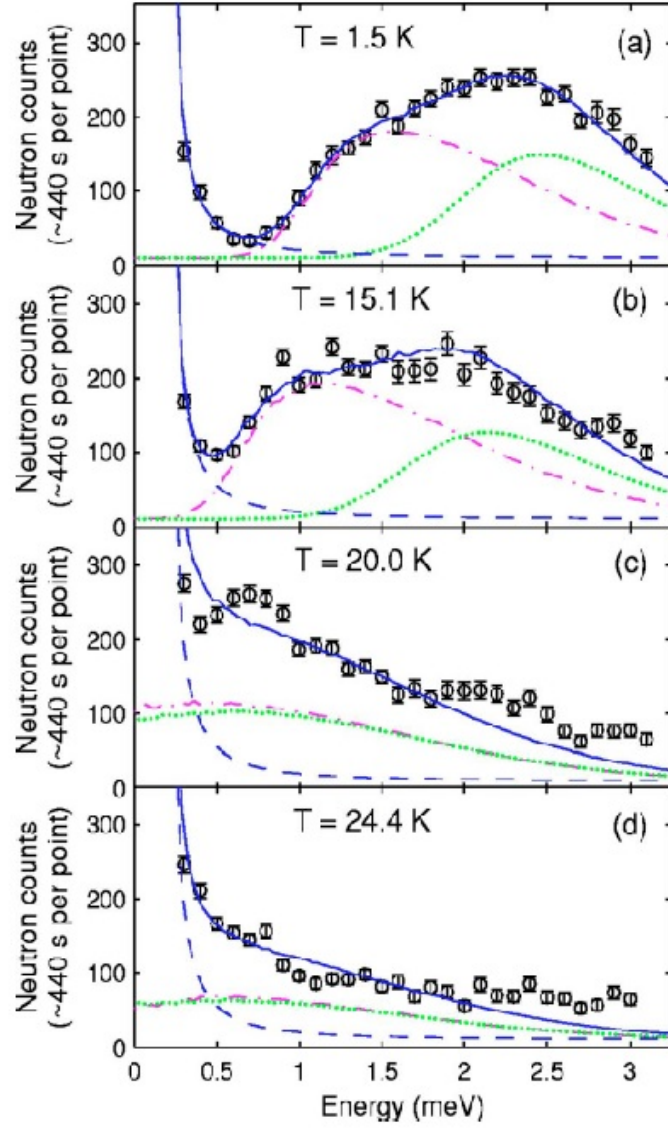


Figure 5.5: (a)-(j) Energy scans at  $Q=(0,0,1)$  at temperatures between 1.5 K and 24.4 K. Solid curves represent the best fit obtained considering two Gaussian peaks (green and purple lines) plus an incoherent peak (dashed line).[19]

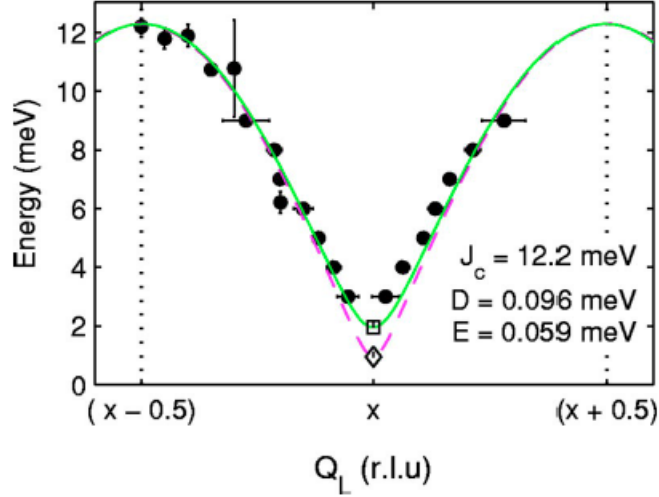


Figure 5.6: *Magnon dispersion parallel to  $(0,0,l)$  centred at  $(0,0,x)=(0,0,3)$  measured at IN20 [18]. Open square/diamond: fits to 1.5 K energy scan at  $(0,0,x)=(0,0,1)$  measured at IN14. Solid and dashed lines curves are obtained fitting the dispersions using the Hamiltonian 5.1 [19].*

group observed a spin-flop transition of the A-type AF structure induced by an applied magnetic field along the crystallographic axis  $c$ . They showed that the spin-flop field is consistent with the size of this double anisotropy gap.

In order to clarify the nature of the gap in the spin wave excitations and the change of magnetic interactions as a function of doping  $x$ , we performed polarized inelastic neutron scattering measurements on a sample of  $\text{Na}_{0.77}\text{CoO}_2$ . The doping has an important influence on the exchange coupling parameters as shown by the different results of Helme et al. and Bayrackci et al. [17, 18, 19].

In our studies we have tried to quantify these effects by comparing our results with those shown above. Furthermore in our data analysis we have tried to include the effects of the crystal field acting on the magnetic ions. The crystal field (CF), in fact, is expected to create the magnetic anisotropies which are responsible for the particular ground state magnetic structure of the

system and that eventually justifies the presence of a gap in the spin-wave excitations as shown in the presented works.

Therefore, in the first instance, we assumed a model Hamiltonian different from those presented above. The anisotropy terms are replaced by a more detailed single-ion Hamiltonian which includes the CF effects. The ground state magnetic structure is given by the minimum of this Hamiltonian, and this is achieved performing a self-consistent mean-field Monte Carlo simulation. After obtaining the magnetic structure observed by Bayrakci et al. [17], it is possible to calculate the spin-wave dispersions and compare them with inelastic neutron scattering data. The spin-wave dispersions were calculated using a dynamical matrix diagonalization (DMD) algorithm. For the Monte Carlo simulations and the DMD calculations we used the software McPhase which provides both of these program packages [14].

In the next section we present the attempt to obtain the ground state magnetic structure of  $\text{Na}_{0.77}\text{CoO}_2$  including the CF effects which have been estimated using the point-charge approximation [16]. As a result we obtain qualitative agreement between the calculated and the experimentally observed single-ion electronic configuration. On the other hand, this approximation fails to obtain a stable magnetic structure for the system. Thus we went back to the much simpler model suggested in the literature. Furthermore we considered also the action of inter-layer second neighbour in the Heisenberg Hamiltonian in accordance with the density functional theory calculations of Johannes et al. [24]. Under these assumptions, we have good agreement between the calculated spin-wave dispersion and the measured one if furthermore we adopt

an anisotropic inter-layer exchange coupling tensor  $J_c=(J_a, J_a, J_c)$  instead of an isotropic one suggested in the literature [17, 18, 19]. These results are shown in section 4.3.

## 5.2 McPhase Calculation on $\text{Na}_x\text{CoO}_2$

As shown in the paragraph 3.3.1, to describe a quantum system we may use the Hamiltonian 3.5 which is composed of a term which represents the Hamiltonian of a single subsystem  $n$ , and a term describing the interaction between different subsystems. In the case of the magnetic sodium cobaltate,  $\text{Na}_x\text{CoO}_2$  there is only one subsystem represented by the cobalt magnetic active ions. The  $\hat{I}_\alpha^n$  operators correspond to the spin components,  $\hat{S}_\alpha^n$  of the ion,  $n$ . Hence, the Hamiltonian 3.5 becomes:

$$\hat{\mathcal{H}} = \sum_{n=1}^N \hat{\mathcal{H}}_{Co}^n - \frac{1}{2} \sum_{n,n'\alpha\beta} J_{\alpha\beta}(i,j) \hat{S}_\alpha^n \hat{S}_\beta^{n'} \quad (5.3)$$

where  $\alpha, \beta = 1 - 3$ . The first term describes the electronic configuration of the cobalt ion placed in its crystal environment, while the second term of the Hamiltonian represents the exchange interaction between the spins of different ions. This second term may be replaced by the simple Heisenberg Hamiltonian described in the introduction, which considers just the intra-plane and inter-plane nearest neighbours. In addition we consider also the inter-layer next neighbours coupling as suggest by the DFT calculation of Johannes et al. [24]. In this way the large amplitude of the dispersion along the direction (0,0,1) can



be explained in a way more consistent with the 2-dimensional symmetry of the system instead of considering a 3-dimensional magnetic behaviour suggested in the literature [17, 18].

The first term of the Hamiltonian 5.3 as shown in section 3.2.2 is the sum of four contributions: the electron-electron Coulomb interaction,  $\hat{\mathcal{H}}_{e-e}$ , the spin-orbit interaction,  $\hat{\mathcal{H}}_{so}$ , the crystal field interaction,  $\hat{\mathcal{H}}_{CF}$  and the Zeeman interaction,  $\hat{\mathcal{H}}_Z$  if an external magnetic field is applied.

The crystal field in  $\text{Na}_x\text{CoO}_2$  is expected to play an important role in determining the energy states of the cobalt ions. In fact, the  $\text{Co}^{4+}$  and the  $\text{Co}^{3+}$  as free ions are in the high spin configuration (HS) with  $S=5/2$  and  $S=2$ , respectively while in  $\text{Na}_x\text{CoO}_2$  they are in the low spin (LS) configuration  $S=1/2$  and  $S=0$ , respectively. The crystal field acting on cobalt ions, is due to the surrounding oxygen situated at the vertices of distorted octahedra. Similar configurations are also present in the case of the  $\text{MnV}_2\text{O}_4$  as shown in the next chapter. The cubic symmetry lifts the degeneracy of the 3d orbitals of the central ion splitting them into lower lying  $t_{2g}$  ( $d_{xy}$ ,  $d_{xz}$ ,  $d_{yz}$ ) and higher lying  $e_g$  ( $d_{z^2}$ ,  $d_{y^2-x^2}$ ) orbitals. Figure 5.7 shows the distorted  $\text{CoO}_6$  octahedra which result from the  $\text{CoO}_2$  layers stacking along the crystallographic c-axis. They are elongated along their (0,0,1) direction and moreover they are distorted in such a way that the resulting symmetry is trigonal. In particular their (1,1,1) direction is a trigonal axis which is oriented along the c-axis of the system. The presence of the elongation along (0,0,1) and the trigonal distortion are expected to lift furthermore the degeneracy of the  $t_{2g}$  in  $e_g^\pi$  and  $a_{1g}$  symmetry

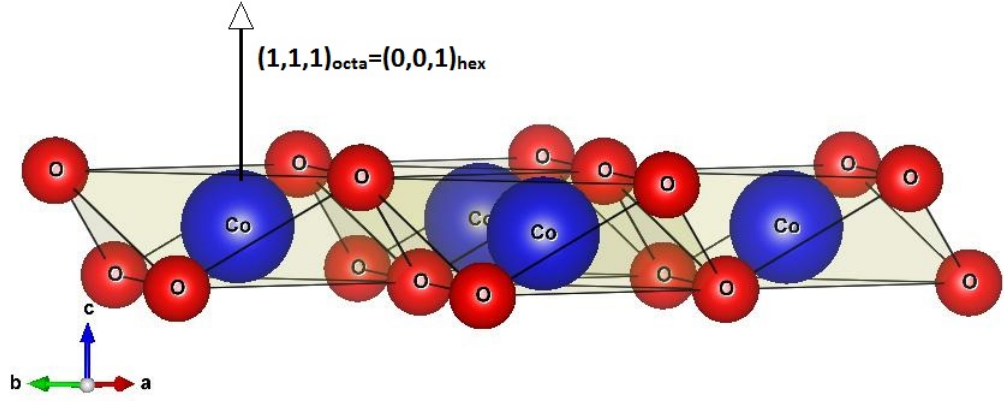


Figure 5.7: The  $\text{CoO}_6$  octahedra of  $\text{Na}_x\text{CoO}_2$ . They are elongated along their  $(0,0,1)$  direction and trigonally distorted. The direction  $(1,1,1)$  of the octahedra is a trigonal axis and it is directed along the crystallographic axis  $c$ .

which may be represented as

$$a_{1g} = \frac{1}{\sqrt{3}}(d_{xy} + d_{xz} + d_{yz}); e_{\pm g}^{\pi} = \frac{1}{\sqrt{3}}(d_{xy} + e^{\pm i2\pi/3}d_{xz} + e^{\pm i4\pi/3}d_{yz}) \quad (5.4)$$

We calculated the crystal field effect using the point charge approximation. In this approach only the electrostatic interactions between the central ion and its surroundings are considered, while covalency effects, spatial distribution of charges and ligand bond strengths are neglected. Therefore in the case of the conducting  $\text{Na}_x\text{CoO}_2$  this approximation is expected to underestimate the splitting of the single-ion energy levels.

The position of the oxygen ions relative to the central cobalt ions have been calculated using the space group parameters obtained from previous neutron diffraction results which are available in the literature [1] and are listed in table 5.1.

The sodium ions have not been considered in the point charge calculations

| Llm parameters | Values (meV) |
|----------------|--------------|
| L20            | -651.34(3)   |
| L40            | -272.85(8)   |
| L43            | 421.77(2)    |

Table 5.3: *Crystal field parameters in Llm Wybourne notation calculated in point-charge approximation.*

because their distances with respect to the cobalt ions are much bigger than those of oxygen ions and their nominal charge twice smaller in absolute value.

The results of these calculations are listed in table 5.3.

The presence of only these three parameters is in agreement with the trigonal symmetry of the system. The calculation of the single energy levels of  $\text{Co}^{3+}$  and  $\text{Co}^{4+}$  ions have been performed in the strong crystal field limit using the module **ic1ion** of the software McPhase, described in paragraph 3.2.2. In these conditions, the crystal field (CF) interaction operators,  $\hat{\mathcal{H}}_{CF}$ , are considered to act as first on single-electron states then electron-electron (Coulomb),  $\mathcal{H}_{e-e}$ , and spin-orbit interactions,  $\mathcal{H}_{SO}$  treated as a perturbation on the CF levels obtained.

The ground state of the  $\text{Co}^{4+}$  ion is characterized by spin  $S=1/2$  and orbital moment  $L=1$ . The first excited state is a doublet at an energy 129 meV higher and it is characterized by a spin  $S=1/2$  and orbital moment  $L=0$ . The ground state of  $\text{Co}^{3+}$  instead resulted to be a singlet characterized by spin  $S=0$  and orbital moment  $L=0$ , while the first excited state resulted at an energy of 1.3 eV higher. This is consistent with the idea of a distribution of  $\text{Co}^{3+}$  and  $\text{Co}^{4+}$  ions where the former are magnetically inactive. The calculation of the ground state magnetic structure has been performed considering only

nearest neighbour spin pair coupling as suggested in the works reported in the introduction and this means that the magnetically inactive  $\text{Co}^{3+}$  ions are omitted. As a first estimate of the exchange coupling parameters we used the values obtained in the literature. The values of the exchange coupling parameters can be refined by fitting the measured spin wave dispersions we will present in the next paragraphs.

Unfortunately the mean field Monte Carlo calculations assuming the Hamiltonian 5.3, failed and no stable magnetic structure has been obtained at the end of the process. Many reasons could have caused this failure. Firstly the point charge method is probably too approximate because it neglects important effects of covalency and of charge spatial distribution that in a conducting system like  $\text{Na}_x\text{CoO}_2$  are very important.

In the second instance the exclusion of the sodium ions in the calculation of the cobalt ions ground state may have influenced the result. In fact, the system becomes magnetically ordered only for a doping level  $x \geq 0.7$ . Recent studies on  $\text{Na}_x\text{CoO}_2$  have shown that the particular sodium ion patterning has a decisive role in the transport and magnetic properties [7]. We considered instead a system with only magnetically active  $\text{Co}^{4+}$  ions as the un-doped compound which does not show magnetic ordering.

In order to obtain the stable magnetic structure observed experimentally, we went back to the simple models suggested in the literature [17, 19] where the  $\text{Na}_x\text{CoO}_2$  is treated as a simple spin  $S=1/2$  interacting system. To do that we used the module **solion** described in paragraph 3.2.1, to define a simple spin  $1/2$  ion.

The A-type antiferromagnetic structure with the cobalt spins aligned along the c-axis which is shown in figure 3 b), is obtained with  $D_z^{Co} > 0$  as shown in the literature.

### 5.3 Results and Discussion

The polarized inelastic neutron scattering has been performed on a single crystal of  $\text{Na}_{0.77}\text{CoO}_2$  which has been grown by Dr S. Uthayakumar using the floating zone technique at Royal Holloway University of London. The doping level has been estimated measuring the relative X-ray scattering intensity of the superstructure peaks due to ordered patterning of the sodium tri-vacancies between the  $\text{CoO}_2$  layers [7]. All measurements were performed using the thermal triple-axis spectrometer IN20 at the I.L.L. with the help of Mechthild Enderle.

We used curved Heusler (111) as both monochromator and analyzer because it is a good selector of polarization direction. We used a graphite filter placed in the scattered beam to suppress higher order harmonics. The crystal has been mounted in a standard helium cryostat and aligned using the reflections (110) and (002). Here the notation  $(hkl)$  refers to the hexagonal reciprocal lattice of the system characterized by an angle between the reciprocal vector  $\mathbf{a}^*$  and  $\mathbf{b}^*$  of  $60^\circ$ .

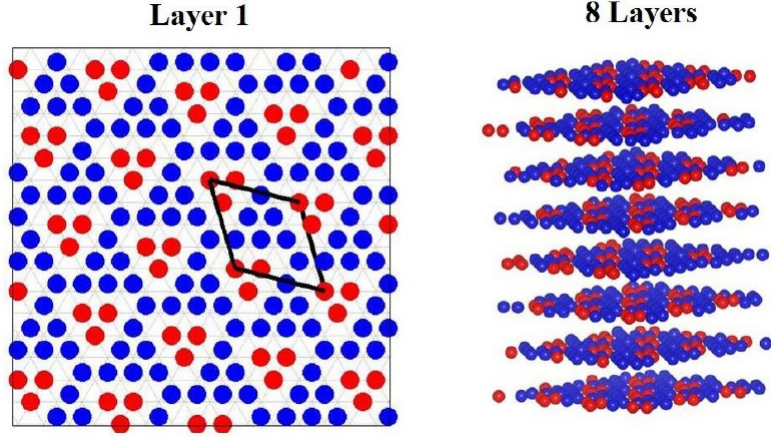


Figure 5.8: The  $1/13^{th}$  tri-vacancy phase structure observed by M. Pandiyan [25].

### 5.3.1 Tri-vacancy Phase Check

The tri-vacancy phase characteristic of the range of doping  $0.75 < x < 0.8$  may present three possible configurations which differ from each other by the different arrangements of the tri-vacancies in the space between the  $\text{CoO}_2$  layers: the stripe phase, the square phase [8] and the  $1/13^{th}$  phase [25]. This corresponds to three different arrangements of superstructure peaks in reciprocal space, in particular the observed superstructure peaks are well indexed using a commensurate hexagonal grid of periodicity  $\frac{a^*}{N}$ , where  $N$  is an integer. Figure 5.2 displays the *square* and *stripe* phases which have been observed by Morris et al. for  $x=0.75$ ,  $0.78$  and  $0.92$  using neutron and X-ray diffraction. The *square* phase is the ground state structure phase for these doping levels and it is stable up to  $\sim 280$  K. The superstructure peaks relative to this phase lie on a  $a^*/15$  grid. Furthermore Morris et al. for the concentration  $x=0.78$  (close to our  $0.77$ ) observed also the presence of a second low temperature *stripe* phase coexisting with the *square* phase and with superstructure peaks

lying on the same  $a^*/15$  grid [8].

More recent neutron and X-ray diffraction measurements performed by M. Pandiyan have shown a third possible phase of tri-vacancy order which is dominant for our particular case of doping level ( $x=0.77$ ) [25]. This third phase is characterized by an  $a^*/13$  periodicity so that it has been called  $1/13^{th}$  phase. This phase along with its corresponding cell are displayed in figure 5.3.1, this superstructure presents a rather complicated stacking sequence with a periodicity along the  $c$  axis of eight sodium layers.

In order to check the phase of our sample, we monitored the intensity of the superstructure peaks produced by the three different phases. The results of this check are shown in figures 5.9, 5.10 and 5.11. The absence of the  $(1/3, 2/3, 0)$ ,  $(0.2, 0.2, 0)$  and  $(0.4, 0.4, 0)$  reflections excluded the presence of the square phase, while the absence of the  $(0.6, 0.4, 0)$  reflection excludes the presence of the stripe phase of tri-vacancies. The high intensity peak observed at  $(1.077, 0.692, 0.25)$  in the  $Q_h$  and  $Q_k$  scans, instead is a clear sign of the presence of the single phase  $1/13_{th}$ .

### 5.3.2 Presentation of the Inelastic Data

All the inelastic neutron scattering measurements were made at a base temperature of 1.5 K by keeping fixed the final neutron wave vector  $k_f$  at  $2.662 \text{ \AA}^{-1}$ . The XYZ-polarization analysis technique described in chapter 2 has been used to separate the contribution of magnon excitations from phonons. We used a Gaussian distribution to fit the magnetic component of the neutron scattering which is given by an appropriate combination of the spin-flip (SF)

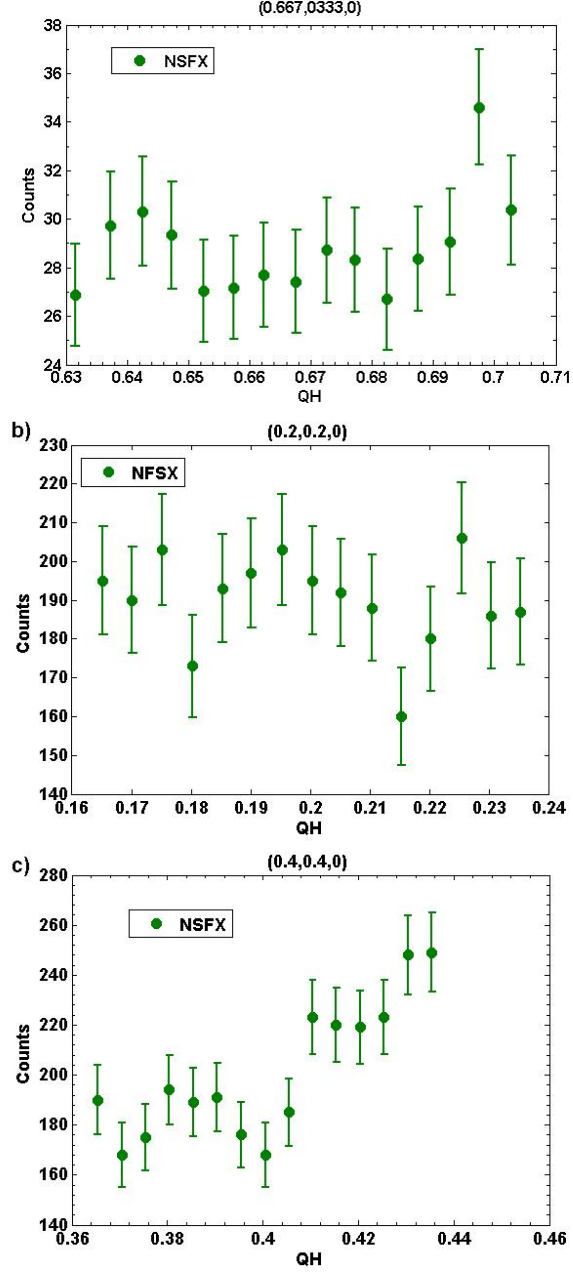


Figure 5.9: Absence of the reflection peaks at  $(0.667, 0.333, 0)$ ,  $(0.2, 0.2, 0)$  and  $(0.4, 0.4, 0)$ . The sample is not in the square phase.



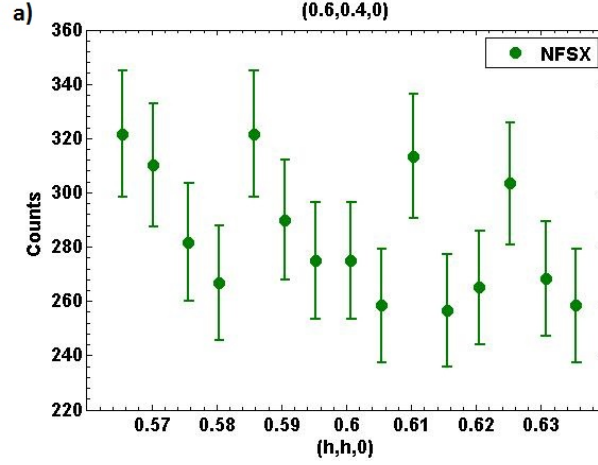


Figure 5.10: *Absence of the reflection peak at  $(0.6,0.4,0)$ . The sample is not in the stripe phase.*

channels  $|M_{\perp}| = 2SF_x - SF_y - SF_z$ .  $M_{\perp}$ , is the component of the magnetization which is perpendicular to the wave-vector transfer of the neutron. This should give a magnetic peak on zero background. Alternatively, if the non-spin-flip signal  $NSF_x$  was flat, we were able to use the sum of the three spin-flip channels, since they combine to give a larger magnetic peak on a flat background. Peak analysis is shown in the following figures, in particular we considered the high symmetry directions  $(h,h,3)$  and  $(0,0,l)$ . Figure 5.12 and 5.13 show the  $\mathbf{Q}$  scans along the direction  $(h,h,3)$  at a fixed energy of 5 meV and 7.5 meV. Part b) of these figures shows the magnetic component of the neutron scattering and multiple Gaussian fit on a near zero background.

In figure 5.14 a) and 5.15 a) are shown the  $\mathbf{Q}$  scans along the direction  $(0,0,l)$  at different fixed energy 4 and 5 meV, respectively. The NSF x component is much lower in intensity with respect to its SF counterpart and this indicates that this scattering is pure magnetic. The fits of SF component are shown in the b) part of the figures. The results of the fits of the  $\mathbf{Q}$  scans are summarized

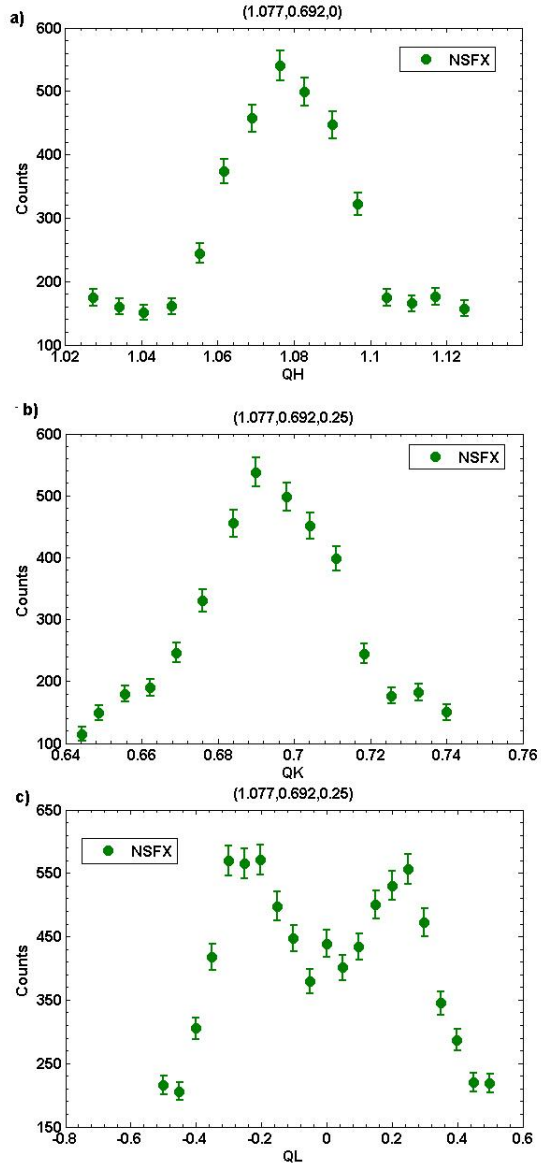


Figure 5.11: *Intense peak observed in both the  $\mathbf{h}$  and  $\mathbf{k}$  directions around  $(1.077, 0.692, 0)$ . A double peak is present at  $(1.077, 0.692, 0.25)$ . The sample is in the  $1/13^{\text{th}}$  single phase.*

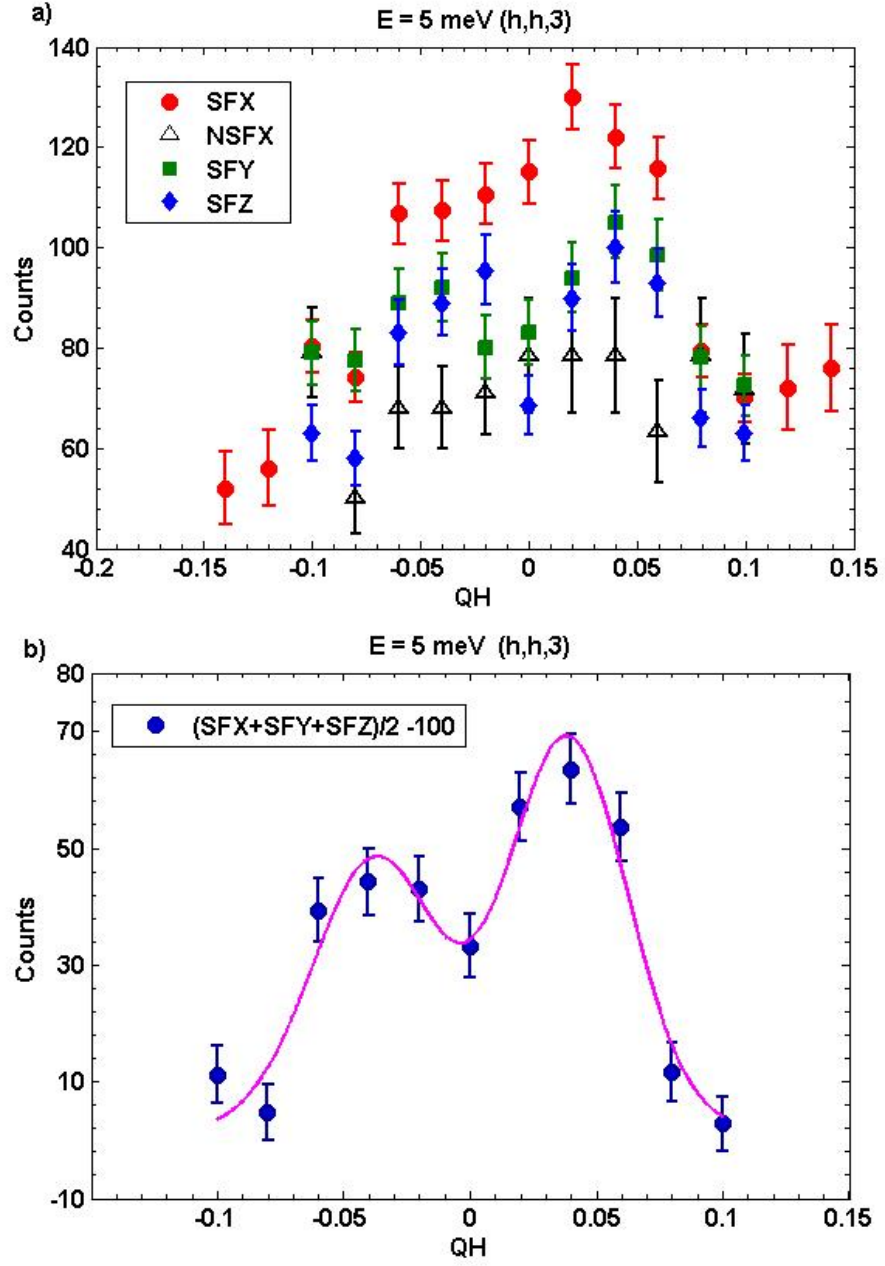


Figure 5.12: a)  $Q$  scan at fixed energy  $E=5$  meV along the direction  $(h,h,3)$ . Spin flip components along the polarization directions  $x$ ,  $y$  and  $z$ . Non spin flip component along  $x$ . b) The signal obtained by the linear combination shown in the picture and relative multiple Gaussian fit.  $\chi^2=2.665$

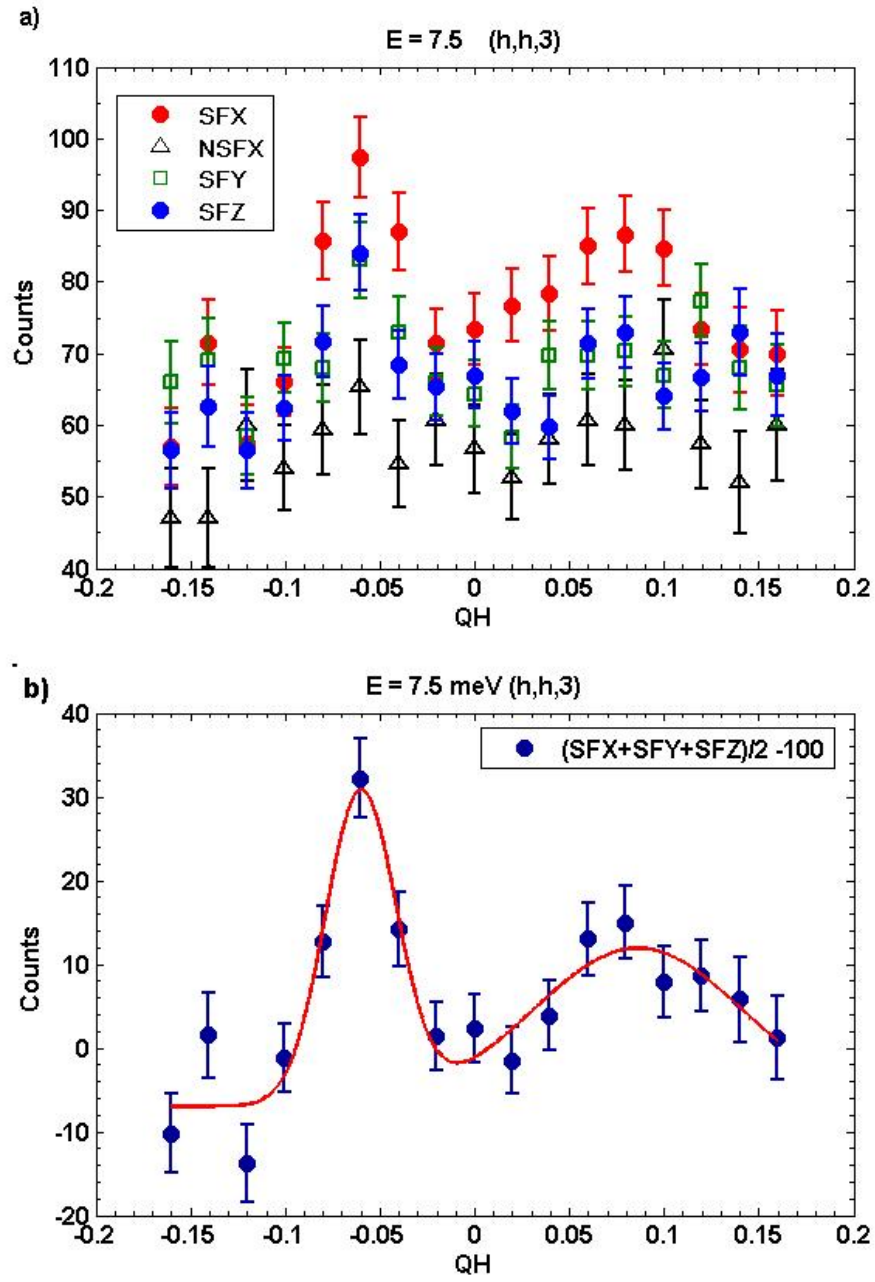


Figure 5.13: a)  $Q$  scan at fixed energy  $E=7.5$  meV along the direction  $(h, h, 3)$ . Spin flip components along the polarization directions  $x$ ,  $y$  and  $z$ . Non spin flip component along  $x$ . b) The signal obtained by the linear combination shown in the picture and relative multiple Gaussian fit.  $\chi^2=0.996$

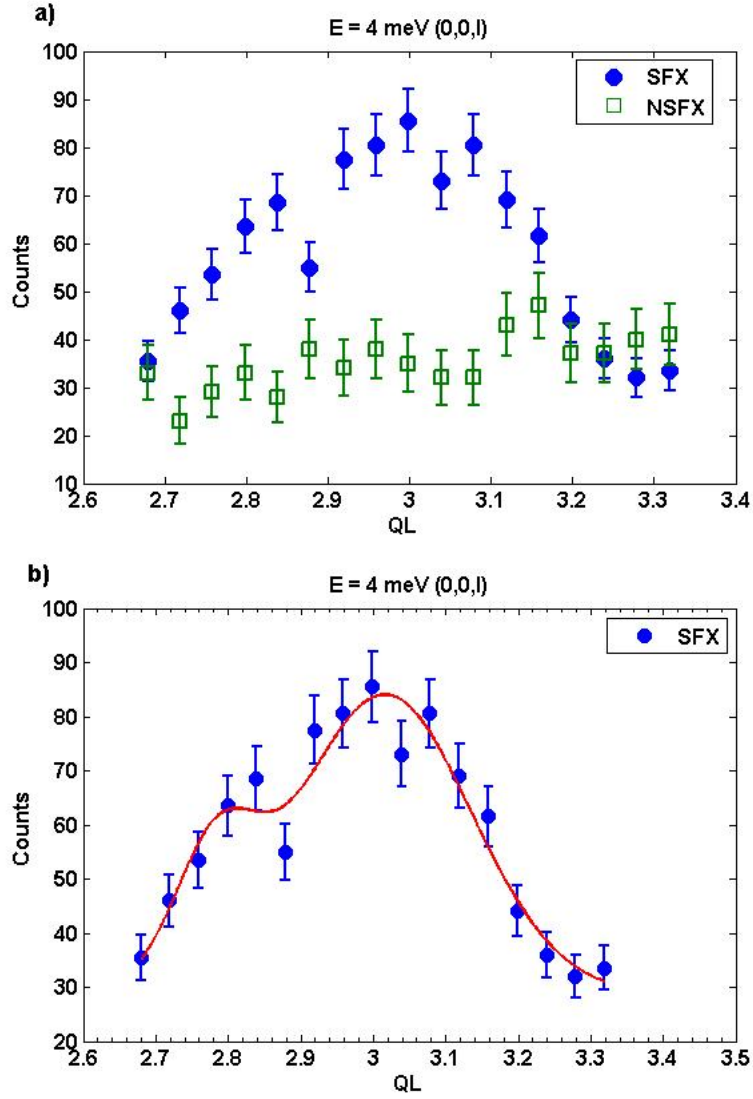


Figure 5.14: a)  $Q$  scan at fixed energy  $E=4$  meV along the direction  $(0,0,l)$ . Non Spin flip component is much lower than the SF one along the same polarization directions  $x$ . The scattering is pure magnetic b) Multiple Gaussian fit of the  $SF_x$  component.  $\chi^2=1.1087$

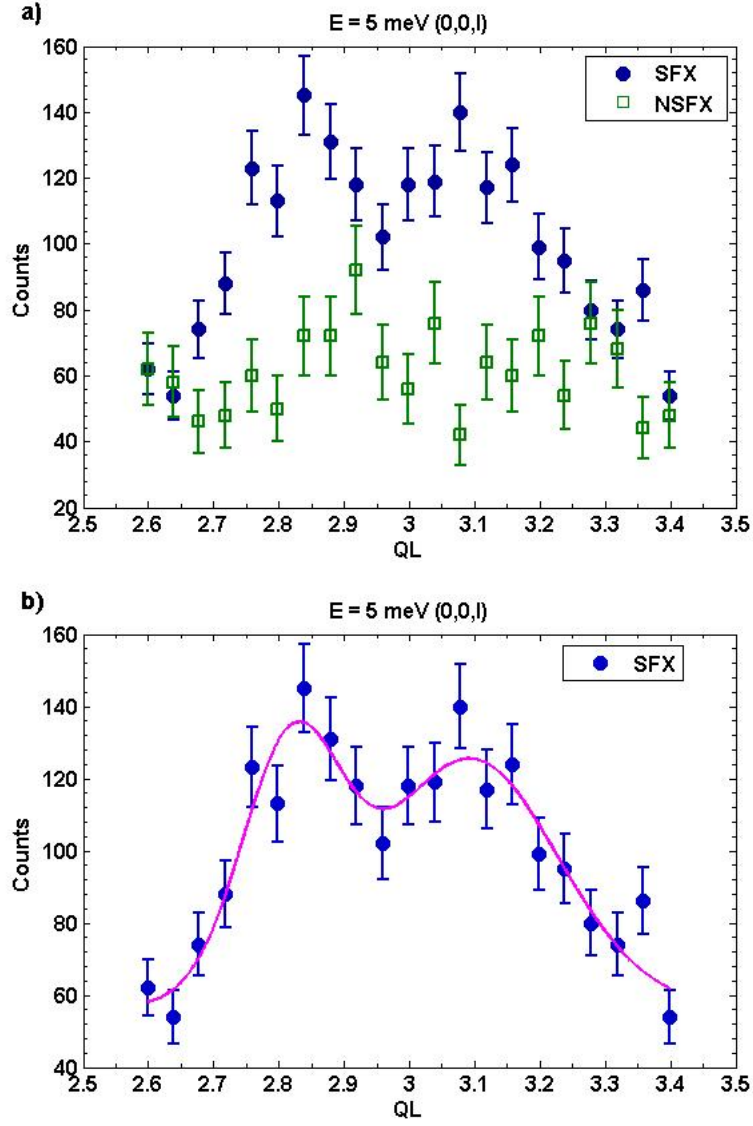


Figure 5.15: a)  $Q$  scan at fixed energy  $E=5$  meV along the direction  $(0,0,l)$ . Non Spin flip components is much lower than the SF one along the same polarization directions  $x$ . The scattering is pure magnetic b) Multiple Gaussian fit of the  $SF_x$  component.  $\chi^2=1.390$

| Energy (meV) | Direction   | $\ell/h$ ( $\text{\AA}^{-1}$ ) |
|--------------|-------------|--------------------------------|
| 4            | 00 $\ell$   | $2.780 \pm 0.021$              |
| 4            | $\parallel$ | $3.018 \pm 0.015$              |
| 5            | $\parallel$ | $2.820 \pm 0.021$              |
| 5            | $\parallel$ | $3.093 \pm 0.032$              |
| 5            | hh3         | $-0.0376 \pm 0.0067$           |
| 5            | $\parallel$ | $0.0386 \pm 0.0046$            |
| 7.5          | $\parallel$ | $-0.0612 \pm 0.0095$           |
| 7.5          | $\parallel$ | $0.0570 \pm 0.0130$            |

Table 5.4: *Fit results after the XYZ-polarization analysis of the fixed energy  $Q$  scans.*

in table 5.4.

In figure 5.16 we report an energy scan at fixed  $Q = (0.5, 0.5, 3) \text{\AA}^{-1}$  which corresponds to the zone boundary. Maybe there is a very low intensity peak centred at  $\sim 31$  meV as estimated by the fit ( $\chi^2 = 0.761$ ).

In figure 5.17 are shown the energy scans at zone boundary  $(0, 0, 2.5)$ . The intensity at this point is very low as shown by the poor counts in figure 5.17 a). Nevertheless the XYZ-polarization analysis allows us to observe a magnetic peak in zero background, see figure 5.17 b). This peak is easily fitted by a single Gaussian function providing us the value of the inter-layer coupling  $J_c$ . Finally, figure 5.18 shows the gap at  $(0, 0, 3)$  and the origin of it is magnetic as shown by the high intensity of the SF signal. The gap seems to be single rather than double as suggested in the literature. The fit gave us a value of  $1.91 \pm 0.12$  meV which is in good agreement with the higher energy mode observed by Helme et al at  $1.95 \pm 0.15$ . Also the width of our peak,  $0.85 \pm 0.16$ , is in good agreement with that one observed by Helme et al. [19]. Resolution corrections were considered using RESCAL. The results account for the weaker peak  $\sim 3.80$  meV in Fig. 4.18. Otherwise the corrections were negligible.

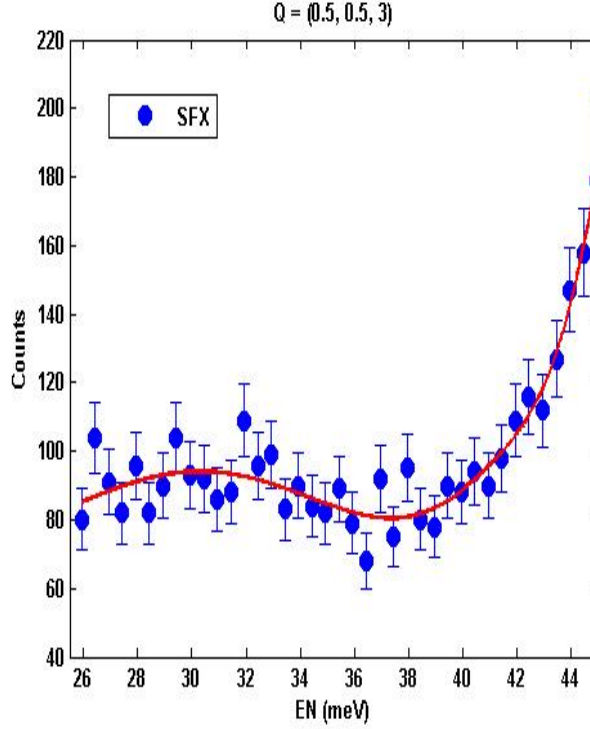


Figure 5.16: *Energy scan at fixed  $Q$  (0.5,0.5,3) . Only the  $SF_x$  is shown. Maybe there is a very low intensity peak placed around  $\sim 31$  meV ( $\chi^2 = 0.761$ ).*

### 5.3.3 Spin-wave dispersions

Figure 5.20 and 5.19 show the measured spin wave dispersions (obtained from the polarized neutron data analysis shown above) with their relative fits, along the high symmetry directions (0,0,1) and (h,h,3) respectively. To fit our experimental data we considered the simple spins 1/2 interacting system described above. In first instance we considered just intra-layer and inter-layer nearest neighbour exchange interactions  $J_{ab}$  and  $J_c$  respectively as suggested in the literature [17, 18, 19]. Then we tried to include even the inter-layer next neighbour interaction,  $J'_c$ , as suggested by Johannes et al. [24]. To calculate the spin-wave excitations we used the module **mcdisp** of the package **McPhase** (DMD algorithm described in section 3) while the module **siman-**



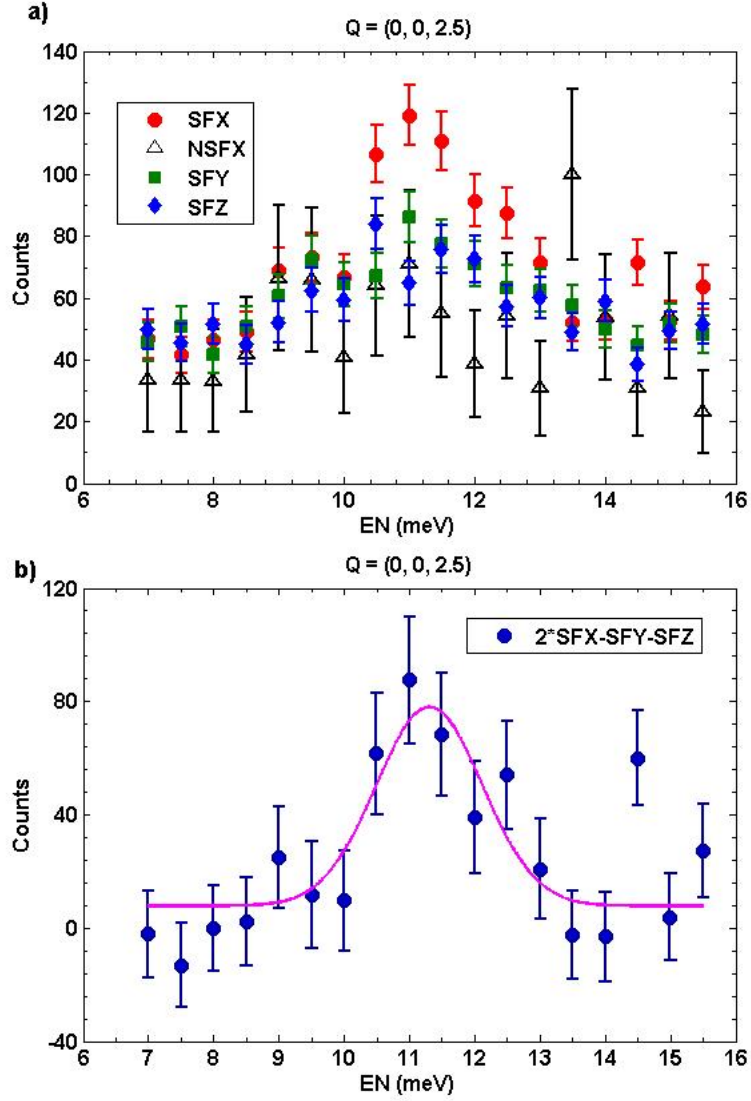


Figure 5.17: a) Energy scan at  $(0,0,2.5)$ . The counts are very low. Nonetheless the SF is higher than the NSF one. b) The xyz-polarization analysis result in well resolved peak in zero background easily fitted by a Gaussian function.  $\chi^2=1.409$

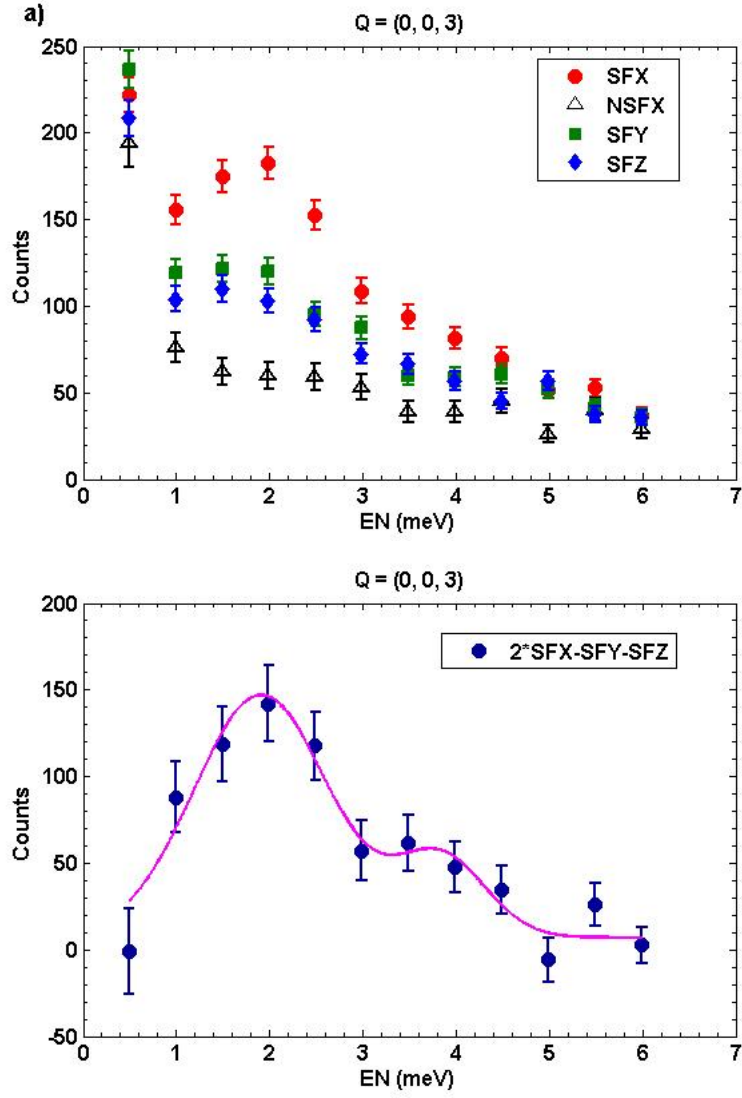


Figure 5.18: a) Energy scan at zone centre  $(0,0,3)$ . The SF signal indicated that the gap is magnetic and it seems to be single rather double b) an additional peak is necessary to have a good fit.  $\chi^2 = 1.780$

**nfit** has been used to fit the data.

The symmetry of our magnetic system implies that dispersion along the direction  $(0,0,l)$  is independent of the intra-layer exchange parameter,  $J_{ab}$ , and it depends only on the inter-layer exchange coupling parameter,  $J_c$ . Thus fitting the inelastic data along this direction, we are able to estimate it. We obtained an anisotropic diagonal inter-layer exchange tensor  $J_c^{ii}=(-11.171(4), -11.171(4), -11.327(4))$  meV ( $\chi^2=0.564$ ). An anisotropic inter-layer exchange coupling tensor was necessary to fit the observed single gap at zone centre. With an isotropic inter-layer coupling tensor the gap disappears. In particular the  $J_c^{zz}$  component of this tensor corresponds to the value of the energy dispersion at zone boundary. Fitting the dispersion along the direction  $(h,h,3)$ , we obtained for the intra-layer exchange coupling a diagonal isotropic tensor  $J_{ab}^{ii}=(5.333(9), 5.333(9), 5.333(9))$  meV ( $\chi^2=0.197$ ).

These values of the exchange parameters are slightly different from those of Helme et al. [18]. This might be expected because our sample doping is closer to that of Helme et al. than to that of Bayrakci et al. On the other hand the calculated dispersion is independent of the choice of the anisotropy  $D_z$ , the only requirement is  $D_z > 0$ .

These results seem to confirm in part what has been observed at different doping levels in the weak magnetic phase of this system[17, 18, 19]: the magnetic correlations in  $\text{Na}_{0.77}\text{CoO}_2$  are of three-dimensional nature, despite its highly two-dimensional physical properties.

Nevertheless recent DFT calculations performed by Johannes et al. [24] have shown that, including also the next nearest neighbour inter-layer spin cou-

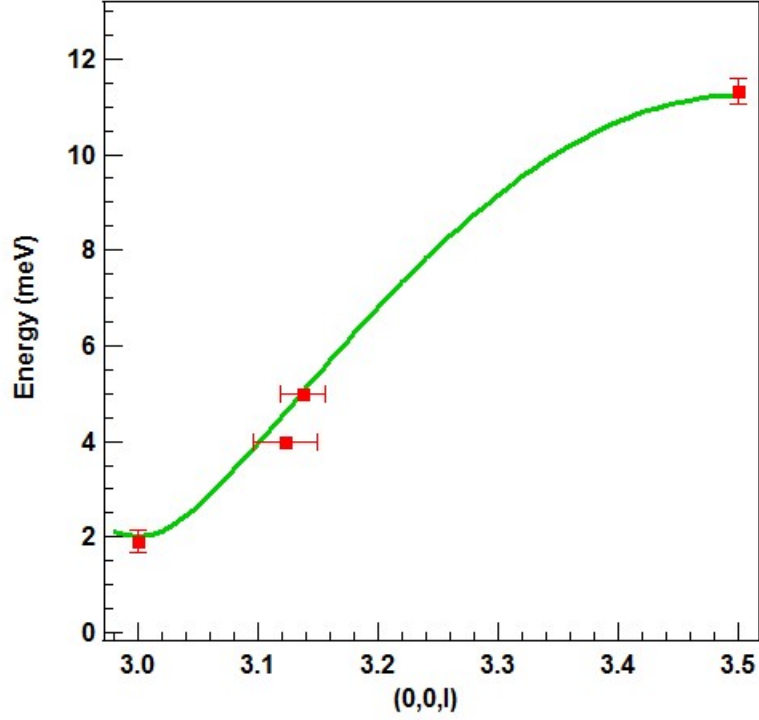


Figure 5.19: *Calculated dispersion along the direction  $(0,0,l)$  (green line) and relative inelastic data (red squares)  $\chi^2=0.564$ .*

pling,  $J'_c$ , the magnetism is really two dimensional. The authors of this work obtained a value for inter-layer coupling parameters of  $J_c=1.98$  and  $J'_c=0.22$  meV for a level of doping  $x=0.82$ . These values are small as than the in plane spin coupling  $J_{ab}$ , and more consistent with two-dimensional magnetism.

On the basis of these results, we tried to fit again our experimental data including the next nearest neighbour inter-layer spin coupling interactions,  $J'_c$ . Now the spin-wave dispersion along the direction  $(0,0, l)$  depends on both the nearest neighbour and next nearest neighbour inter-layer spin coupling constants,  $J_c$  and  $J'_c$  respectively. In particular, the dispersion along this direction depends on the sum  $J_c + 6J'_c$  and not on  $J_c$  and  $J'_c$  separately. The multiplication of  $J'_c$  by 6 is due to the fact that the number of the inter-

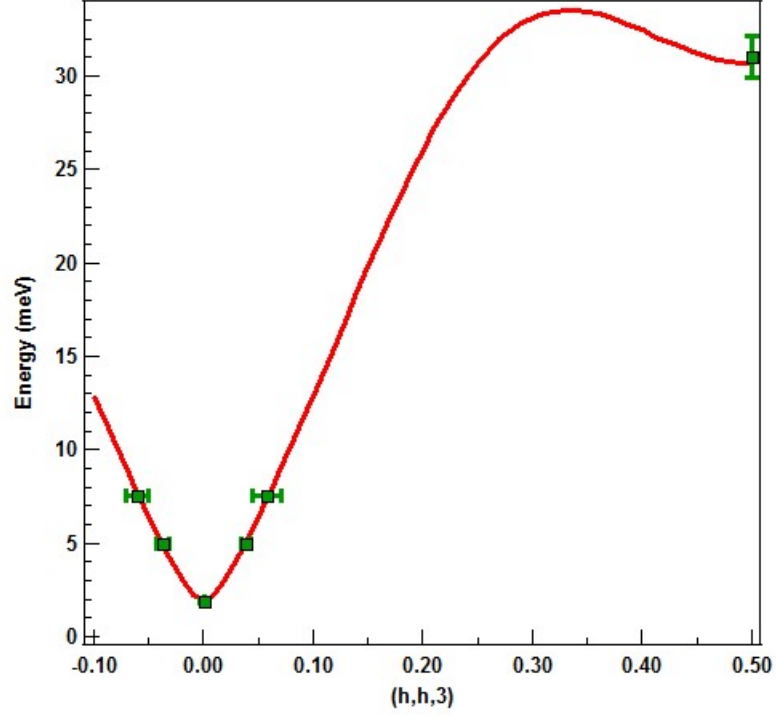


Figure 5.20: *Calculated dispersion along the direction  $(h,h,3)$  (red line) and relative inelastic data (green squares)  $\chi^2=0.197$ .*

layer next nearest neighbour is 6 times bigger than that one of the inter-layer nearest neighbours (see figure 5.21 ). Thus it is not possible to obtain the values of the inter-layer exchange coupling constant fitting the dispersion along  $(0,0,1)$ ; the only information we can gain from the dispersion along this direction is that the energy at zone boundary corresponds to  $J_c^{zz}+6J_c^{'zz}$ . Hence we have the constraint  $J_c+6J_c' = -11.327(4)meV$ . All the dispersion curves for which this equality is verified are degenerate and are identical to the curve characterized by  $J_c^{zz} = 11.327(4) meV$  and  $J_c^{'zz} = 0$ , we obtained before. In order to understand whether the nature of the magnetism in  $Na_xCoO_2$  is 3-dimensional or 2-dimensional or something in between, we fitted again our data along the other high symmetry direction  $(h,h,3)$  for various combinations

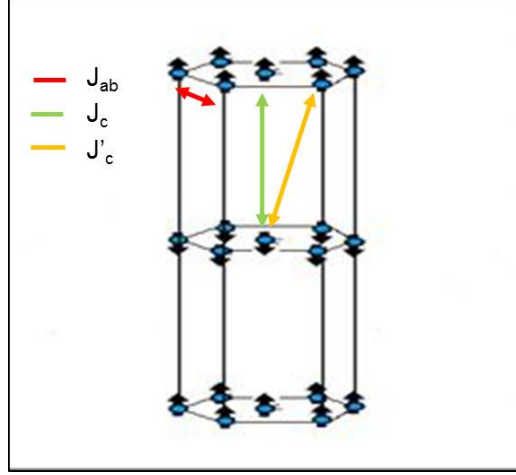


Figure 5.21: *The theoretical model of Johannes et al. [24] including also the inter-plane next neighbours interactions,  $J_c$  ( yellow arrow ) together with the intra-plane and inter-planes nearest neighbours interaction,  $J_{ab}$  ( red arrow ) and the  $J_c$  ( green arrow ) respectively already considered in our and previous works [17, 18, 19].*

of  $J_c^{zz}$  and  $J_c'^{zz}$ . We started from the limiting case  $J_c = -11.33$  meV and  $J_c' = 0$  and, increasing step by step  $J_c'$ , we arrived to the case  $J_c = -0.23$  meV  $J_c' = -1.85$  meV.

The  $J_{ab}$  intra-plane exchange parameters resulting from our fits, are listed in table 5.5 while figure 5.22 shows the corresponding dispersion curves. A qualitative agreement between experiment and theory is obtained for all the calculated curves. On the other hand the minimum  $\chi^2$  value is given by the dispersion curve characterized by  $J_c' = 0$  and  $J_c = -11.327$  meV and this seems to indicate that the magnetic correlation in  $\text{Na}_{0.77}\text{CoO}_2$  are of three-dimensional nature or that maybe there is another operative mechanism behind this high inter-plane spin coupling constant. However we have to consider that the  $\chi^2$  values have been calculated on a low number of experimental points thus we can not exclude a priori this or that model on the basis of

| $J_c^{zz}$ (meV) | $J_c^{xx,yy}$ (meV) | $J_c'^{zz}$ (meV) | $J_c'^{xx,yy}$ (meV) | $J_{ab}$ (meV) | $\chi^2$ |
|------------------|---------------------|-------------------|----------------------|----------------|----------|
| fixed            | from fit            | fixed             | from fit             | from fit       | -        |
| -0.227           | -0.204(9)           | -1.85             | -1.832(7)            | 4.721(3)       | 6.012    |
| -2.327           | -2.313(2)           | -1.5              | -1.479(5)            | 4.680(4)       | 3.602    |
| -5.927           | -5.886(6)           | -0.90             | -0.881(4)            | 4.865(1)       | 1.074    |
| -11.327          | -11.171             | 0                 | 0                    | 5.333(9)       | 0.197    |

Table 5.5: *The intra-plane exchange constant ,  $J_{ab}$ , and the  $J_c^{xx,yy}$  components of the inter-plane nearest and next neighbours exchange constants,  $J_c$  and  $J_c'$ , obtained by fitting the dispersion along the direction  $(h,h,3)$ .*

those  $\chi^2$  values. We have to consider that the model consistent with the 2-dimensional magnetism suggested by Joannes et al. and based on DFT calculations, reproduces very well the dispersions of Bayracki et al. for a level of doping  $x=0.82$  [24, 17]. Thus maybe this model need to be refined in order to explain also our results.

However both our results and those present in the literature seem to confirm that the sodium ions and especially their particular patterning play an important role in the transport and magnetic properties. In a recent work it has been suggested that the  $\text{Na}^+$  patterning determines the Coulomb landscape in Co planes, and this depends very sensitively on the Na superstructure [7]. In particular for a doping level  $x \sim 0.80$ , the electrostatic potential due to the  $\text{Na}^+$  ions is expected to localize spin  $S=1/2$  holes in potential well depth  $\sim 100$  meV. Hence the local moment picture described by the Heisenberg Hamiltonian.

In conclusion we measured the spin wave dispersion in  $\text{Na}_{0.77}\text{CoO}_2$  using polarized neutrons. We used the polarization analysis to separate the phonon contribution from the magnetic signal. Our inelastic data are well fitted assuming a simple local moment approach suggested in the literature [18, 19, 17].

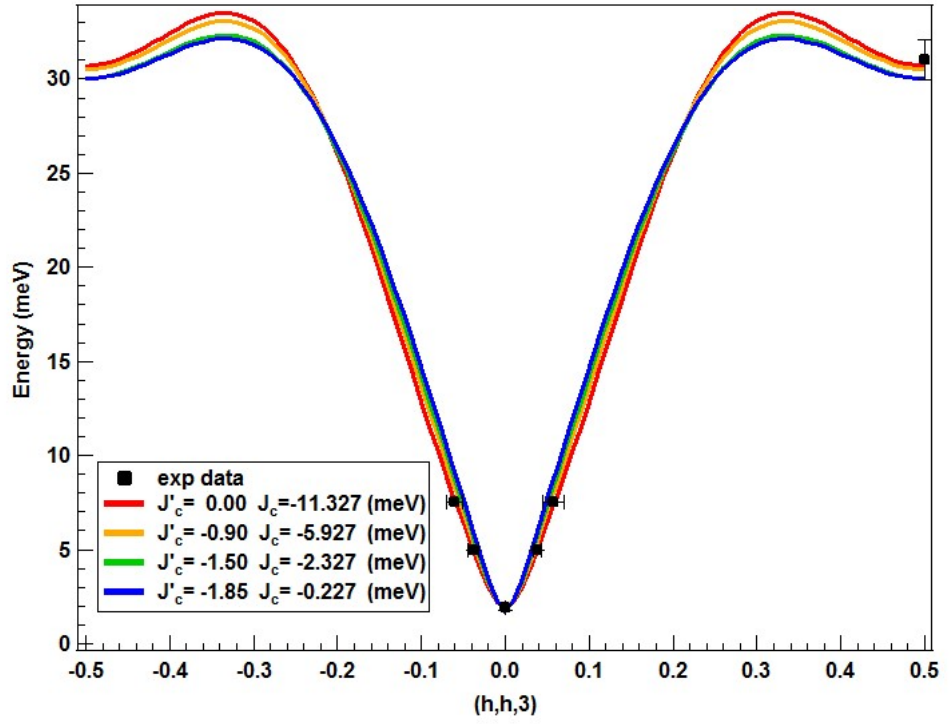


Figure 5.22: Comparison between the dispersion calculated with different values of the inter-plane neighbours parameters,  $J_c$  and  $J'_c$ . All the dispersion curves are comparable in the error bars with the experimental data. However the minimum  $\chi^2$  is given by the dispersion curve with  $J'_c=0$ .



We observed a gap in the spin wave excitations at the zone centre  $\mathbf{Q}=(0,0,3)$  and this is consistent with previous inelastic measurements [17, 18, 19] and the presence of this gap is a clear sign of magnetic anisotropy. This is consistent with the observed magnetic structure in which the spins of the cobalt ions are antiferromagnetically aligned along the c direction (A-type AF). This gap is single and not double as observed by Helme et al. [19]. We have tried to explain the presence of this anisotropy and consequently the formation of the ordered magnetic structure in terms of crystal field effects. Nevertheless the point charge approximation is insufficient for a conductor like  $\text{Na}_x\text{CoO}_2$  and much more accurate ligand theory is necessary to describe the action of the oxygen ions (and maybe also the sodium ions) which surrounds the magnetically active cobalt. We tried to fit our inelastic data assuming a simple Heisenberg Hamiltonian in which also the inter-plane next nearest neighbour interaction, which is consistent with a two-dimensional magnetism as one may expect from this system. Quantitative agreement is obtained, but the accuracy of the fits make it difficult to distinguish between different models. The best agreement in terms of  $\chi^2$  is reached when only the inter-plane nearest neighbour interactions are considered and this seems to indicate that the nature of magnetic correlation in  $\text{Na}_{0.77}\text{CoO}_2$  is three-dimensional. However further investigations are necessary to address this point.

# Bibliography

- [1] Q. Huang, M.L. Foo, R.A. Pascal, J.W. Lynn, B.H. Toby, Tao He, H.W. Zandbergen, and R.J. Cava *Phys. Rev. B* 70,184110 (2004)
- [2] M.L. Foo, Y. Wang, S. Watauchi, H.W. Zandbergen, T. He, R.J. Cava and N.P. Ong *Phys. Rev. Lett.* 92, 247001-1 (2004)
- [3] T. Tanaka, S. Nakamura and S. Lida *Jpn. J. Appl. Phys.* 33, L581 (1994)
- [4] K. Takada et al. *Nature(London)* 422,53 (2003)
- [5] Lucy Helme Thesis *Neutron Scatterins Studies on Correlated Electron System*, University of Oxford (2006)
- [6] I. Terasaki, Y.Sasago and Uchinokura *Phys. Rev. B* 56, R12685 (1997)
- [7] M.Roger, D.J.P. Morris et al. *Nature* 445,631 (2007)
- [8] D.J.P. Morris et al. *Phys. Rev. B.* 79,101103(R) (2009)
- [9] Y.Y. Wang, N.S. Rogado, R.J. Cava and N.P. Ong *Nature* 423,425 (2003)
- [10] T. Fujimoto et al. *Phys. Rev. Lett.* 92,047004 (2004)
- [11] W. Higemoto et al. *Phys. Rev. B* 70 134508 (2004)

- [12] C.J. Milne et al. *Phys. Rev. Lett.* *93*,247007 (2004)
- [13] D. Prabhakaran et al. *Axiv.0312493*
- [14] T. Motohashi et al. *Phys. Rev. B* *67*,064406 (2003)
- [15] J. Sugiyama et al. *Phys. Rev. B* *67*,214420 (2003)
- [16] J. Sugiyama et al. *Phys. Rev. Lett.* *92*,017602 (2004)
- [17] S.P. Bayrakci et al. *Phys. Rev. Lett.* *94*,157205 (2005)
- [18] L.M. Helme, et al. *Phys. Rev. Lett.* *94*,157206 (2005)
- [19] L.M. Helme et al. *Phys. Rev. B* *73*,054405 (2006)
- [20] T. Kroll dissertation thesis *On the electronic structure of layered sodium cobalt oxide, Dresden (2006)*
- [21] M. Rotter et al. *J. Phys. Condens Matter* *24*,213201 (2012)
- [22] M.T. Hutchings et al *Solid State Phys.* *16*,227 (1964)
- [23] [http://www.cpfs.mpg.de/~rotter/homepagemcphase/manual/  
manual.html](http://www.cpfs.mpg.de/~rotter/homepagemcphase/manual/manual.html)
- [24] M.D. Johannes, I.I. Mazin and D.J. Singh *Phys. Rev. B* *71*, 214410 (2005)
- [25] M. Pandiyan Ph D. Thesis *Phase Diagram and Control of Thermoelectric Properties of Sodium Cobaltate* Royal Holloway University of London (2013)

# Chapter 6

## Spin-waves in $\text{MnV}_2\text{O}_4$

### 6.1 5.1 Introduction to $\text{MnV}_2\text{O}_4$

$\text{MnV}_2\text{O}_4$  belongs to the class of vanadium spinels,  $\text{AV}_2\text{O}_4$ . In these compounds the  $\text{V}^{3+}(\text{d}^2)$  ion is characterized by the occupancy of two of the three-fold degenerate  $t_{2g}$  orbitals which are lowered by the crystal field effect from the octahedral arrangement of surrounding ions. Furthermore the magnetically active  $\text{V}^{3+}$  ( $S=1$ ) ions form a pyrochlore lattice with corner-sharing tetrahedra that is magnetically frustrated. The site A is occupied by the  $\text{Mn}^{2+}$  ion, which is in the  $3\text{d}^5$  high-spin configuration with no orbital degrees of freedom, and therefore it can be regarded as a simple  $S=5/2$  spin [1]. In such systems where both orbital and spin degeneracies are present, the low temperature physics becomes very intriguing. In fact the orbital, spin and lattice degrees of freedom may mutually interact leading to complex structural/magnetic ordering and excitations [2]. Moreover the presence of the magnetic manganese ions leads to a ferrimagnetic structure and hence it is potentially possible to control both

magnetism and the orbital physics via an applied field.

$\text{MnV}_2\text{O}_4$  exhibits two phase transitions: at  $T_N=56$  K it transforms from a paramagnet to a collinear ferrimagnet with the Mn and V magnetic moments aligned along the  $c$  axis in opposite directions. At  $T_s=53$  K a structural phase transition from cubic to tetragonal occurs and associated with it, there is a further transition in which the spin structure changes from the collinear structure to a non-collinear *triangular* configuration [3]. This suggests that the lower temperature transition is dominated by the orbital degrees of freedom on the V site, and there is an interplay between orbital and spin degrees of freedom in this compound. In fact, subsequent magnetostriction measurements have shown that the structural transition may be induced by the application of a magnetic field [1, 4]. This transition involves a compression of the  $\text{VO}_6$  octahedron along the  $c$  axis and a small distortion of the V-O bonds in the basal plane as shown by diffraction measurements [3, 4]. This relieves further the degeneracy of the  $t_{2g}$  orbitals of vanadium splitting them into a non-degenerate  $d_{xy}$  orbital and doubly degenerate  $d_{xz}$ ,  $d_{yz}$  orbitals at higher energy. To lift the degeneracy of the second electron many models have been proposed in the literature giving rise to various orbital orderings and related magnetic structures.

Tsunetsugu et al. proposed an *antiferro-orbital* order in which the  $xz$  and  $yz$  orbitals are alternately occupied along the  $c$  axis [5]. Tchernyshyov and Di-Matteo et al. instead, taking account of the relativistic spin-orbit coupling, suggested an orbital ordering in which the second electron can occupy a superposition of orbitals of the kind  $d_{xz} \pm d_{yz}$ . They both have a non-zero orbital

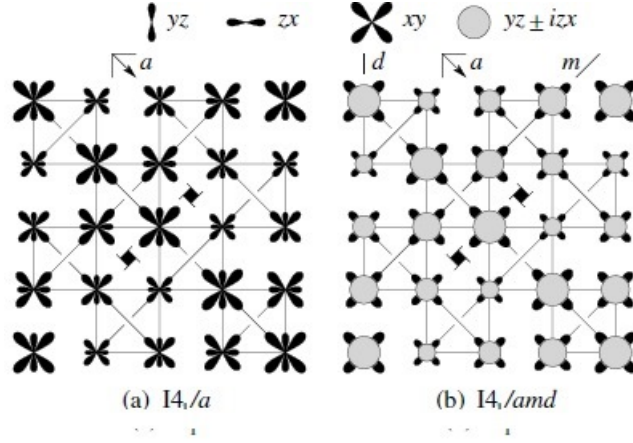


Figure 6.1: d

irection.] *Orbital order of vanadium ions below the structural phase transition. A view down the  $[001]$  direction. a) The result of Tsunetsugu and Motome [5] and b) Tchernyshyov and Di Matteo [6, 7]*

moment (see figure 6.1) [6, 7].

Recent density functional calculations by Sarkar et al. suggested a *ferro-orbital* ordering in which the first electron is in a more complex orbital state with mainly xy character and a bit of xz character. The second electron occupies an orbital with mainly yz character instead of an alternating occupation of xz and yz. These orbitals form chains along the a and b direction and they are rotated within each chain alternately by an angle of about 45 degrees as shown in figure 6.2. The authors explain this rotation of orbitals in terms of trigonal distortion present in both the ab plane and along the c axis [8].

The determination of the low temperature tetragonal space group  $I4_1/a$  (instead of the  $I4_1/amd$  observed in the related compounds with A non-magnetic) by X-ray diffraction measurements, lead Suzuki et al. to support the *antiferro-orbital* model of Tsunetsugu et al. (see figure 6.3) [4]. Such orbital ordering is characterized by strong antiferromagnetic spin coupling along the *ferro-orbital*

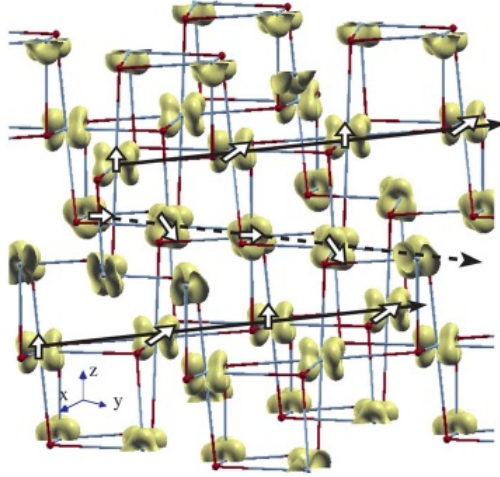


Figure 6.2: *Three-dimensional electron density plot showing the orbital ordering proposed by Sarkar et al. The black solid and dashed lines designate the orbital chains. The arrows superimposed on the electron density at each  $v$  site mark the rotation sense of the orbitals as one moves to the neighbouring  $V$  sites within a given chain. [8]*

chains running along the directions  $a$  and  $b$ . On the other hand *antiferro-orbital* order along  $c$ , gives rise to a small ferromagnetic coupling between chains [4, 5]. High-resolution neutron diffraction measurements performed by Garlea et al. seemed to confirm this model. A group theory analysis of their data resulted in a ferrimagnetic structure with Mn moments aligned along the tetragonal  $c$  axis, while V moments can have components on any of the three crystal axes. The  $a$  and  $b$ -axis components are constrained to form an orthogonally stacked anti-ferromagnetic structure as shown in figure 6.4 [9]. The V moments are canted with the respect to the  $c$ -axis by 65 degrees. This is in contrast to the magnetic ground state proposed previously by Plumier et al. in which the vanadium moments instead lie in  $(h\ 0\ 0)$  planes and are canted with respect to the  $c$  axis by  $\sim 63$  degrees (see figure 6.5) [3].

Nevertheless many aspects concerning the relationship between the orbital

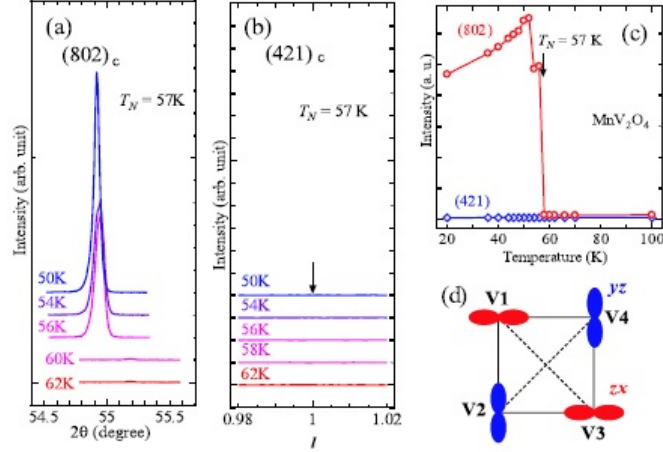


Figure 6.3: *Temperature dependence of x-ray diffraction of the  $\text{MnV}_2\text{O}_4$  single crystal around (a) the  $(802)_c$  and (b) the  $(421)_c$  peaks in the cubic setting, and (c) the temperature dependence of their intensities. (d) Schematic picture of  $t_{2g}$  orbitals in one tetrahedron. V1 and V3 are on the same layer, which is above the layer containing V2 and V4 [4].*

ordering and the magnetic structure are still unclear. The magnetic structure suggested by Garlea et al. and related orbital ordering implies the quenching of V orbital angular momentum. This is not consistent with the significant spin-orbit coupling on the  $\text{V}^{3+}$  (13-20 meV) ion [10] and the observation of a finite gap at zone centre in the spin-wave excitation spectrum [9]. Spin wave measurements performed by Chung et al. showed that the inter-chain coupling,  $J'_{BB}$  is anti-ferromagnetic instead of ferromagnetic and of an order of magnitude close to the intra-chain coupling,  $J_{BB}$  [12]. Furthermore the authors stated that their inelastic neutron scattering data were better fitted using the Plumier magnetic ground state than the magnetic structure of Garlea.

In this chapter we will show the comparison between our spin wave dispersion calculations, performed with a dynamical matrix diagonalization (DMD) approach [13], and our inelastic polarized neutron data. The ground state mag-



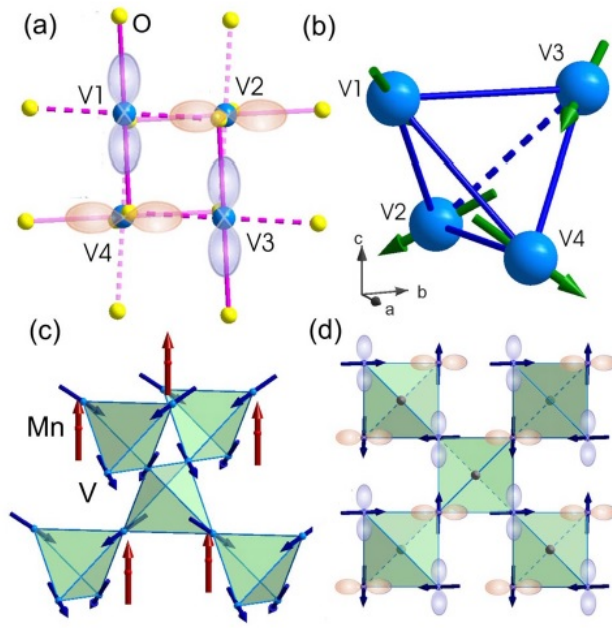


Figure 6.4: (a) Projection of the V tetrahedron in the  $ab$  plane. V-O bonds are arranged in an alternating pattern giving rise to a staggeredlike orbital ordering. (b), (c) Graphical representation of the low-temperature non-collinear ferrimagnetic structure of the  $\text{MnV}_2\text{O}_4$ . The Mn moments are aligned parallel to the  $c$  axis, while the V moments are canted by approximately 65 degrees. (d) Projection of the magnetic structure on the basal plane [9].

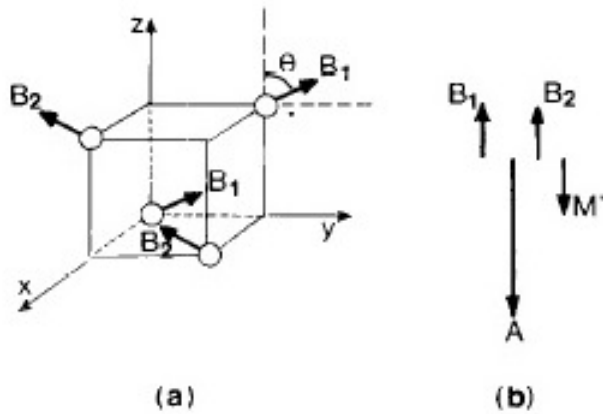


Figure 6.5: Plumier magnetic structure. (a) Basic magnetic cell in the case of the triangular magnetic structure; the moments on the A sites are along  $[001]$ ; (b) the Neel ferrimagnetic configuration [3].

netic structure has been calculated by a mean-field Monte-Carlo method. This method is used to diagonalize the Hamiltonian composed of a single-ion term which includes electron-electron Coulomb, spin orbit and crystal field interactions and, as the second term, a nearest-neighbour Heisenberg Hamiltonian. The DMD and the mean field Monte-Carlo algorithm were both provided by the software McPhase [14].

## 6.2 Calculation of the $\text{MnV}_2\text{O}_4$ ground state magnetic structure with McPhase

As in the case of  $\text{Na}_x\text{CoO}_2$ , the magnetic structure and excitations in  $\text{MnV}_2\text{O}_4$  are described by the Hamiltonian

$$\hat{\mathcal{H}} = \sum_{n=1}^N \hat{\mathcal{H}}(n) - \frac{1}{2} \sum_{n,n',\alpha,\beta} J_{\alpha\beta}(R_{n'} - R_n) \hat{S}_{\alpha}^n \hat{S}_{\beta}^{n'} \quad (6.1)$$

presented already in chapter 4 for the  $\text{Na}_x\text{CoO}_2$ . The first term represent the Hamiltonian of a subsystem that in our case is a single magnetic ion. The  $\text{Mn}^{2+}$  is just a simple spin  $S=5/2$  system with no orbital degrees of freedom ( $L=0$ ).  $\text{V}^{3+}$  is considered as the free ion under the action of the crystal field due to the surrounding oxygen ions. The second term, assumes again the typical form of Heisenberg exchange coupling Hamiltonian with  $J_{\alpha\beta}(i, j)$  diagonal isotropic or anisotropic tensors.

The crystal field (CF) interactions,  $\mathcal{H}_{CF}$ , due to surrounding oxygen are again stronger than electron-electron (Coulomb) interactions,  $\mathcal{H}_{e-e}$ , and spin-

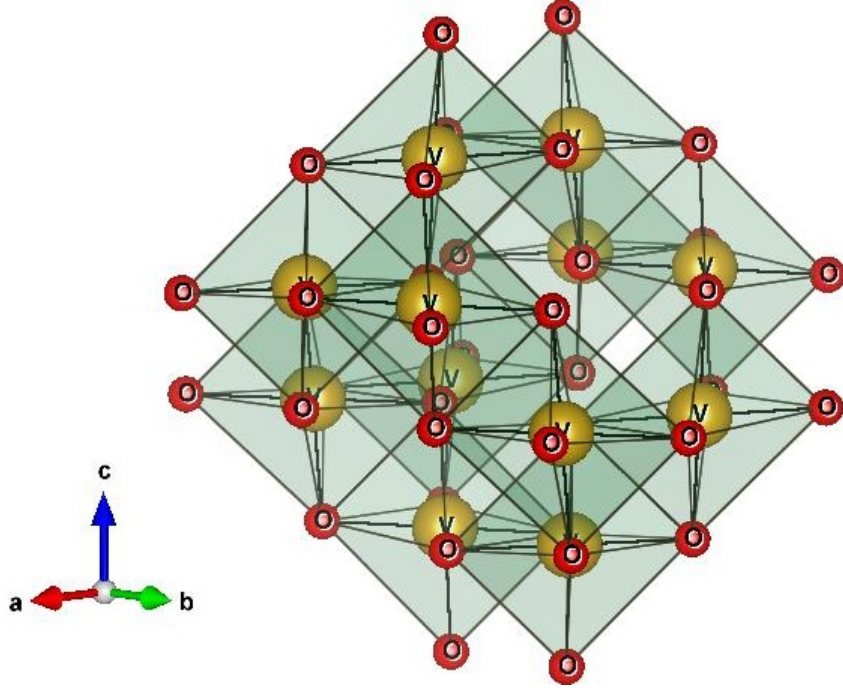


Figure 6.6: *The  $\text{VO}_6$  octahedra. They are trigonally distorted and compressed along the  $c$  direction at base temperature. The V-O bonds along the  $c$  axis, are 2% shorter than the  $ab$  plane V-O bonds.*

orbit interactions,  $\mathcal{H}_{SO}$ . Thus in the single-ion Hamiltonian the strong CF is considered to act first on single-electron states, splitting the degenerate orbital levels. Then eventually the Coulomb and the spin-orbit interactions (treated as perturbations) will further remove the degeneracies of the CF levels obtained. The  $\text{V}^{3+}(\text{d}^2)$  ions sit at the centre of distorted octahedra whose vertices are occupied by the oxygen  $\text{O}^{2-}$  ions. This kind of crystal field configuration is expected to lift the degeneracy of the 3d orbitals energy splitting them into lower lying  $t_{2g}$  and higher lying  $e_g$  orbitals. Figure 6.6 shows the trigonally distorted  $\text{VO}_6$  octahedra which characterize the crystal structure of  $\text{MnV}_2\text{O}_4$  (manganese ions have been omitted to simplify the view). As explained in the introduction, the transition from cubic to tetragonal symmetry, is associated with a compression of the  $\text{VO}_6$  octahedron along the the  $c$ -axis with

| Atom | Site | x       | y           | z          |
|------|------|---------|-------------|------------|
| Mn   | 4a   | 0       | 0.75        | 0.125      |
| V    | 8d   | 0       | 0           | 0.5        |
| O    | 16f  | 0.0059* | 0.02424(89) | 0.7381(12) |

Table 6.1: *Atomic parameters of  $\text{MnV}_2\text{O}_4$  at 2 K [ $I4_1/a$ ,  $a = 6.0250(8) \text{ \AA}$ ,  $c = 8.5142(8) \text{ \AA}$ ] [15] \*this position is taken from Sarkar et al. calculations [8].*

$c_T/a_T=0.98$ . This is expected to lift furthermore the degeneracy of the  $t_{2g}$  levels, lowering the energy of the  $d_{xy}$  orbital. The (CF) effects have been evaluated in the point-charge approximation [16] in which only the electrostatic interactions of surrounding ions are included. This approximation is expected to work better for insulating  $\text{MnV}_2\text{O}_4$  than for conducting  $\text{Na}_x\text{CoO}_2$ .

The positions of the oxygen ions relative to vanadium ions have been calculated using the space group parameters obtained from previous neutron diffraction data refinements shown in table 1 [15]. For the position x of the oxygen we adopted that obtained by Sarkar et al. who used a local spin density approximation method with the inclusion of correlation effects (LSDA+U) to optimize the structural parameters [8]. Their results are consistent with the neutron diffraction data, but neutron diffraction is not sensitive to a displacement that is this small. This feature is very important because it differentiates the space group  $I4_1/a$  from  $I4_1/amd$ . The consequence of it is that mirror and glide symmetry will be absent in the  $I4_1/a$  space group and two of the four V-O bonds in the  $ab$  plane will be shorter, whereas in the other case all four V-O bonds have the same length.

Four equivalent oxygen ion configurations can be identified in the crystal structure of this system. They differ from each others by a rotation of  $90^\circ$

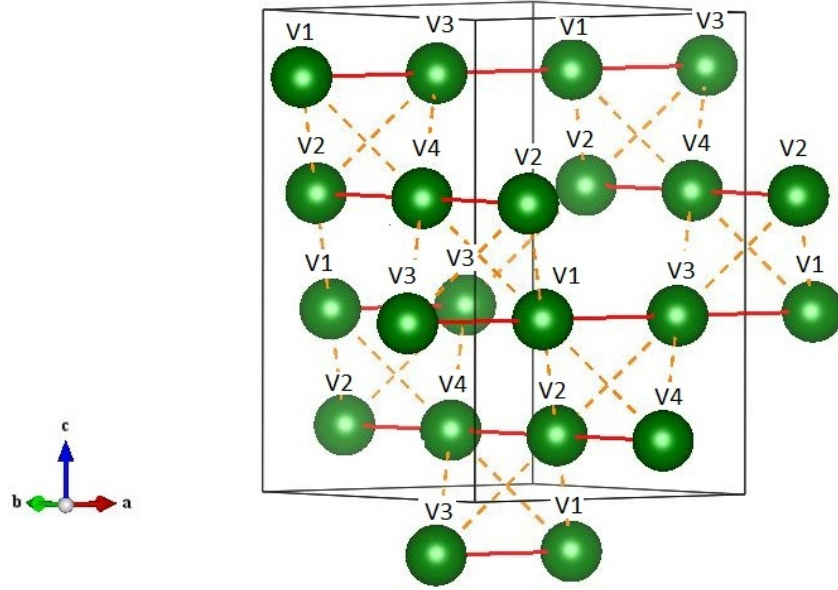


Figure 6.7: *The four subsystems given by the vanadium ion and one of the four oxygen surrounding configurations. Chains of V1-V3 along  $\vec{a}$  and V2-V4 along  $\vec{b}$ . Intra-chain and inter-chain interactions in red lines and yellow dashed lines respectively.*

along the z-axis. Hence we deal with four subsystems composed of a  $V^{3+}$  ion and its own oxygen octahedral configuration. They are placed at the vertices of tetrahedra as shown in figure 6.7. We labelled each subsystem by V1, V2, V3 and V4 and we can see an alternation of V1 and V3 along the a direction and an alternation of V2 and V4 along the b direction. The vanadium crystal field parameters, calculated using the point-charge approximation for each set of external oxygen configurations are listed in table 6.2. The parameters B40 and B44 are compatible with the tetragonal symmetry of the system while B43 (or B43S) is due to the trigonal distortion. The presence of the other parameters is due to the fact that the octahedra are not aligned along a high symmetry direction.

To calculate the single ion energy levels of  $V^{3+}$  ions we used the module

**ic1ion** of the package **McPhase** in the strong crystal field limit as explained in chapter 3. The Slater integrals,  $F_0$ ,  $F_2$  and  $F_4$  for the electron-electron interaction,  $\mathcal{H}_{ee}$ , and the spin orbit parameter,  $\lambda$  have been taken from the literature [11, 10].

The single ion energy calculations including the spin orbit coupling, give a doublet as ground state mostly characterized by  $|S = 1, L = 3, m_L = \mp 3, m_S = \pm 1\rangle$ , and as first excited states a singlet at 1.70 meV,  $(|S = 1, L = 3, m_L = 0, m_S = 0\rangle)$ , and a doublet at 2.62 meV,  $(|S = 1, L = 3, m_L = \mp 3, m_S = \pm 1\rangle)$ . Higher energy levels are above 80 meV and, therefore, they will not be important in determining the ground state magnetic structure.

It is difficult to interpret the results of these calculations because the algorithm in McPhase uses the total orbital and spin angular momenta as labels for the states that in this specific case are not good quantum numbers. Nevertheless we can say that in the ground state the two electrons are in the triplet state so that they must occupy two different orbitals. Presumably one electron occupies the non degenerate lower energy  $d_{xy}$  orbital while the other electron occupies a complex superposition of the  $d_{xz}$  and  $d_{yz}$  orbitals giving rise to an orbital angular momentum different from zero. In order to understand which kind of orbital ordering and related magnetic structure is obtained it is necessary to include the multiple ion interaction as given in the Hamiltonian 6.1.

Direct  $t_{2g}$ - $t_{2g}$  interaction between neighbouring  $V^{3+}$  spins and super-exchange interaction through the oxygen 2p orbital between  $V^{3+}$  and  $Mn^{2+}$  spins were considered. The occupation of the orbital  $d_{xy}$  in all the vanadium ions is expected to produce strong intra-chain anti-ferromagnetic coupling,  $J_{BB}$ , within

| V1   | V3    | Values (meV) | V2   | V4    | Values (meV) |
|------|-------|--------------|------|-------|--------------|
| B22S | B22S  | 3.82         | B22S | B22S  | 3.58         |
| B21S | -B21S | -3.98        | B21S | -B21S | 26.36        |
| B21  | -B21  | 26.36        | B21  | -B21  | 2.45         |
| B22  | B22   | -9.43        | B22  | B22   | 9.34         |
| B40  | B40   | -0.98        | B40  | B40   | -0.98        |
| B43  | -B43  | -1.13        | B43S | -B43S | 1.13         |
| B44  | B44   | 4.82         | B44  | B44   | 4.82         |

Table 6.2: *Point-charge calculated crystal field parameters in Blm Stevens notation.*

V1-V3 and V2-V4 ions along the tetragonal axes a and b respectively (solid lines in figure 6.7). On the other hand the occupancy by the second electron of one of the  $d_{xz}$  and  $d_{yz}$  orbitals or a superposition of them is expected to produce a smaller inter-chain coupling,  $J'_{BB}$  (dashed lines in figure 6.7). The sign and magnitude is governed by the specific orbital ordering along the z axis. The *antiferro-orbital* order suggested by Suzuki et al. is expected to produce a small and positive (ferromagnetic) inter-chain coupling. On the contrary the *ferro-orbital* arrangements of Sarkar et al. is expected to produce an anti-ferromagnetic inter-chain coupling. The exchange coupling between  $V^{3+}$  and  $Mn^{2+}$  spins,  $J_{AB}$ , is antiferromagnetic as suggested by the paramagnet to collinear ferrimagnet transition at 56 K.

As a first approximation, all the exchange coupling interactions have been parametrized by diagonal isotropic tensors. In the next section we will see that in the case of the Mn-V coupling,  $J_{AB}$ , a diagonal anisotropic tensor fits better the spin wave dispersion at the zone centre. The ground state magnetic structure corresponding to the minimum of the Hamiltonian 6.1, has been evaluated using the self-consistent mean field Monte Carlo algorithm provided

by the software McPhase [14].

The results are shown in figure 6.8. On the left, manganese and vanadium spins form a non-collinear anti-ferromagnetic arrangement with the manganese spins oriented parallel to the  $c$  axis whereas the vanadium spins are tilted by  $63^\circ$  with the respect to this axis, in good agreement with both the suggested magnetic structures (Plumier and Garlea). On the right, the  $ab$ -plane vanadium spin components lie along the  $(110)_t$  tetragonal direction forming parallel antiferro-magnetic chains along this direction as indicated by the uni-colour lines. This is in exact agreement with the Plumier magnetic structure. In fact, the tetragonal planes  $(h,h,0)_t$  in which the vanadium spin components lie, corresponds to the  $(h,0,0)$  planes in the cubic reference frame used by Plumier et al. (see figure 6.5). In our model structure the  $ab$  plane spin components are aligned along the direction  $(110)$  or  $(\bar{1}\bar{1}0)$  depending on whether the manganese spins point toward the positive or negative  $z$  respectively. This basal plane spin structure is obtained independently of the sign of the inter-chain exchange coupling  $J'_{BB}$ . Nevertheless the correct angle of canting of vanadium spin is only obtained when the inter-chain coupling is negative, antiferromagnetic coupling.

In summary this structure results from the choice of the exchange coupling parameters  $J_{AB}=1.8$ ,  $J_{BB}=11$  and  $J'_{BB}=-2$  meV suggested by Sarkar et al. [8]. These parameters will be optimized in the next section to have the best agreement with the inelastic polarized neutron scattering data. The negative value of the inter-chain coupling leads one to assume that there is *ferro-orbital* ordering along the  $c$  axis. Presumably the second electron occupies a complex



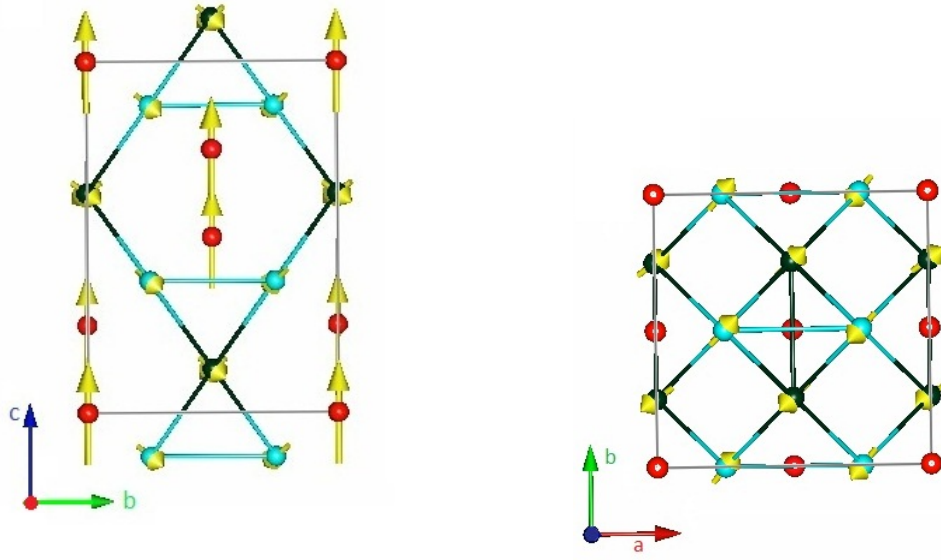


Figure 6.8: *The ground state magnetic structure of  $\text{MnO}_2\text{V}_4$ . V1, V3 ions in black and V2, V4 ions in cyan; Mn ions in red. On the left: manganese spins are parallel to  $c$  while vanadium spins are tilted by  $\sim 63^\circ$  with respect to the  $c$  axis. On the right:  $ab$  plane vanadium spin components form anti-ferromagnetic chains (uni-color lines) and are aligned along the direction  $(1,1,0)_t$  or  $(1\bar{1}0)_t$  depending on whether the manganese spins point toward the positive or negative  $z$  respectively.*

state resulting from the superposition of the  $t_{2g}$ - $t_{2g}$  orbitals because of the trigonal distortion, but it has a dominant contribution from the  $d_{yz}$  or  $d_{yz}$  depending on the orientation of the manganese spins. This is in agreement with the Sarkar DFT calculation, nevertheless further investigations are necessary to confirm or discard this hypothesis.

In conclusion, our mean field Monte Carlo studies in which single ion energy levels have been calculated, including the crystal field effects, strongly supports the Plumier magnetic structure, instead of the more recent magnetic structure proposed by Garlea. In the next section we will show the spin wave dispersion obtained using a DMD approach starting from the obtained magnetic ground state (Plumier) agrees with the inelastic polarized neutron data.

## 6.3 Spin-Wave Dispersion and Comparison with the IN20 data

Spin wave dispersions along high symmetry directions have been measured by Andrea Magee [15] using the triple axis spectrometer IN20 at the I.L.L in Grenoble (France). All measurements were performed using the unidirectional polarization analysis technique described in chapter 2. In order to preserve the neutron polarization, a vertical magnetic field of 2 T had been applied along the z direction. To calculate the magnetic dispersions we used the module **mcdisp** which includes a DMD algorithm, as explained in chapter 3. The program **mcdisp** calculates also the  $\chi^2$  factor which can be optimized using the module **simannfit**. The spin dispersions in  $\text{MnV}_2\text{O}_4$  are much more complex than those of  $\text{Na}_x\text{CoO}_2$  as shown below. They are characterized by the presence of many modes and required a lot of computational time. For this reason it was difficult, if not impossible, to use the module **simannfit** to fit our data. For this reason to fit our experimental data we proceeded in a different way. We tried to optimize the  $\chi^2$  factor acting on the exchange parameters  $J_{AB}$ ,  $J_{BB}$ ,  $J'_{BB}$  and sometimes on the spin-orbit coupling parameter,  $\lambda$ . Then we did also a graphical comparison between calculated curves and experimental data (fitting by eye). Also this second step is important when the dispersion is characterized by many modes as in our case. The values of the  $\chi^2$  factor are listed in all the figures.

Figure 6.9 shows the calculated spin wave dispersions along the tetragonal direction  $(h,1,0)_t$  which corresponds to the cubic direction  $(h+2,h,0)_c$  along

which the spin excitations were measured by A. Magee [15]. A good agreement is achieved between the calculation and the experimental data, especially for the reproduction of the crossing modes at  $(1,1,0)_t$  ( $(2,0,0)_t$ ) and the quasi-flat mode at  $\sim 10$  meV. Also some other observed features at  $\sim 8$  meV seem to be well reproduced by our calculations. The calculated intensities are not always in good agreement with those observed experimentally. This may be due to the fact that our model is not complete. The flat mode is well reproduced both in amplitude modulation and in intensity.

Figure 6.10 shows the dispersion calculated along the tetragonal direction  $(2,k,0)_t$  together with the dispersion observed experimentally along the equivalent cubic direction  $(2+h,-2+h,0)_c$ . Along this direction the agreement between experiment and calculations is quite satisfactory both in energy and in intensity.

Figure 6.11 shows the experimental results and theoretical calculations along the tetragonal direction  $(h,2-h,0)_t$  which corresponds to the cubic direction  $(2,k,0)_c$  along which the dispersion has been measured [15]. The dispersion branches indicated in red and black colour variations are more intense than those in yellow which were predicted to be very weak by our calculations. The data are in very good agreement both for the energy and for the intensity in the range from the Brioullin zone center to the half zone. Then from the half zone to the zone boundary data points are well reproduced by a lower intensity dispersion mode predicted by our calculation. The higher intensity mode in this range is predicted to be flat until the zone boundary where these two modes become nearly degenerate. Nonetheless the high intensity flat mode

| coupling constants | tensor      | values (meV)                                      |
|--------------------|-------------|---|
| $J_{BB}$           | isotropic   | -11.13(15)  |
| $J'_{BB}$          | isotropic   | -2.80(11)   |
| $J_{AB}$           | anisotropic | $J_{xx} = J_{yy} = -1.70(12), J_{zz} = -1.80(12)$ |

Table 6.3: *Exchange coupling constants.*

reproduces at least qualitatively these data points. A similar good agreement is obtained also for the  $(h, h, 0)_t$  direction (corresponding to the  $(h, 0, 0)_c$  cubic direction. This is because these two directions are equivalent in the tetragonal geometry, see figure 6.12.

The calculations of Chung et al. [12] were not able to predict the additional lower intensity feature which fit the data from the half zone to the zone boundary, but only the flat mode predicted also by our calculations, see figure 6.13. Qualitative agreement between experimental data and calculations is obtained also for the off-symmetry direction  $(1.25 + \frac{3}{8}h, 1.25 - \frac{5}{8}h, 0)$  (corresponding to the cubic off-symmetry direction  $(2.5 - h/4, -h, 0)$ ) as shown in figure 6.14. Also in that case the experimental points are well reproduced both in dispersion and in intensity from the zone centre to the half zone. Then data points are in better agreement with the lower intensity mode.

The spin coupling constants resulting from our fitting procedure are listed in table 6.3. The value of the intra-chain,  $J_{BB}$ , and inter-chain,  $J'_{BB}$ , are in good agreement with those predicted by Sarkar et al. [8] and Chung et al. [12]. For the manganese-vanadium interaction an anisotropic diagonal tensor with values of  $(J_{ab}^{xx,yy}=1.7, J_{AB}^{zz}=1.8)$  meV is required to fit the data points at zone centre. The spin-coupling parameter,  $\lambda$ , has been optimized to the value of 13.5 in accordance with values present in literature [10].

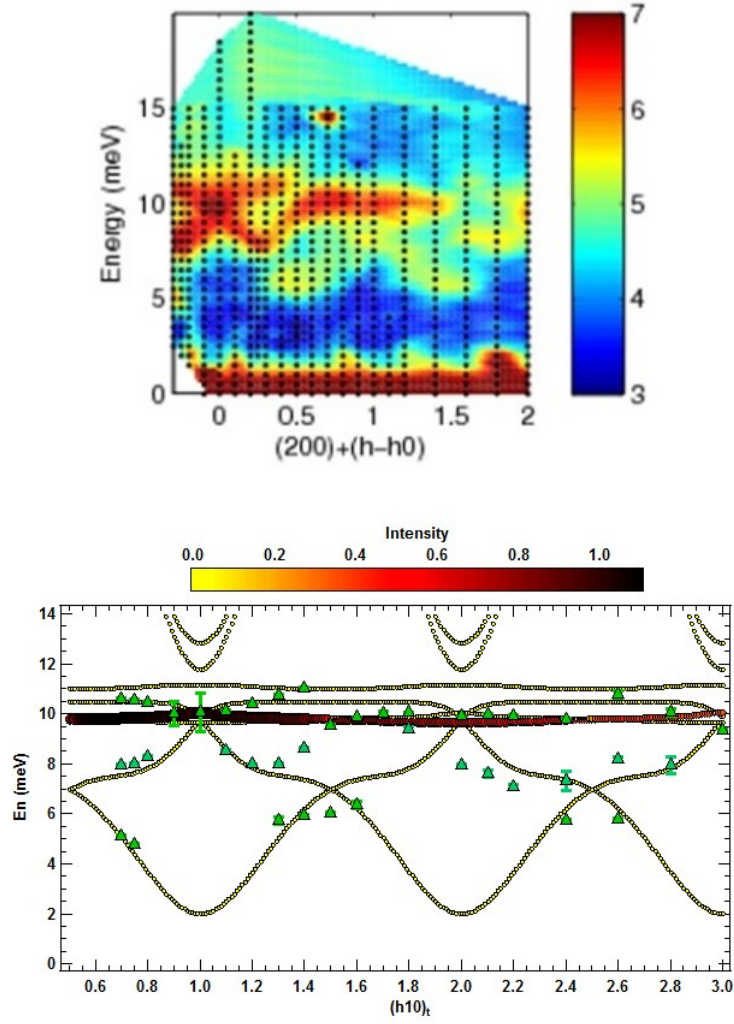


Figure 6.9: *Spin-wave dispersions measured by A. Magee along the cubic direction  $(2+h,h,0)_c$  (top) which correspond to the tetragonal direction  $(h,1,0)_t$  (bottom). Our calculation reproduces the modes which are crossing in  $(1,1,0)_t$   $((2,0,0)_c)$  and the flat mode at 10 meV. Also some other features seem to be captured by our spin wave calculation ( $\chi^2 = 12.400$ ). [15]*

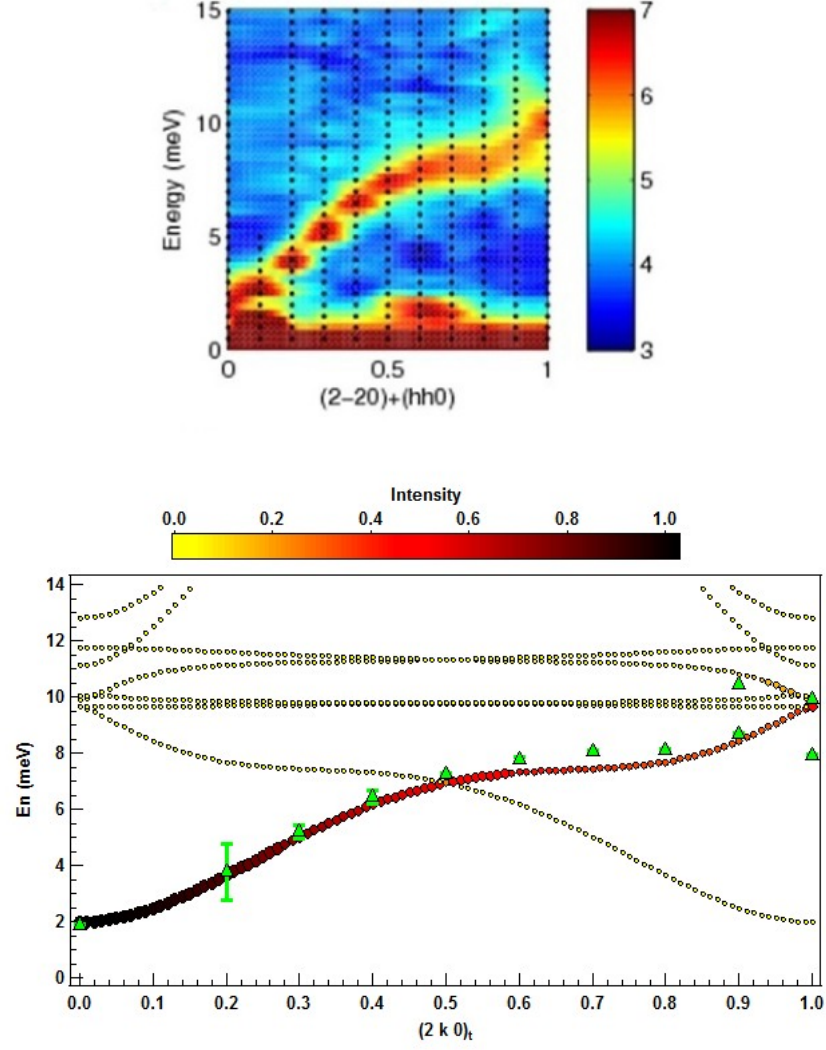


Figure 6.10: *Spin wave dispersion calculated along the tetragonal direction  $(2,k,0)_t$  (bottom) in comparison with that measured along the equivalent cubic direction  $(h+2,h-2,0)_c$  (top). The agreement between theory and experiment is satisfactory both in energy and in intensity ( $\chi^2 = 20.1$ ). [15]*

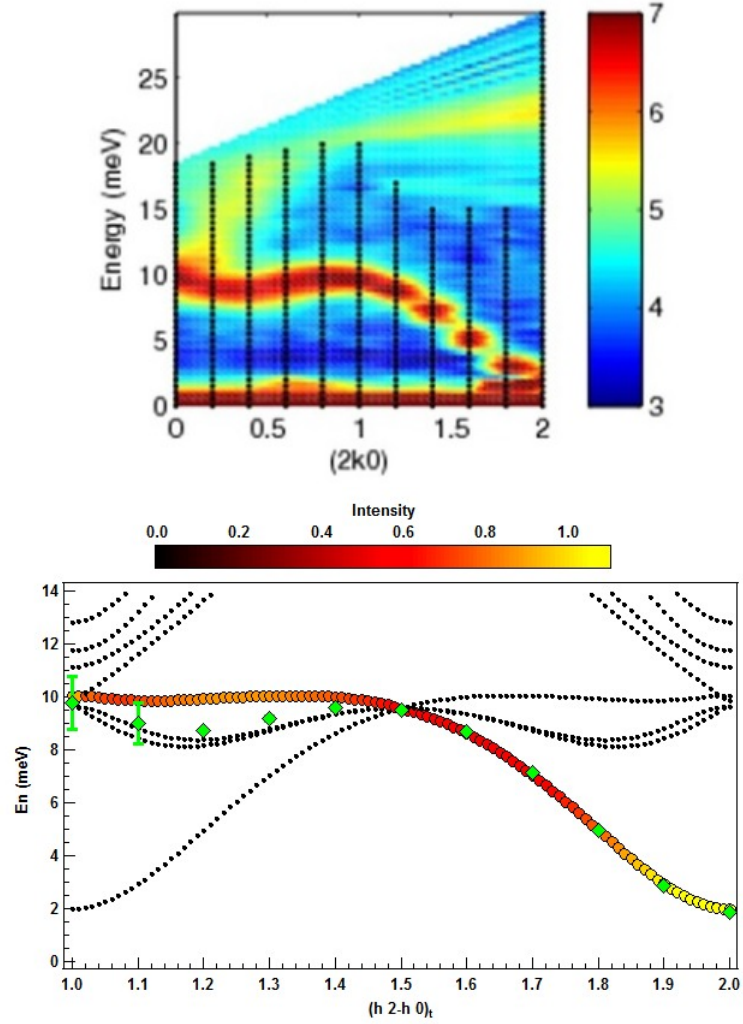


Figure 6.11: *Spin-wave dispersion calculated along the tetragonal directions  $(h, 2-h, 0)_t$  (bottom) and measured along the equivalent cubic direction  $(2, k, 0)_c$  (top). The calculated energy dispersion are in good agreement with experimental data, it is not always the same for the intensity indicated in the color map bar ( $\chi^2 = 7.042$ ). [15]*

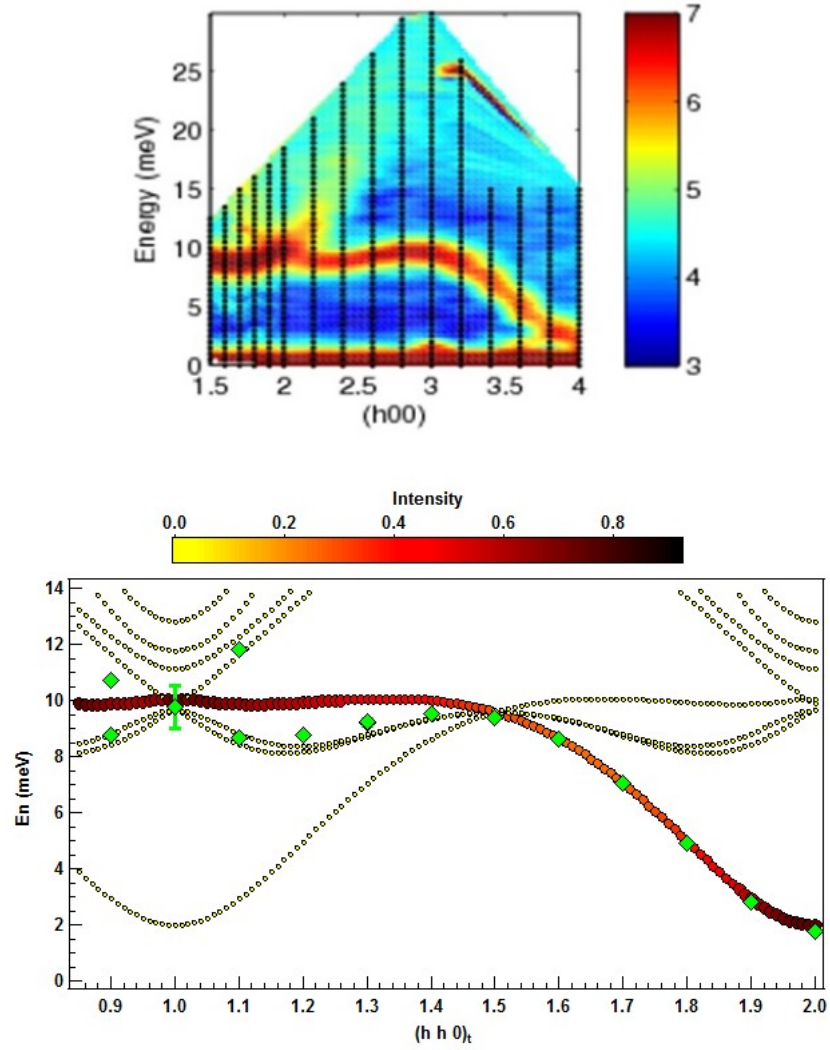


Figure 6.12: *Spin wave dispersion measured along the the cubic direction  $(h,0,0)_c$  (top) and calculated along the equivalent tetragonal direction  $(h,h,0)_t$  (bottom). The calculated energy dispersion is in good agreement with experimental data, but it is not always the same for the intensity indicated in the color map bar ( $\chi^2 = 8.091$ ). [15]*



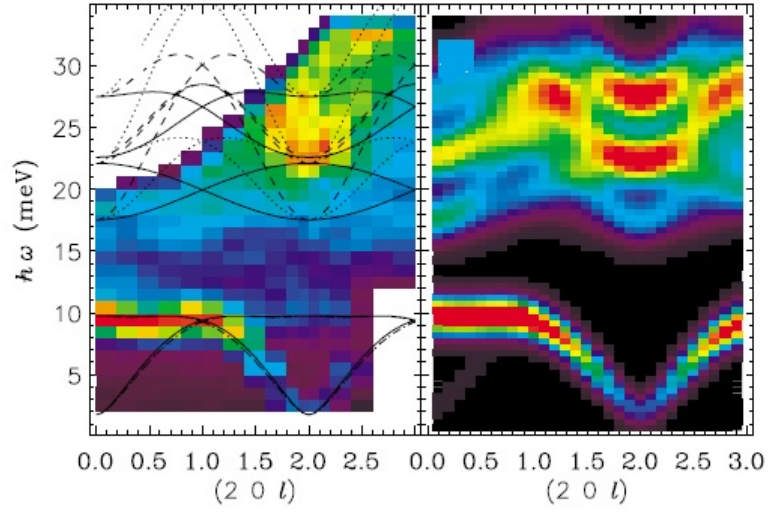


Figure 6.13: *Chung et al. [12] spin wave dispersion along the cubic direction  $(2,0,l)_c$ . They measured the spin wave dispersion with a multi domain sample with unpolarized neutrons. Thus the direction  $(2,k,0)_c$  and  $(2,0,1)_c$  are equivalent. Their calculated spin wave dispersion is similar to ours, in fact, they used the Plumier magnetic structure as ground state [3]. Nonetheless we predict an addition feature which fits better the experimental data.*

In conclusion, the McPhase calculations favour the Plumier magnetic structure and rule out the Garlea structure. The spin wave dispersion calculated from the Plumier magnetic structure is in reasonable agreement with the data and reproduce some of the extra features revealed using polarized inelastic neutron scattering. The exchange constants are consistent with those predicted by Sarkar et al. and our results are consistent with their proposed orbital order.

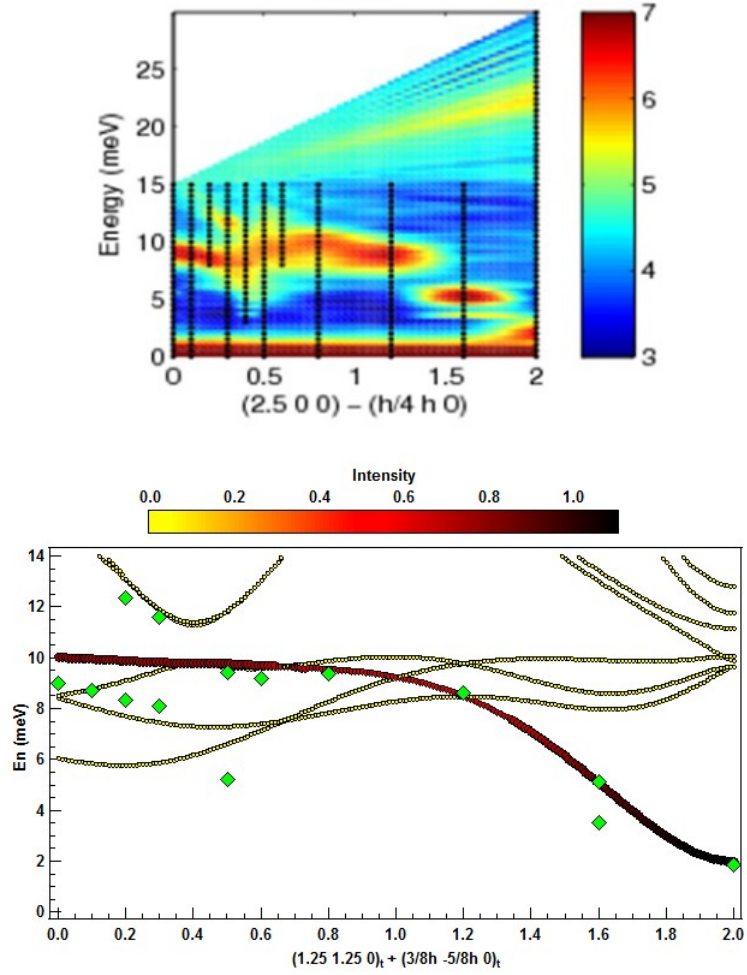


Figure 6.14: *Spin-wave dispersion along the tetragonal off-symmetry measured by A. Magee along the cubic direction  $(2.5+h/4, h, 0)_c$  (top) and calculated along the equivalent tetragonal direction  $(1.25+(3/8)h, -(5/8)h \ 0)_t$  (bottom). Also here we have a qualitative agreement between experiment and theory. [15]*

# Bibliography

- [1] K. Adachi et al. *Phys. Rev. Lett.* *95*,197202 (2005)
- [2] K.I. Kugel et al. *Sov. Phys. JETP* *37*,725 (1973)
- [3] R. Plumier et al. *Solid State Comm.* *64*,53 (1987)
- [4] T. Suzuki et al. *Phys. Rev. Lett.* *98*,127203 (2007)
- [5] H. Tsunetsugu et al. *Phys. Rev. B* *68*,060405(R) (2003)
- [6] O.Tchernysyov et al. *Phys. Rev. Lett.* *93*,157206-1 (2004)
- [7] S. Di Matteo et al. *Phys. Rev. B* *72*,020408(R) (2005)
- [8] S. Sarkar et al. *Phys. Rev. Lett.* *102*,216405 (2009)
- [9] V. O. Garlea et al. *Phys. Rev. Lett.* *100*,066404 (2008)
- [10] T. Mizokawa et al. *Phys. Rev. B* *54*,5368 (1996)
- [11] A. Abragam and B. Bleaney, *Electron Paramagnetic Resonance of Transition Ions* Clarendon Press, Oxford (1970)
- [12] J.H. Chung et al. *Phys. Rev. B* *77*,054412 (2008)
- [13] M. Rotter et al. *J. Phys. Condens. Matter* *24*,213201 (2004)

- [14] [http://www.cpfs.mpg.de/~rotter/homepagemcphase/manual/  
manual.html](http://www.cpfs.mpg.de/~rotter/homepagemcphase/manual/manual.html)
- [15] A. Magae Phd Thesis *Spin Correlations in Frustrated Magnets with Orbital Ordering* (2011), Royal Holloway University of London (2010)
- [16] M.T. Hutchings *Point Charge Calculation et.. Solid State Phys. Vol. 16 ed. Seitz and Thurnbull, Academic Press, New York and London (2004)*  
227

# Chapter 7

## Conclusion and Future Outlook

In this thesis work we achieved important progress in understanding the physics behind the magnetic behaviour and related properties in the three different compounds under investigation.

We characterized the spin dynamics in INVAR  $\text{Fe}_{65}\text{Ni}_{35}$  by performing neutron spin echo and muon relaxation measurements. We observed two different time scale spin dynamics, one with a characteristic time of the order  $\mu\text{s}$  and the other with a characteristic time larger by one order of magnitude. The larger time-scale seems to be associated with the INVAR effect. It has also been observed that a magnetic field suppresses this spin dynamics component. Further muon spin relaxation measurements on the related non-INVAR  $\text{Fe}_{50}\text{Ni}_{50}$  compound would test this hypothesis, while dilatation measurements in an applied magnetic field may explain the effect it has on the spin dynamics and, therefore, on the INVAR effect.

We measured the spin wave dispersion in  $\text{Na}_{0.77}\text{CoO}_2$  using polarized neutrons. Our data are well fitted assuming a simple local moment approach

suggested in literature. Our data are also consistent with more recent DFT studies which show that including the second neighbour inter-layer spin coupling, the magnetism is two-dimensional as may be expected for this kind of system. We obtained a good fit of the energy gap assuming an anisotropic inter-plane spin coupling. Further characterization of the spin wave dispersion in the region far from the zone centre could be used to test the model suggested by the DFT calculations.

We performed magnetic structure calculations on  $\text{MnV}_2\text{O}_4$  including the crystal field effect. These calculations favour the Plumier magnetic structure and rule out the Garlea structure. The calculated spin wave dispersion is in good agreement with experimental data, and is able to reproduce several new features revealed by polarized neutrons. However, the intensities are not in perfect agreement, suggest that additional ingredients may be required. Further elastic neutron scattering measurements may reveal additional features in the magnetic structure, and parallel investigations on the orbital order in this compound may provide useful complementary information.

# Appendix A

## McPhase Input Files

Figure A.1 shows an example of a single ion Input file for the program `iclion`. A similar kind a file has been created to model the  $V^{3+}$  and  $Mn^{2+}$  magnetic ions of  $MnV_2O_4$  in chapter 6. In this file are listed the characteristics of the free magnetic ion considered such as the electronic configuration, the Slater integrals, and the spin orbit coupling. The Crystal Fields coefficients also are listed in Wybourne notation for a particular configuration of surrounding ions.

Figure A.2 instead shows another Input file which is necessary together with single ion files for the modules **mcphas** and **mcdisp** to calculate the ground state magnetic structure and excitations respectively. This file contains the information on the multiple ion interaction in the magnetic system. The components the exchange tensor describing the interactions between a magnetic ion of the unit cell and its neighbours are listed.

Figure A.2 in particular shows the interaction between the cobalt ions in  $Na_xCoO_2$ . In this case we have isotropic symmetric tensor in case of the in-

tra plane interactions and an anisotropic symmetric tensor for the inter plane interactions, thus only three components need to be specified.

Figure A.3 show the file which contains the list scattering vectors for which are calculated the excitation energies by the program module **mcdisp**. Finally figure nr shows the other Input file necessary for **mcdisp** to calculate the magnetic excitations. This file is produced by the core module **mcphas** and contains the mean field at the ion position for a given Temperature,  $T$ , and external magnetic field,  $H$ .



McPhaseExplorer 201104080000

File Edit View Tools Window Help

Co2p.spf

Source Editor

Module Configuration (e.g. f2) d7

ic1ion

Ion type

Co2+ Update Constants Charge (pointcharge for makenn)[|e|] 2 nof\_electrons (for charge densities) 7

Landé factor (GJ) Slater Integrals Spin Orbit Integral Energy Unit Basis

\_database\_err F2 10563.08 F4 6820.59 F6 66.20 meV

Wybourne normalised Crystal Field Parameters

Convert from Ag2+ to Ag2+ Convert

| L[,m] | l=0 | l=2   | l=4    | l=6 |
|-------|-----|-------|--------|-----|
| m=-6  |     |       |        |     |
| m=-5  |     |       |        |     |
| m=-4  |     |       |        |     |
| m=-3  |     |       |        |     |
| m=-2  |     |       |        |     |
| m=-1  |     |       |        |     |
| m=0   |     | -1533 | 1701   |     |
| m=1   |     |       |        |     |
| m=2   |     |       |        |     |
| m=3   |     |       |        |     |
| m=4   |     |       | 1204.8 |     |
| m=5   |     |       |        |     |
| m=6   |     |       |        |     |

Stevens Factors

| a | β | γ |
|---|---|---|
|   |   |   |

Radial Matrix Elements [a.u.=52.92pm]

| <r> [a.u.] | <r> [a.u.] | <r> [a.u.] |
|------------|------------|------------|
| 1.2586919  | 3.7600657  |            |

Radial Wave Function Parameters

$$R(r) = \sum_p C_p \cdot r^{N_p-1} \cdot \exp(-\xi_p \cdot r) \cdot (2\xi_p)^{N_p+.5} / \sqrt{2N_p!}$$

|     | N[p] | XI[p]   | C[p]    |
|-----|------|---------|---------|
| p=1 | 3    | 4.95296 | 0.36301 |
| p=2 | 3    | 12.2963 | 0.02707 |
| p=3 | 3    | 7.03565 | 0.14777 |
| p=4 | 3    | 2.74850 | 0.49771 |
| p=5 | 3    | 1.69027 | 0.11388 |

Add row Remove row

Debye-Waller factor (DWF) [Å<sup>-2</sup>]

$$\text{Intensity} \propto \exp\left(\frac{-DWF \cdot Q^2}{4\pi^2}\right)$$

0.0

Neutron scattering length [10<sup>-14</sup> m]

| Real  | Imaginary |
|-------|-----------|
| 0.249 | 0         |

Neutron magnetic form factor coefficients [Å<sup>2</sup>]

$$\begin{aligned} \langle j_0(Q) \rangle &= A \exp(-aQ^2) + B \exp(-bQ^2) + C \exp(-cQ^2) + D \quad (1) \\ \langle j_2(Q) \rangle &= A Q^2 \exp(-aQ^2) + B Q^2 \exp(-bQ^2) + C Q^2 \exp(-cQ^2) + D Q^2 \quad (2) \\ \langle j_4(Q) \rangle &= A Q^2 \exp(-aQ^2) + B Q^2 \exp(-bQ^2) + C Q^2 \exp(-cQ^2) + D Q^2 \quad (3) \\ \langle j_6(Q) \rangle &= A Q^2 \exp(-aQ^2) + B Q^2 \exp(-bQ^2) + C Q^2 \exp(-cQ^2) + D Q^2 \quad (4) \end{aligned}$$

| FF[j], [Å] | c=A     | c=a     | c=B    | c=b    | c=C     | c=c    | c=D    |
|------------|---------|---------|--------|--------|---------|--------|--------|
| j=0        | 0.4332  | 14.3553 | 0.5857 | 4.6077 | -0.0382 | 0.1338 | 0.0179 |
| j=2        | 1.9049  | 11.6444 | 1.3159 | 4.3574 | 0.3146  | 1.6453 | 0.0017 |
| j=4        | -0.4759 | 14.0462 | 0.2747 | 3.7306 | 0.2458  | 1.2504 | 0.0057 |
| j=6        |         |         |        |        |         |        |        |

Figure A.1: An example of Input file for the program **ic1ion** of the package **McPhase**.

```

1 # autocreated file for iclioni
2 #<!--mcphase.mcphas.j-->
3 #
4 #
5 # Lattice Constants (A)
6 #! a=2.84 b=2.84 c=10.82 alpha= 90 beta= 90 gamma= 120
7 #! r1a= 1 r2a= 0 r3a= 0
8 #! r1b= 0 r2b= 1 r3b= 0 primitive lattice vectors [a][b][c]
9 #! r1c= 0 r2c= 0 r3c= 1
10 #! nofatoms=2 nocomponents=3 number of atoms in primitive unit cell/number of components of each spin
11 #
12 #
13 #! da= 0 [a] db= 0 [b] dc= 0 [c] nofneighbours=8 diagonalexchange=2 gJ=2 cffilename=Co4p1.sipf
14 # da[a] db[b] dc[c] Jaa[meV] Jbb[meV] Jcc[meV] Jab[meV] Jba[meV] Jac[meV] Jca[meV] Jbc[meV] Jcb[meV]
15 #! symmetruecxhsnge=1 indexexchange = JaJa JbJb JcJc
16 -1 -1 0 5.250000e+000 5.25 5.25
17 1 1 0 5.25 5.25 5.25
18 -1 0 0 5.25 5.25 5.25
19 1 0 0 5.25 5.25 5.25
20 0 1 0 5.25 5.25 5.25
21 0 -1 0 5.25 5.25 5.25
22 0 0 -0.5 -11.045 -11.045 -11.226
23 0 0 0.5 -11.045 -11.045 -11.226
24 #
25 #! da= 0 [a] db= 0 [b] dc= 0.5 [c] nofneighbours=8 diagonalexchange=2 gJ=2 cffilename=Co4p1.sipf
26 # da[a] db[b] dc[c] Jaa[meV] Jbb[meV] Jcc[meV] Jab[meV] Jba[meV] Jac[meV] Jca[meV] Jbc[meV] Jcb[meV]
27 #! symmetruecxhsnge=1 indexexchange = JaJa JbJb JcJc
28 -1 -1 0 5.25 5.25 5.25
29 1 1 0 5.25 5.25 5.25
30 -1 0 0 5.25 5.25 5.25
31 1 0 0 5.25 5.25 5.25
32 0 1 0 5.25 5.25 5.25
33 0 -1 0 5.25 5.25 5.25
34 0 0 -0.5 -11.045 -11.045 -11.226
35 0 0 0.5 -11.045 -11.045 -11.226
36 #

```

Figure A.2: An example of Input file for the core module **mcphas** of the package McPhase. This file contains the interaction between each magnetic ion of the unit cell and its neighbours. In the case of  $\text{Na}_x\text{CoO}_2$  we two cobalt ions in the unit cell.

```

1 # Parameter file mcdisp.par - read by mcdisp version 3.6
2 #<!--mcdisp.mcdisp.par>
3 #*****
4 # mcdisp - program to calculate the dispersion of magnetic excitations
5 # reference: M. Rotter et al. J. Appl. Phys. A74 (2002) 5751
6 #*****
7 #
8 # mcdisp calculates the neutron scattering cross section dσ/dΩdE' [barn/sr/meV/f.u.]
9 # f.u.=crystallographic unit cell (r1xr2xr3) for inelastic and diffuse scattering
10 #
11 # depending on what is kept constant it follows either kf or ki (1/Å)
12 #ki=10
13 # For measurements with a triple axis spectrometer kf is fixed as in the me case of MnV2O4
14 kf=2.662
15 #
16 # emin and emax define the energy range in which neutron intensities are calculated
17 # for full calculation of the dynamical susceptibility (option "-r", inversion of the MF-RPA equation
18 # for each point in Q-omega space) the minimum and maximum energy has to be given (energy stepwidth is
19 # equal to the parameter epsilon given in the command line after "-r")
20 #
21 emin=-200
22 emax=200
23 # optional parameter is extended_eigenvector_dimension
24 # which is used to define, how many components of the
25 # eigenvector should be in the output to file mcdisp.qee
26 # important for charge density movies, e.g. (i) for module solion
27 # - f electrons - chargedensity fluctuation needs coefficients
28 # l=3, i.e. eigenvector should be extended to 3+5+7+9+11+13=48,
29 # (ii) for module iclion with f-electrons eigenvector has to be
30 # extended to 6+5+7+9+11+13=51 (here there are 6 components for
31 # all spin and orbital moments), (iii) for module iclion and d-
32 # electrons l=2 it suffices 6+5+7+9=27
33 #!extended_eigenvector_dimension=3
34 #
35 # It follows either
36 #
37 # (i) a Q vector mesh to be mapped in the calculation
38 #hmin=0 hmax=0 deltah=0.1
39 #kmin=0 kmax=0 deltak=0.1
40 #lmin=2.5 lmax=3.5 deltal=0.01
41 #
42 # h k l measured energies (meV)
43 # - list of q-vectors
44 #
45 1 1 0 9.765 90.909 1229 3.53
46 1.1 0.9 0 8.792 43.478 667 1.380
47 1.2 0.8 0 8.740 58.824 737 1.754
48 1.3 0.7 0 9.208 62.500 784 1.879
49 1.4 0.6 0 9.584 58.824 1496 2.447
50 1.5 0.5 0 9.490 71.429 835 1.845
51 1.6 0.4 0 8.687 52.632 883 1.732
52 1.7 0.3 0 7.081 38.462 767 1.800
53 1.8 0.2 0 4.915 34.483 891 1.727
54 1.9 0.1 0 2.887 71.429 557 0.942
55 2 0 0 1.727 0.33 690 2.000
56

```

Figure A.3: Input file for the module **mcdisp** of the package McPhase. This file contains the list of scattering vectors for which magnetic excitation energies are calculated. In this file are also specified the energy range in which the neutron scattering intensities are calculated and the incident or the emitted wavevector, ( $k_i$  and  $k_f$  respectively) depending on the geometry of the inelastic experiment. If a triple-axis spectrometer is used as in the case of  $\text{MnV}_2\text{O}_4$   $k_f$  is fixed. If in the list of scattering vectors are also included the energy measured experimentally with their statistical weight the program calculate the value of the  $\chi^2$  factor.

```

1#(mcphas version 2.6 Tue Sep 30 01:11:08 2008
2# CePd2Si2 see dijk00 PRB
3 # a=4.2318 b=4.2318 c=9.9035 alpha= 90 beta= 90 gamma= 90
4# r1a= 1 r2a= 0 r3a= 0.5
5# r1b= 0 r2b= 1 r3b= 0.5 primitive lattice vectors [a][b][c]
6# r1c= 0 r2c= 0 r3c= 0.5
7# nofatoms=1 nofcomponents=3 number of atoms in primitive unit cell/number of components of each spin
8#*****
9# da= 0 [a] db= 0 [b] dc= 0 [c] nofneighbours=368 diagonalexchange=0 gJ=0.857143 cffilename=Ce3+.cf
10#x y T[K] |H| H[T] Ha[T] Hb[T] Hc[T] nofspins nofatoms(in primitive basis) nofmeanfield-components
11 #mfa(1) mfa(2) .... selfconsistent Mean field configuration
12 #mfb(1) mfb(2) .... UNITS: mf(i)=gJ*mu_B*heff(i) [meV]
13 #mfc(1) mfc(2) .... (i.e. divide by gJ and mu_B=0.05788meV/T to get effective field[T])
14 1.3 0 1.3 0 0 0 0 8 1 3
15 0.5863 -0.5863
16 0.5865 -0.5865
17 0.0000 -0.0000
18 -0.5863 0.5863
19 -0.5865 0.5865
20 0.0000 -0.0000
21
22 -0.5863 0.5863
23 -0.5865 0.5865
24 -0.0000 0.0000
25 0.5863 -0.5863
26 0.5865 -0.5865
27 -0.0000 0.0000
28
29
30

```

Figure A.4: *Input file containing the mean field at ion sites calculated with the program **mcphas** for a given Temperature, T, and external magnetic field, H. This file is necessary to calculate the magnetic excitation energy with **mcdisp**.*